

A NOVEL 3-D FLUX STRUCTURE FOR SWITCHED RELUCTANCE MACHINES

by

Pengyuan Chen

APPROVED BY SUPERVISORY COMMITTEE:

Babak Fahimi, Chair

Poras T. Balsara

Matthew Gardner

Dinesh Bhatia

Copyright 2022

Pengyuan Chen

All Rights Reserved

To my parents,

Mr. Chen Lin and Mrs Chen Xiaomeng

A NOVEL 3-D FLUX STRUCTURE FOR SWITCHED RELUCTANCE MACHINES

by

PENGYUAN CHEN, BS, MS

DISSERTATION

Presented to the Faculty of

The University of Texas at Dallas

in Partial Fulfillment

of the Requirements

for the Degree of

DOCTOR OF PHILOSOPHY IN

ELECTRICAL ENGINEERING

THE UNIVERSITY OF TEXAS AT DALLAS

December 2022

ACKNOWLEDGMENTS

I would like to express my gratitude to my advisor, Professor Babak Fahimi, for his guidance, his endless support, and the confidence he has shown in me over the years. His constant encouragement in my dissertation work and my Research Assistant duties has helped me to look forward to the future with enthusiasm and confidence in my abilities.

I would like to thank Professor Poras Balsara, Professor Dinesh Bhatia, and Professor Matthew Gardner for serving on my committee and for offering valuable suggestions to make my dissertation possible.

Finally, I would like to thank my parents, Mr. Chen, Lin and Mrs Chen. Xiaomeng, for their constant support both emotionally and financially, in completing this endeavor. I sincerely appreciate their patience and understanding while waiting for me to complete my degree.

Without their overwhelming positive influence on my life, I would not have been able to achieve my goals.

November 2022

A NOVEL 3-D FLUX STRUCTURE FOR SWITCHED RELUCTANCE MACHINES

Pengyuan Chen, PhD
The University of Texas at Dallas, 2022

Supervising Professor: Babak Fahimi

Switched Reluctance Machines (SRMs) receive considerable attention from industry and academia over the past few decades. SRMs are generally inexpensive, reliable, and mechanically robust when compared to other types of electrical machines. Design of magnetic configuration for SRMs is a prevalent topic in the literatures. The focus of these design practices can be categorized into boosting average torque, torque pulsation mitigation, loss reduction (copper loss, windage loss, core loss), vibration suppression, and acoustic noise suppression to name a few. The present dissertation proposes a novel 3-D flux structure containing both radial and axial flux structures. The step-by-step design procedure and the background reasoning are discussed in detail. The illustrations and reasoning in this study highly relies on 3D finite element analysis (FEA) and magnetostatic measurements. Through multiple revisions and optimizations, a prototype of the proposed machine is chosen and fabricated to verify the claims. Besides switched reluctance machine, the proposed 3D concept can be used in other types of electric machinery.

TABLE OF CONTENTS

ACKNOWLEDGMENTS	v
ABSTRACT	vi
LIST OF FIGURES	ix
LIST OF TABLES	xiv
CHAPTER 1 INTRODUCTION.....	1
CHAPTER 2 3D FLUX SRM WITH SALIENT POLES	18
2.1 <i>Principles of operation</i>	18
2.2 <i>Fundamental Magnetic Design</i>	18
2.3 <i>The proposed 3D flux structure</i>	38
2.4 <i>First version: a double-salient pole 3D flux SRM</i>	42
CHAPTER 3 MODIFIED SEGMENTED ROTOR 3D FLUX SRM	83
3.1 <i>The machine structure</i>	86
3.2 <i>The magnetic design</i>	92
3.3 <i>The comparison between two structures</i>	100
3.4 <i>The second revision on segmented-rotor 3D flux 8/14 machine</i>	102
CHAPTER 4 THE OPTIMIZATION METHOD	108
CHAPTER 5 SIMULATION RESULTS.....	116
5.1 <i>The simulated electromagnetic behavior of the model 6211011</i>	118
5.2 <i>The simulated mechanical and thermal performance of the model 6211011</i>	123
CHAPTER 6 EXPERIMENTAL RESULTS	130

6.1 <i>Experimental results</i>	132
6.2 <i>Discussion of discrepancies between simulation results and experimental results</i>	138
CHAPTER 7 CONCLUSION AND FUTURE WORKS.....	145
BIBLIOGRAPHY	147
BIOGRAPHICAL SKETCH.....	150
CURRICULUM VITAE	

LIST OF FIGURES

Figure 1.1: The map of different type of electrical machines [2].	2
Figure 1.2: The price history of per kilograms of Neodymium Oxide from <i>kitco.com</i> .	5
Figure 1.3: The price history of per kilograms of Praseodymium Oxide from <i>kitco.com</i> .	5
Figure 1.4: (a) PM machine (b) IM (c) SRM.	7
Figure 1.5: (a) PMA-synSRM (b) double-stator PMSM (c) stator PM machine.	9
Figure 1.6: Summary of configurations of common SRMs.	13
Figure 1.7: Sample drawings of multiple type SRMs: a) 8/6 inner-rotor SRM b) 8/6 outer-rotor SRM c) 8/6 single-side axial flux SRM d) 8/6 double-side axial flux SRM e) 8/6 back-to-back SRM f) 8/6 multi-stack SRM g) 8/6 linear SRM (partial view).	14
Figure 2.1: a) Flux Linkage versus Excitation b) Inductance versus Rotor Position	20
Figure 2.2: Plots of magnetic energy.	22
Figure 2.3: a) the ideal locus of operating point b) the locus of operating point under chopping.	23
Figure 2.4 Flux lines of a 6/4 SRM: a) unaligned position b) aligned position.	26
Figure 2.5: The simplified magnetic circuit of one magnetic flux path of a 6/4 SRM.	27
Figure 2.6: The dimension drawing of the 2D model.	31
Figure 2.7: Self Inductance of Phase A: a) single phase active b) stroke active.	34
Figure 2.8: Torque Profiles: a) Single Phase Torque (Phase-A active) b) Stroke Torque.	34
Figure 2.9: Single phase excitations and normal excitation sequences.	35
Figure 2.10: The short magnet flux path formed by double-phase excitations.	36
Figure 2.11: Images of end windings of radial flux machines and axial flux machines [29].	38
Figure 2.12: Structure with interior rotor.	40
Figure 2.13: Structure with interior stator.	41

Figure 2.14: The views of extra axial rotor pole surface.	42
Figure 2.15: Circulating magnetic flux created by phase A excitation.....	44
Figure 2.16 :The magnetic flux paths created by the “equivalent phase”. [30].....	45
Figure 2.17: The equivalent magnetic circuit of $\frac{1}{4}$ model.....	47
Figure 2.18: The magnetic flux paths created by three-phase excitation.	48
Figure 2.19: The magnetic field of 16/12 machine with 3.3° forward rotation.	48
Figure 2.20: The equivalent magnetic circuit of $\frac{1}{4}$ model.	49
Figure 2.21: The radial magnetic field of the 16/12 3D flux SRM under three-phase excitation .	51
Figure 2.22: The axial magnetic field of the 16/12 3D flux SRM under three-phase excitation...	52
Figure 2.23: The magnetic field in the cross section of flux tube [30]	54
Figure 2.24: The sectionized stator pole with dimension labels	56
Figure 2.25: The sectionized rotor poles with dimension labels	60
Figure 2.26: The alignment pattern of the stator and rotor	61
Figure 2.27: The exploded view of the 16/12 salient pole structure.....	61
Figure 2.28: The radial magnetic field layout of three different pole configurations.....	62
Figure 2.29: The geometric view of the simulated models [30]	65
Figure 2.30: The 3D magnetic field in the 08/14 structure	67
Figure 2.31: The simplification of 3D 08/14 SRM [30]	69
Figure 2.32: The geometrical layout of radial probe sheets and axial probe sheets [30]	70
Figure 2.33: The magnetic flux distribution printed on axial probe sheets.	73
Figure 2.34: The magnetic flux distribution printed on radial probe sheets.	74
Figure 2.35: Illustration of the tendency of the 3D flux	75

Figure 2.36: The diagram in Twin Builder	76
Figure 2.37: The static torque of 08/14 3D Flux SRM at 180rpm [30]	77
Figure 2.38: The hysteresis control based current profiles of the co-simulation.....	78
Figure 2.39: The power loss profiles of stator and rotor.....	79
Figure 2.40: The saturated thermal image of stator and rotor.....	80
Figure 2.41: The equivalent tensile stress and deformation of stator.	81
Figure 2.42: The equivalent tensile stress and deformation of rotor.	81
Figure 2.43: The equivalent tensile stress and deformation of stator support and shaft.....	82
Figure 3.1: The overlap pattern of segmented-rotor SRM.....	84
Figure 3.2: The cross section of optimized 08/14 SRM	87
Figure 3.3: The rotor magnetic segments and non-magnetic segments.....	88
Figure 3.4: The region prone to the cross-coupling issues.	89
Figure 3.5: The 3D model of the inner stator of the segmented-rotor 08/14 SRM.....	91
Figure 3.6: Flux lines in radial part of segmented-rotor 08/14 SRM.....	92
Figure 3.7: the geometrical distribution of probe sheets.....	94
Figure 3.8: The flux plots of axial probe sheets.....	96
Figure 3.9: The 3D flux vector – ½ model	98
Figure 3.10: The flux plots of radial probe sheets.	99
Figure 3.11: The stroke torques of two 08/14 models	102
Figure 3.12: The ambiguous design issue.....	103
Figure 3.13: The new winding configuration of segmented-rotor 08/14 machine	104
Figure 3.14: The circulation magnetic flux due to the discrepancies in excitations.....	105

Figure 3.15: The 2D model of a 10/18 machine: a) single phase active b) stroke active	107
Figure 4.1: The fundamental operation of Genetic Algorithm (GA) Optimization.....	109
Figure 4.2: The behind logics of different optimizations	111
Figure 4.3: The simplified gene sequence	113
Figure 5.1: The static stroke torque profiles of GA optimized down-scaled models.	117
Figure 5.2: The B-H curve and loss curve of Hiperco 50 27mil.....	118
Figure 5.3: Mechanical properties of Hiperco50 27mil.....	119
Figure 5.4: The co-simulation electrical interface	120
Figure 5.5: The simulated excitation sequence.....	121
Figure 5.6: The co-simulated torque profile of the second and third strokes	122
Figure 5.7: The co-simulated core loss profile of the second and third strokes	122
Figure 5.8 The phase C inductance profile from the unaligned position to the aligned position.	123
Figure 5.9: The flux plots of stator center, axial stator pole surface, axial rotor segment surface.	123
Figure 5.10: The deformation information of rotor	125
Figure 5.11: The stress information of rotor	125
Figure 5.12: Deformation information of the stator.....	126
Figure 5.13: Stress information of the stator	126
Figure 5.14: The stress and deformation information of the support unit.	127
Figure 5.15: The inner temperature of rotor frame	128
Figure 5.16: The temperature of rotor segments.....	128
Figure 5.17: The temperature of stator core.....	129

Figure 5.18: The temperature of support unit	129
Figure 6.1: The 5-phase SiC asymmetric inverter board.	131
Figure 6.2: The stator with installed windings and support unit.....	132
Figure 6.3: The rotor with installed rotor segments.....	132
Figure 6.4: The static torque testbed.....	133
Figure 6.5: Static torque of phase A and phase B.....	134
Figure 6.6: Static stroke torque of phase A and phase B.	136
Figure 6.7 The oscilloscope reading at the initial position of the stroke of Phase A and Phase B	136
Figure 6.8: the current and voltage transient	137
Figure 6.9: The reconstructed inductance profile.	138
Figure 6.10: Flux plot at different positions	140
Figure 6.11: estimated aligned position inductance and unaligned position inductance	141
Figure 6.12: estimated inductance profiles with different airgaps.....	141
Figure 6.13: The experimental inductance profiles and co-simulated inductance profiles.	142
Figure 6.14 The comparisons between simulated torques and experimental results.....	144

LIST OF TABLES

Table 2.1: Positive Torque Zone and Stroke of Common Topology.....	32
Table 2.2: Sample parameters.....	33
Table 2.3: The Comparison Of Different Pole Configurations [30].....	65
Table 2.4: Comparison Of 08/14 Models With the Commercial SRM	68
Table 3.1:The comparison between two versions of 08/14 3D flux machine	101
Table 5.1:The machine parameters of the down-scale 10/18 model 621011	121

LIST OF SYMBOLS AND ABBREVIATIONS

x/y	stator pole number / rotor pole number
\mathcal{R}	Magnetic Reluctance
\mathcal{F}	Magnetic Motive Force
Ψ	flux linkage in Wb
W_{total}	total energy
W_F	field energy
W_C	coenergy
θ_r	rotor position
ω	rotation speed
CW	clockwise direction
CCW	counterclockwise direction
R_{pn}	the Nth rotor pole
S_{pn}	the Nth stator pole
$\angle S_{pole}$	the arc of stator pole
$\angle S_{slot}$	the arc of stator slot
$\angle R_{pole}$	the arc of rotor pole
$\angle R_{slot}$	the arc of rotor slot

CHAPTER 1

INTRODUCTION

Over the past few decades, the fabrication technologies of power semiconductors and energy storage units have progressed in the industry and academia. In particular, the power semiconductors become smaller, more powerful, and more dependable. The commercialization of wide bandgap devices and powerful microcontrollers makes development of versatile control methodologies and high-end circuitries possible. The precise machining technologies such as 5-axis CNC milling, line cut, and EDM, make the manufacturing of complex machine structures possible and provides new degrees of freedom for machine designers. Considering the new manufacturing and fabrication capabilities, notable investigations into design of brushless electrical machine have been performed over the recent years [1]. The objectives of machine design usually include achieving higher power density, wider operational speed range, higher efficiency, and higher reliability. [1], [2] provide high-level reviews on emerging evolutions of propulsion systems, electrical machines, drivers, energy storage units, and control methods. [2] mainly discussed merits and demerits of different types of electrical machines which are widely adopted for electrical vehicles (EVs) applications and home appliances. In references [1-3], the traditional three types of machines, namely, permanent magnetic synchronous machines (PMSMs), induction machines (IMs), and reluctance machines (RMs) are reviewed as well as their subcategories. Besides the automotive industry, superior choices of novel electric machines are also beneficial to electrified ships, aircraft, drones, scooters, compressor, and robot applications. The proposed novel magnetic configuration aims to maximally utilize machine space for torque harvesting. In the next chapter, the step-by-step explanation of this magnetic

configuration is presented. Figure 1.1. illustrates the existing and emerging types of brushless electric machinery [2].

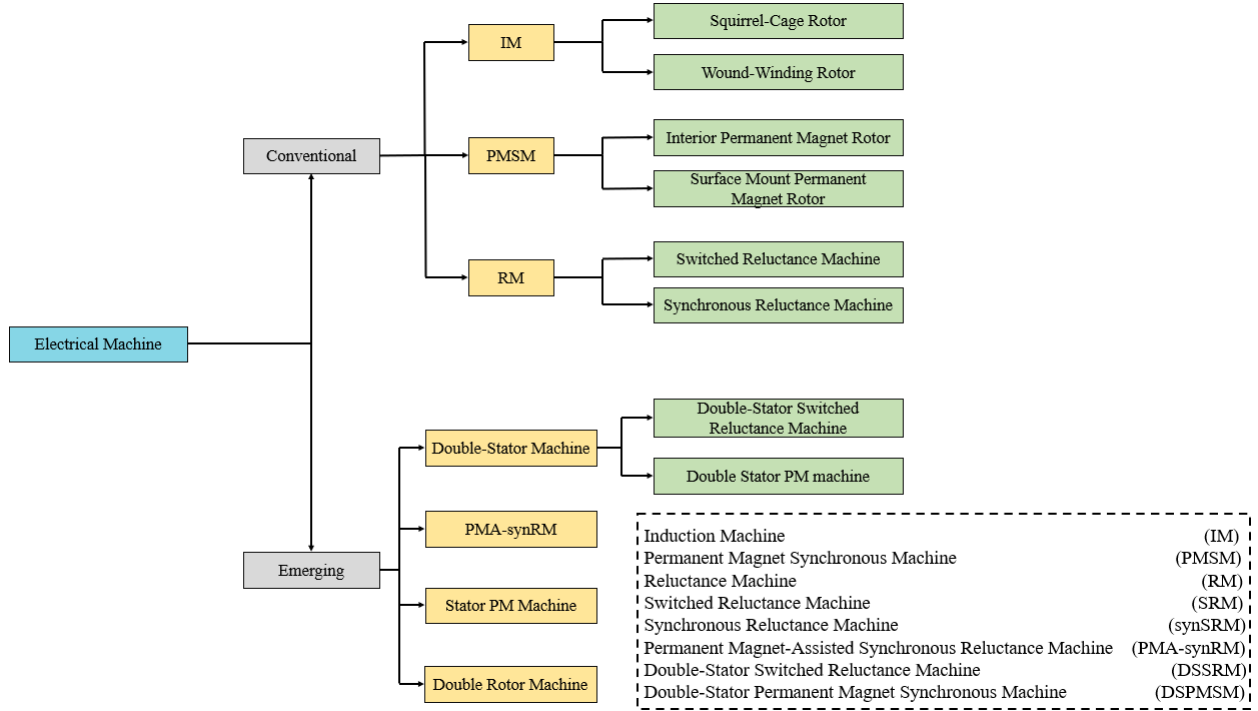


Figure 1.1: The map of different type of electrical machines [2].

Brushless machines do not have brushes and commutators and as such require significantly less maintenance and offer a more compact and superior mechanical integrity. The first category of brushless machines includes squirrel cage induction machine. According to the nature of magnetic field, the electromagnetic torque originates from the interaction between rotor flux (offspring field) and stator flux (parent field). The rotor flux induced in induction machines exists due to the presence of the difference between the rotational speed and the synchronous speed. According to the asynchronous operation and the Faraday's Law the induced current, in the short circuited bars of the rotor, forms the rotor flux. The induced rotor current does not require brushes/commutators to alternate its direction. In fact, the synchronous interaction of the

rotor field and the stator field in the airgap eliminates the need for any manipulation of rotor currents and in doing so greatly simplifies the structure of the motor. Due to the absence of physical presence of brushes and slip rings, the squirrel cage induction machine can safely work in harsh environments such as mines where explosive gases are present. It must be noted that in the case of wound rotor induction machine, the presence of slip rings and the possibility of short circuit within the three-phase winding of the rotor can lead to additional maintenance and electrical failures [4]. Since the energy of the induced rotor flux has originated from the rotating field of the stator, the efficiency of the induction machine can never be higher than those of permanent magnet synchronous machines (PMSM). Furthermore, the rotor windings or copper bars could result in severe thermal issues or even failures. This can potentially complicate the control of the stator currents and require multi-layer protection, especially for the in-rush current protection. To overcome these issues, Tesla adopted special fabrication processes to build casted copper conductors [5]. Induction machines (IM) are used in commercial EVs, such as Tesla Model 3 and Model S, BMW i3, Mercedes-Benz, B-Class-Electric, Toyota RAV-4, and Nissan Leaf. Even though the conductors/windings used in the rotor of IM would be a concern, the absence of PMs and brushes still provide enough attraction for IMs. Due to the existing slip frequency, high precision control of speed in IMs could be difficult. Contrary to IMs, the permanent magnet (PM) machines have inherent rotor flux from magnets that are installed in the rotor. The amateur only needs to support the stator flux in quadrature axis and as such the PM machines generally enjoy the highest efficiency in constant torque region. This advantage, however, fades away in the constant power/field weakening region where negative direct axis currents are necessary to be able to inject sinusoidal current into the stator. As it is widely

accepted, the PMs such as NdFeB and SmCo require the use of rare-earth metals. SmCo magnets offer higher tolerance than NdFeB in terms of operating temperature and demagnetization. NdFeB magnets possess the higher density of magnetic energy per cubic meter. PMs suffer from the issues such as high temperature, demagnetization, and physical shocks, even though material industry keeps developing new types of PM alloys with wider tolerances. Depending on the mounting locations and the rotor design, the process for assembly of PM machines could be complicated. The interior permanent magnet synchronous machine (IPMSM) developed for Toyota Puris, the V-shape-magnet rotor structure have been vastly studied by the industry and academia. Even though history of the recorded price for rare-earth metals are not quite accessible to the public, price histories of Neodymium Oxide and Praseodymium Oxide for the recent years can be found and are shown in Figure 1.2 and Figure 1.3. Although the prices of rare-earth oxides slightly drop in the past few months, the long term trends are point toward an increase and that they have been doubled over the past 5 years (source: [kitco.com](http://www.kitco.com)). Even though companies keep investigating low-cost PM materials and the PM machines dominate the EV markets and offshore wind generator markets, an alternative propulsion solution without the use of rare-earth materials are still in high demand. After all, the resources of rare-earth materials may not be endless.

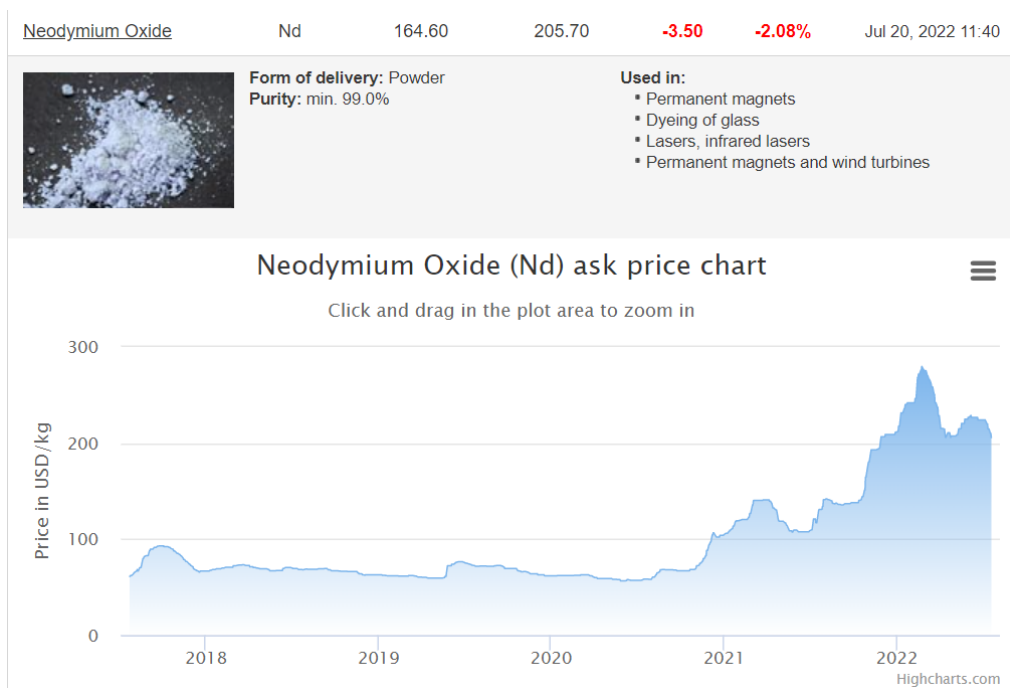


Figure 1.2: The price history of per kilograms of Neodymium Oxide from *kitco.com*.



Figure 1.3: The price history of per kilograms of Praseodymium Oxide from *kitco.com*.

Dating back to 1838, the concept of switched reluctance machines (SRMs) was experimented for traction of a locomotive. SRMs belong to the category of the reluctance machines (RMs). The other prominent member of the RMs is the synchronous reluctance machine (synRM). In reluctance machines, the torque generation relies on the magnetic field interaction with the magnetic saliencies. In particular, the operation principle of switched reluctance machine is relatively straightforward. The active stator poles behave as electromagnets that attract the nearest rotor poles into full alignment. In the process alignment to the active stator poles, the positive reluctance torque is generated. The synRMs operate slightly different from SRMs. Basically, the rotor structure is similar to that of interior permanent magnet machines (IPMs) rotors without the presence of magnets such that there are no inherent rotor fluxes. However, there exists an implicit saliency caused by the flux barriers. The torque in synRMs is achieved by the tracking of the rotating magnetic field in the presence of both q -axis and d -axis excitation and the difference between q -axis inductance and d -axis inductance. In fact, the second term in (1.1) denotes the reluctance torque of a synRM as is known as reluctance torque. (1.1) is a full expression of torque of an IPMSM.

$$T(I_d, I_q) = \frac{p}{2} ((\Psi_r * I_q) + (L_d - L_q) * I_d * I_q) \quad (1.1)$$

Since there is neither rotor conductors nor magnets in the rotor structure, the RMs are favored by their robust structure, low cost, and relatively easy fabrications. Even though the low torque density and high torque pulsation are the well-known demerits in this family of electric machines, RMs are viewed as versatile solutions under harsh environments and in low-cost EV applications such as golf carts [7, 8]. Dating back to 1980s, Lucas Chloride adopted the SRM-

based system for their concept EVs [8]. The sample drawings of PM machines, IMs, and SRMs are shown in Figure 1.4.

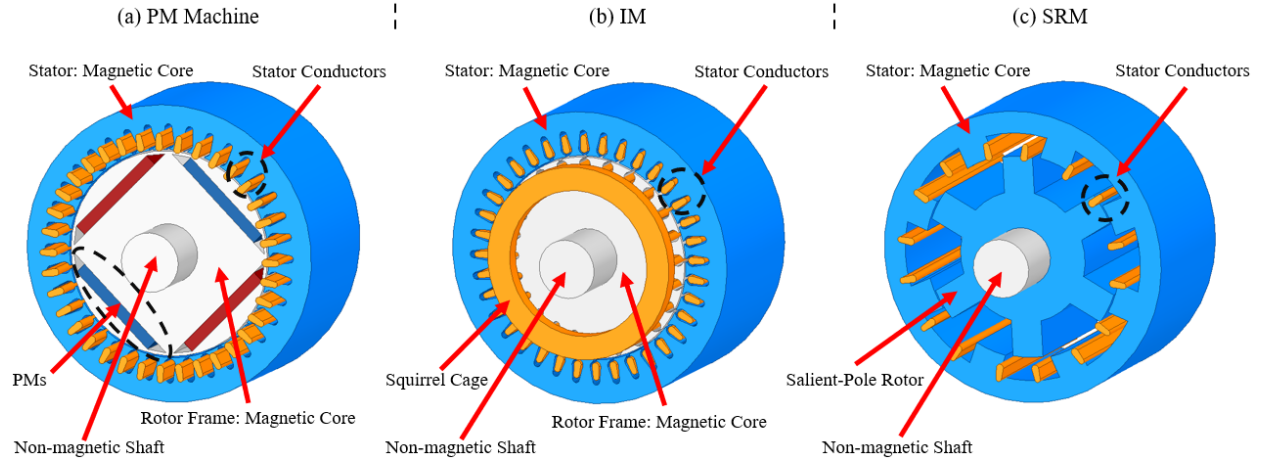


Figure 1.4: (a) PM machine (b) IM (c) SRM.

Derived from IPMs, the permanent magnet-assisted synchronous reluctance machines are also investigated. Equation (1.1) shows the combination of electromagnetic reaction torque and reluctance torque. Since the rare-earth materials are scarce and expensive, it is reasonable to increase the contribution of the reluctance torque and reduce the contribution of the reaction torque. This is the underlying reason for use of PM-assisted synRMs (PMA-synRMs). From another vantage point, the surface mounted permanent magnet synchronous machines (SPMSMs) and interior permanent magnet synchronous machines (IPMSMs) normally offer strong radial rotor fluxes such that in order to operate these machines at high-speed the DC bus voltage must be sufficiently large to counteract the back-EMF which is linearly proportional to rotor flux and speeds. Since the DC bus voltage cannot be arbitrarily high, the common solution is to perform field weakening by means of counteracting PMs so that the back-EMFs with a reduced rotor flux at the speed could have a reduced and manageable magnitude. This raises a question that if a machine is meant to operate at higher speed, why not install less strong PMs or

just install weaker PMs with less energy densities. In this way, the rated speed could be further extended [12]. The matter of labeling a machine as IPMs or as a (PMA-synRM), therefore, depends on the major contributing torque component. PMA-synRMs could adopt materials such as MnAl-Z (Z =C,B,Ga as doping elements), MnBi which offer less energy densities [9]. Those weak magnets were carefully synthesized at precise high-temperature methods, followed by various milling and annealing steps and then installed on the quadrature axis of the rotor. Other than pursuing the higher operational speed, some double-stator PM vernier machines (DSPVMs) are invested for their high torque density. The PM rotor of a DSPVM could be installed in the middle of the exterior stator and the inner stator [13]. The double-stator structure could also be applied to IMs and SRM configurations. In [14], the rotor shape of double-stator SRM (DSSRM) is optimized to achieve higher reluctance torque and less torque pulsations. Using a proper winding layout, short magnetic paths could be formed by excitations from both inner stator and the outer stator in order to maximize the flux linkages such that the maximum average reluctance torque can be obtained. The same design philosophy could be theoretically applied to IMs. However, this tends to increase complexities and additional fabrication costs. It may be difficult to tell that double-rotor PM machines or double-rotor switched reluctance machines are derived from a similar idea. Interior rotor and exterior rotor share a common stator such that both rotors could either simultaneously harvest torque or alternatively perform during startup, normal operational region, and field-weakening region. Certainly, the additional expense and mechanical integrity complicates the design and fabrications. To achieve a simple structure with high output torque, the stator flux switching PM machines were developed by Rauch and Johnson back in 1955 [15]. The structure could be viewed as a combination of a salient structure with PMs.

Different from PMA-synRMs, the salient poles of the stator are meant to switch the active flux paths originated from PMs such that the rotor salient poles are attracted to stator poles subsequently in a desired sequence. The sample drawings of emerging machines including PMA-synSRM, double-stator PMSMs, and stator PM machines are shown in Figure 1.5.

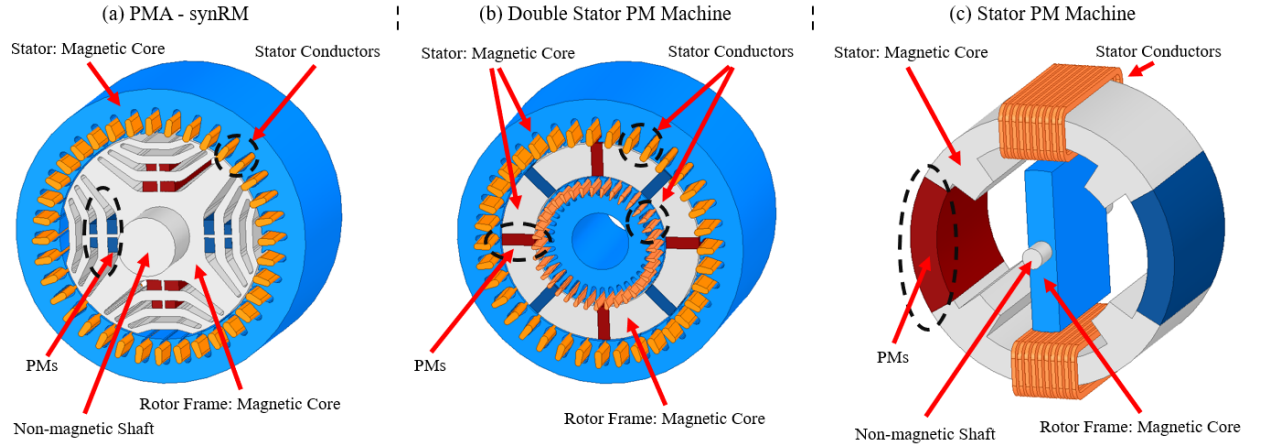


Figure 1.5: (a) PMA-synSRM (b) double-stator PMSM (c) stator PM machine.

To avoid widening the scope, other emerging topologies are not covered here. In the above categories, SRMs have the simplest structures and require simple control method which could accelerate the design phase as well as the verification process. The proposed structure in this thesis is based on the conventional SRM topologies. SRMs could be divided into two categories according to its configuration, namely double-salient pole structure and the segment-rotor structure. Double-salient pole structure generally presents explicitly salient poles on both stator and rotor structures as shown in Figure 1.4 c). The segmented-rotor structure does not necessarily have extrude rotor poles since rotor segments can be inserted into the cylindrical rotor frame, which means the rotor surface could be cylindrical. The rotor segments are built with soft ferromagnetic material while the rotor frame will be fabricated using non-magnetic material. Some emerging SRM solutions has been derived from the above two basic categories.

In [16], authors simulated a modular stator structure that requires complex mounting techniques and raises mechanical integrity concerns. The modular stator structure is scarce in the literature which may indirectly imply the difficulty of the fabrication process. In [17] authors published a comprehensive review on SRMs structure with multiple configurations and control methods. The review starts from a double salient radial flux inner rotor SRM and ends up with a linear SRM. As the classic type of SRM, the double salient inner rotor SRMs can be seen in several industrial applications and home appliances. SRM rotor does not carry magnets and conductors. They are merely made of electric steel laminations that are mounted on the shaft. This makes the inner rotor SRM suitable for high-speed applications due to the superior mechanical integrity. The windage losses of salient-pole structures could be high at higher rotational speeds. Authors in [18] designed a cylindrical salient-pole inner rotor specifically for high-speed applications. The inner rotor still has a salient-pole structure, however, with very thin bridges connecting each rotor pole where those thin bridges are still built with the same magnetic core material. Thus, the rotor has a cylindrical outer surface which greatly reduces the windage losses. Those thin bridges heavily saturate during operation and can be magnetically viewed as an equivalent extended airgap. Inner rotors generally have small rotor radius which limits their torque generation capacity. This could be proven using Maxwell Stress Tensor method. The instantaneous torque could be estimated by (1.2).

$$Estimated Torque = L_s r^2 \int_0^{2\pi} f_t d\theta$$

$$f_t = \frac{B_n B_t}{\mu_0} \quad (1.2)$$

where f_t is the product of radial flux density and tangential flux density along the calculation contour placed in the middle of the airgap. Using line integration along the circular contour, the

tangential force density of the rotor could be estimated. The product of the square of contour radius and stack length of the rotor constitutes the torque.

Given (1.2), the torque is proportional to the square of the rotor radius and linearly proportional to length of the rotor stack. In fact, the radius of the inner rotor could be confined by a few factors such as the volume of the stator and windings. A large ratio between rotor radius and the machine outer diameter (OD) may not be often seen in medium size and small size motors. On the contrary, exterior-rotor machines generally have large rotor radiuses and higher output torques at low speeds. For radial flux machines, increasing stack length could always enhance the torque generation in both interior rotor and exterior rotor. In some applications, referred to as disc type machines, have constrains on machine length such as in-wheel drives. In this case, the top choice is axial flux machine which benefits from a relatively large axial pole surface. The large axial pole surface could provide reasonable flux linkages at aligned positions. The output torque of axial flux machine could be equal or greater than that of radial flux machine with a similar size. An axial flux machine could have one-sided rotor or two-sided rotor configuration. Due to the large axial surface and the strong axial electromagnetic force, the deformation of axial rotor could be a concern. To address this issue, the back-to-back rotor with double salient-pole structure is investigated. The back-to-back rotor is placed between the two axial stators such that the axial electromagnetic forces acting on both sides of the rotor will cancel each other. In addition, back-to-back rotor could be stacked up along the axial direction to superimpose output torques. Besides axial flux machine and radial flux machine, the double-salient pole structure can be converted into the linear version. For the linear version, the windings would be installed on the rails. Alternating excitation sequences could tract the rotor to move forward and backward.

The topologies of SRMs are listed in Figure 1.6. The way to read the map is to cascade the selection of each group from left to right, for example, the topology of “Double Salient-Pole Structure”, “Radial Flux”, “Higher Number of Stator Poles”, “Interior Rotor”, etc. The sample drawings of mentioned topologies are shown in Figure 1.7 to offer some geometrical insights. Multiple optimization methodologies are reviewed in [19]. Besides the major configurations shown in Figure 1.6, the shapes of stator poles and rotor poles take significant roles of determining the torque profiles in terms of average torque, torque pulsations, vibrations, and acoustic noise. Those topologies that fit in the scope of this thesis will be partially discussed in Chapter 2 and Chapter 3. Following trends of improvement of SRMs in the literature, the novel geometrical designs as applied to magnetic cores, winding configurations, new magnetic core materials, control methodologies will continue to evolve. This raises a question: if a machine is designed using the above perspectives, is it fair to say that the machine volume is fully exploited in terms of torque harvesting? The answer could be negative. And this study attempts to exploit the machine space from a new perspective, namely by developing a 3D flux structure. The 3D flux structure means to create both radial magnetic field and axial magnetic field in a machine. This surely augments the design scope. To avoid getting lost in fragmental ideas, the first version could be built with the use of the existing knowledge and methodologies. It also helps to solidify the reasoning and feasibilities of the concept.

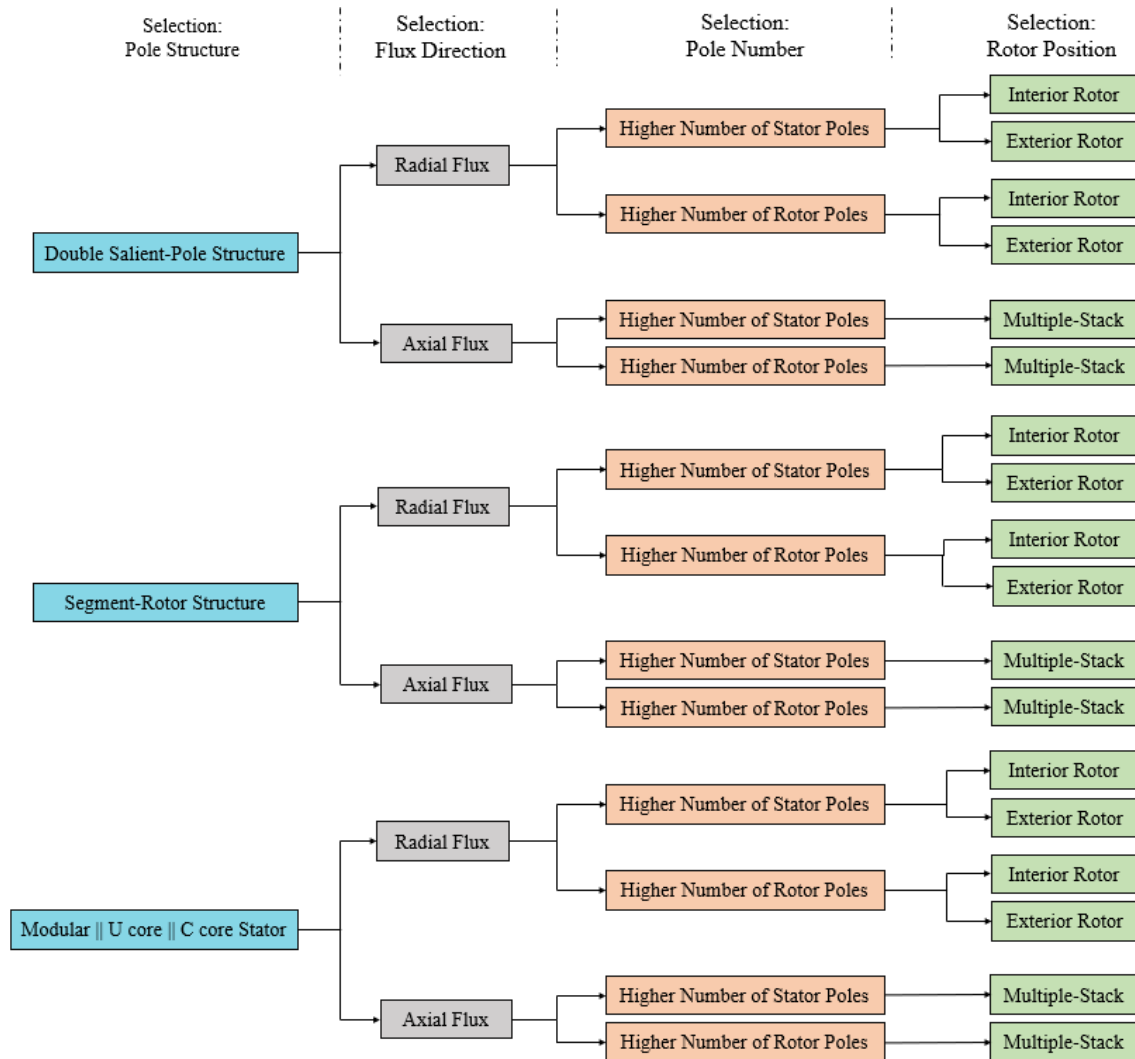


Figure 1.6: Summary of configurations of common SRMs.

The electrical machine is an electrical energy to mechanical energy converter. The electrical energy creates magnetic in a machine. The field interacts with the stator pole and rotor pole and forces the shaft to rotate. To create the field, armature windings are installed in the stator slots while parts of the copper conductors are placed in stator slots for forming the useful electromagnetic field and the remaining parts are left outside of the stator slots. Parts extended to the outside are called end windings which contribute to leaking magnetic field and additional copper losses. In addition, they occupy additional machine space.

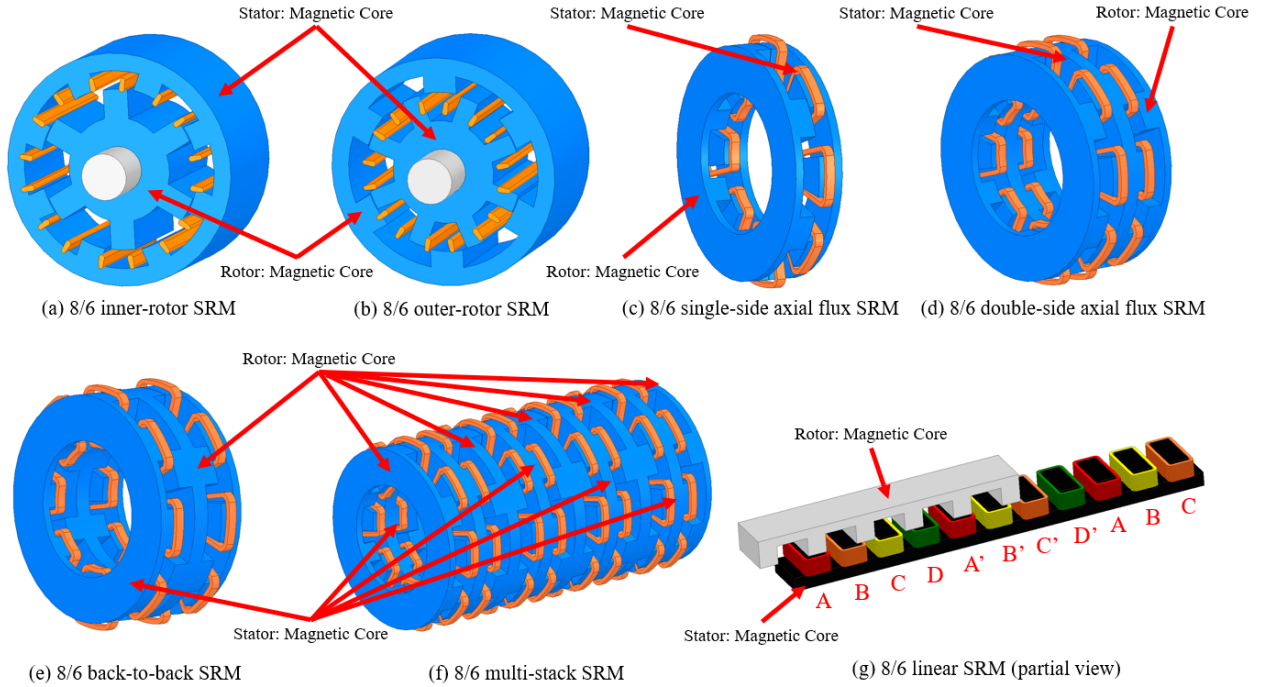


Figure 1.7: Sample drawings of multiple type SRMs: a) 8/6 inner-rotor SRM b) 8/6 outer-rotor SRM c) 8/6 single-side axial flux SRM d) 8/6 double-side axial flux SRM e) 8/6 back-to-back SRM f) 8/6 multi-stack SRM g) 8/6 linear SRM (partial view).

To develop higher torque, a larger copper area is usually preferred since flow of a larger current could strengthen the magnetic field. Unfortunately, the larger volume of end winding will emerge as a side effect of the larger copper area and yield more space and introduces additional thermal stress. Nowadays, the design flow of industry generally starts from confining the machine space and estimating the thermal stress. Consequently, the detailed machine dimensions are derived subject to constraints through iterative balancing and tradeoffs. Through our investigation, it was found that the proposed 3-D flux structure indirectly reduces the size of end windings. With the proposed structure, the machine space can be better exploited. The structure has been revised at least twice for seeking the maximized torque capacity and the optimized configuration subject to the constrains. Multiple magnetic field design and configurations have

been investigated. To clearly illustrate the design concepts step by step, this thesis is organized as follows:

In Chapter 2, the design concepts and process of the first version of proposed structure will be discussed in detail. The whole design process consists of multiple sub-design objectives with interrelated dependencies. Every sub-design objective is driven by fundamental logic of conventional machines. Pole configuration, winding configurations, geometrical layout, magnetic field design generally begin with preliminary ideas referring to conventional machines and are accordingly refined by the preferences of the 3D flux structure. At a high-level, those small steps are reasonably organized and linked to seek the theoretical advantages of the double-salient pole 3D flux structure. In addition, the advantages are validated by simulation results. Under design constraints, the parameters of a double-salient pole 3D flux machine are chosen while they could be changed subject to various design constraints. The inherent issue of the first-version structure is illustrated at the end of chapter to derive major revisions in the next steps. This study does not only validate the theoretical advantage of the proposed structure, but also investigates the best configuration of the machine subject to the constraints.

In Chapter 3, the machine structure is revised into a segmented-rotor version to get rid of the inherent issue of the double-salient pole structure. The operation and design concepts are different from those of the first version. The magnetic field, pole configuration, and winding configurations for segmented-rotor structures are studied where the pole configuration has deterministic superiority over other machine parameters. The theoretical advantage of the segmented-rotor structure is validated by the simulation results. Moreover, the practical value of the proposed structure is investigated in order to fabricate a physical prototype. This raises the

third-round revision on pole configurations because the magnetic imbalance of a 8/14 segmented-rotor machine may or may not yield unexpected failures. Vast parameters have been tried in the past to get rid of the magnetic imbalance issue. Fortunately, the suitable pole configuration, 10/18 is found. In this third version, the magnetic imbalance will not yield a potential failure. Furthermore, the advantages of the previous models can be fully inherited. The iteration process and reasonings are also included in Chapter 3. To clearly illustrate the magnetic field design, simulation results of flux distribution are demonstrated as well.

In Chapter 4, the global optimization method, Genetic Algorithm (GA) will be discussed. The cost function involves the weights for average torque and torque pulsation where the weight of average torque takes the lead since the objective of this study is to seek the maximum torque capacity of the proposed structure. Multiple machine parameters are involved in the optimization process. Those parameters are internally coupled and have significant impact on the saturation patterns and the flux density distribution. The GA optimization is the inner loop of the whole design process. The scope of the GA optimization is minimized for reducing the computational cost. It is the inner loop of the whole design process and is only activated after the parameters belonging to outer loop are locked. Parameters belonging to outer loop involves, machine OD, stator ID, stack length, pole configuration, winding turns, etc. To avoid unnecessary computations, which costs extra time, the parameters of outer loop are fixed through a preliminary trend study.

In Chapter 5, the results of multi-physics and co-simulation results of the 10/18 3D flux SRM will be presented. Since in Chapter 2 and Chapter 3, partial simulation results of early-stage models have been demonstrated for explaining the behavior of the magnetic field, they are not

presented in this chapter again. The advantages of the proposed model have been validated by previous simulated results. The main objective of this chapter is to address concerns of mechanical integrity of the scaled-down model and present its torque capacity.

In Chapter 6, the modifications and down scaling applied to the prototype machine by fabrication process are discussed. Since the proposed structure could be designed for future machines, mechanical complexities in the fabrication process are addressed. The basic operations of the manufactured prototype are presented. The very fundamental experimental results will be presented.

The conclusion will be presented in Chapter 7. The design concepts and achievements of this thesis will be reviewed.

CHAPTER 2

3D FLUX SRM WITH SALIENT POLES

The primary objective of the 3D flux structure is to exploit maximum torque from a given machine space. The approach to achieve this goal starts from a high-level vantage to engage the maximum space within the machine in electromechanical energy conversion. It does not focus on detailed machine dimensions such as stator pole designs or rotor pole designs. It seeks the possibility to exploit all three inner surfaces of a machine, two axial surfaces and one cylindrical surface. Both radial magnetic structure and axial magnetic structure are expected to be present in the proposed structure and simultaneously generate torque. To demonstrate a clear derivation, this chapter consists of four parts: a) principles of operation in conventional SRMs b) the magnetic paths of the common topologies c) the proposed 3D flux structure d) the first version of the 3D flux SRM with double-salient pole structure.

2.1 Principles of operation

8/6 and 6/4 double salient pole SRMs are commonly seen in industrial applications and academic publications. A double-salient pole structure means that a machine has salient stator poles and salient rotor poles. As a salient rotor pole rotates towards a stator pole, the magnetic reluctance of the magnetic paths linking the stator pole, rotor pole, and air gap decreases while the magnetic reluctance increases once a rotor pole moves towards a stator pole. From an energy conversion point of view, assuming that phase currents are constant, $0.5I^2 \frac{\Delta L}{\Delta \theta}$ determines the instantaneous torque at an arbitrary rotor position where the inductance L is overall increasing from unaligned rotor position toward aligned rotor position. L is inversely proportional to the magnetic

reluctance \mathcal{R} such that the magnetic reluctance of magnetic paths is expected to keep decreasing along the path towards alignment. This is because, the resultant airgap between stator pole and aligning rotor pole reduce along the route towards full alignment. Figure 2.1 describes relationships between the rotor position, phase inductance, excitation, and flux linkages. As shown in Figure 2.1 (b), increasing the excitation current tend to induce magnetic saturation. This, in turn, reduces the magnitude of the inductance and alters the inductance profile. At the unaligned position, the rotor pole is quite far away from the stator pole and there is a large airgap in between. The magnetic permeability is the well-known constant μ_0 . The relative permeability of air or vacuum is 1 resulting in a large reluctance at unaligned position. The relative permeability of magnetic cores under unsaturated condition is normally very large (100's to 1000's). The corresponding magnetic reluctance of unsaturated magnetic steel is negligible, compared to that of airgap. The reluctance of airgap dominates the phase reluctance at the unaligned position. In other words, different excitations would not result in significant differences in terms of the phase inductance at unaligned position. As the rotor poles move closer to the edges of the stator poles, the physical airgap shrinks. The equivalent airgap still dominates the phase reluctance at this moment. Before a rotor pole begins to overlap with a stator pole, the corner tip of that stator pole may saturate in advance due to the limited core area through which an inrush of magnetic flux occurs. Once a rotor pole actually overlaps with the approaching stator pole, the phase inductance apparently increases till the rotor pole fully aligns with the stator pole.

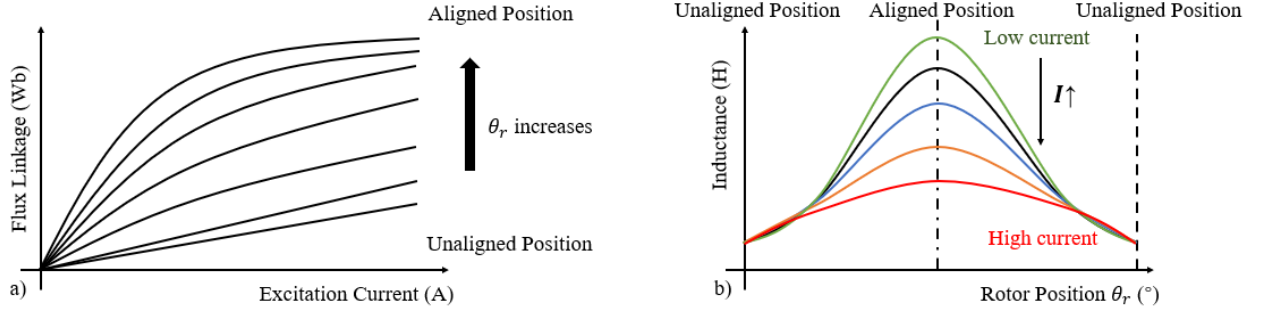


Figure 2.1: a) Flux Linkage versus Excitation b) Inductance versus Rotor Position.

It is worthy to note that the high magnitude of phase inductance profile under low excitation does not translate to a higher torque capacity of the machine. As shown in the Figure 2.1(a), the deterministic term is the flux linkage (Ψ) which could be presented as the product of the excitation and phase inductance (2.1.1). The product of peak flux linkage and excitation is the total energy of the machine (2.1.2). The total energy consists of field energy and co-energy (2.1.3). The derivative of total energy with respect to time is shown in (2.1.4).

$$\Psi(i, \theta_r) = L(i, \theta_r) \times i \quad (2.1.1)$$

$$W_{total} = \Psi(i, \theta_r) \times i \quad (2.1.2)$$

$$W_{total} = W_F + W_C \quad (2.1.3)$$

$$\frac{dW_{total}}{dt} = \frac{d\Psi(i, \theta_r) \times i}{dt} = \frac{\partial \Psi(i, \theta_r) \times i}{\partial i} \frac{di}{dt} + \frac{\partial \Psi(i, \theta_r) \times i}{\partial \theta_r} \frac{d\theta_r}{dt} \quad (2.1.4)$$

Substitution of (2.1.2) into (2.1.4) yields (2.1.5)

$$\begin{aligned} \frac{\partial (W_F + W_C)}{\partial i} \frac{di}{dt} + \frac{\partial (W_F + W_C)}{\partial \theta_r} \frac{d\theta_r}{dt} &= \Psi(i, \theta_r) \times \frac{di}{dt} + i \times \frac{\partial \Psi(i, \theta_r)}{\partial i} \frac{di}{dt} + i \times \frac{\partial \Psi(i, \theta_r)}{\partial \theta_r} \frac{d\theta_r}{dt} \\ &= \left(\Psi(i, \theta_r) + i \times \frac{\partial \Psi(i, \theta_r)}{\partial i} \right) \frac{di}{dt} + \left[i \times \frac{\partial \Psi(i, \theta_r)}{\partial \theta_r} \frac{d\theta_r}{dt} \right] \end{aligned} \quad (2.1.5)$$

Knowing that derivative of rotor position (θ_r) with respect to time (t) is the rotational speed ω_r and that the mechanical power should be a product of torque and rotation speed as (2.1.6). In addition, it is assumed that the excitation current is kept constant along the movement such that

the derivatives of the current with respect to time equals 0. The derivatives of energy terms, W_F and W_C with respect to current will be equals to 0 as well. Also, it is known that the stored field energy does not contribute to torque harvesting. The torque equation could be re-arranged as (2.1.7).

$$\text{Mechanical power} = T \times \omega_r \quad (2.1.6)$$

$$T = i \times \frac{\partial \Psi(i, \theta_r)}{\partial \theta_r} - \frac{\partial W_F}{\partial \theta_r} = \frac{\partial W_C(i, \theta_r)}{\partial \theta_r} \quad (2.1.7)$$

Assume that the (2.17) is a piecewise curvature with very fine steps and the operating point stays in unsaturated region under an arbitrary magnitude, then (2.1.7) could be rewritten as (2.1.8).

$$T = \frac{\partial W_C(\theta_r)}{\partial \theta_r} = \frac{\int i \times L(\theta_r) di}{\partial \theta_r} = \frac{1}{2} \times i^2 \times \frac{dL(\theta_r)}{d\theta_r} \quad (2.1.8)$$

As a quick estimation, by ignoring the potential curved part of the co-energy, the area integral of incremental co-energy over the span of rotor position represents the average torque. The estimation is expressed as (2.1.9).

$$\tilde{T} = \frac{W_C(\theta_{end}, i) - W_C(\theta_{start}, i)}{\theta_{end} - \theta_{start}} = \frac{1}{2} \times i^2 \times \frac{L(\theta_{end}, i) - L(\theta_{start}, i)}{\theta_{end} - \theta_{start}} \quad (2.1.9)$$

Considering the saturation and the nonlinearity of the magnetic curve, the co-energy is the area integral along the flux linkage curve with respect to the excitation as presented by the green region in Fig.2.2 (a). Assuming that the excitation current i_1 is constant along the rotation, the increment in co-energy from the unaligned position to aligned position is shown as the green region in Figure 2.2 (b) where the i_1 is sufficiently large to shift the operating point into a saturated region. Assuming that i_2 is insufficiently large to shift the operating point into saturation. The area integral of increment in co-energy due to i_2 is shown as the orange region in Figure 2.2 (c). Admittedly, the contrast between Figure 2.2 (b) and Figure 2.2 (c) is slightly

exaggerated while the benefit of operating a SRM in the saturation region is apparent. This is the reason why SRMs are generally forced to operate in saturated regions.

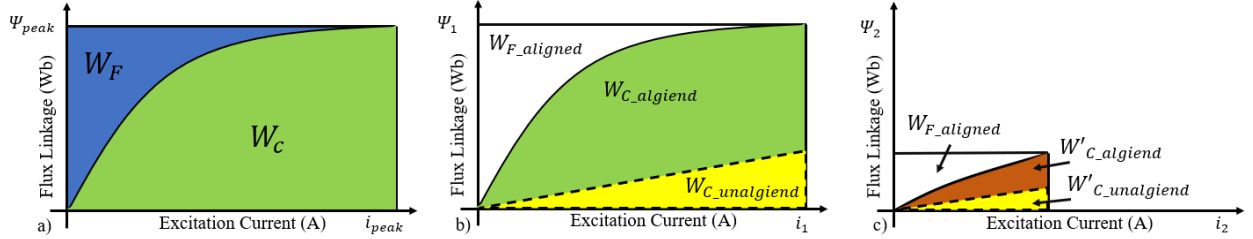


Figure 2.2: Plots of magnetic energy.

By fixing the excitation current, the locus of the operating point moves along the magnetic energy cycle which is shown in Figure 2.3 (a). The operating point starts from an unaligned position under zero excitation where the transient of phase current is ignored. At this moment, the rotor position still stays at the unaligned position. The co-energy at the unaligned position (shaded region in Figure 2.3a) is built. Then, the operating point migrates through different curves along the rotation from an unaligned position towards an aligned position. At each rotor position, there is a corresponding flux linkage curve matching due to the variant magnetic reluctance. Once the rotor position passes the aligned position, the excitation current is expected to immediately drop to zero to avoid negative torque generation. Meanwhile the field energy will return to the power source. The locus of the operating point in ideal case is presented by red arrows in Figure 2.3 a). Power converters would be the interfaces to feed excitations into SRMs. In practice, the phase current is never a clean rectangular waveform without current ripples. To regulate the phase current, power devices keep turning ON and OFF and switch the sign of voltage across the phase winding. At a given time, the voltage across a phase winding could be zero, positive DC bus voltage, or negative DC bus voltage. Since phase windings are combinations of inductance and resistance, current flows through phase windings should not

present sharp transients unless fault conditions occur. By chopping patterns, phase currents present chattering with different magnitudes around the current reference.

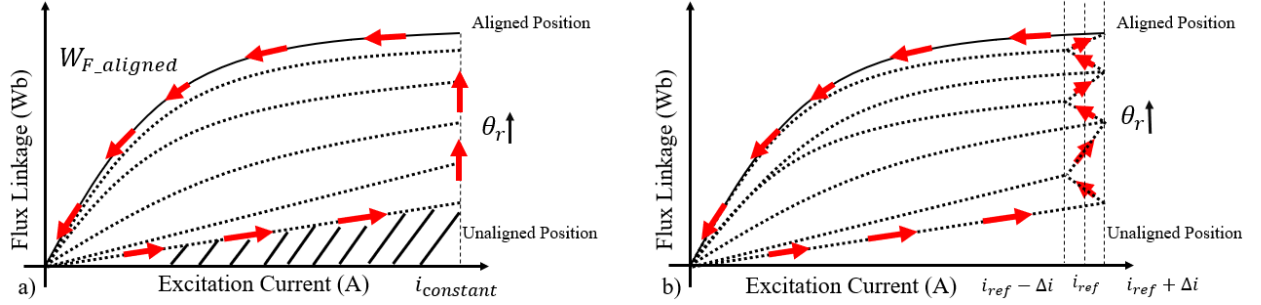


Figure 2.3: a) the ideal locus of operating point b) the locus of operating point under chopping.

Regardless of the DC bus voltage, the current ripples could be greatly smoothed out by rapid switching. However, doing so will increase switching losses and power consumption of the driver circuit. In Figure 2.3 b), the chattering in the locus is due to chopping which could take a small portion of magnetic energy away. The smooth locus of magnetic energy for torque generation is presented in Figure 2.3 a) which may not be seen in real measurement. However, it is still used for evaluating the machine design for simplicity. In unsaturated regions, the magnetic field energy W_F approximately equals to the magnetic co-energy W_c due to the semi-straight slope of $\Psi(i, \theta_r)$. Both field energy and co-energy take half of the total energy. As the saturation occurs, $\Psi(i, \theta_r)$ becomes more nonlinear and presents a knee point. Co-energy occupies more than 50% of the total energy while the magnetic field energy is suppressed. This is an expected situation because the field energy is used in a more efficient way. Note that the saturation discussed here does not mean bulk saturation in machine cores. In an SRM, saturation tends to occur in tips and corners of stator poles and rotor poles. If the body saturation occurs in SRM, the core loss could be unacceptable. Also, the bulk saturation could have negative impacts on airgap energy and overall field distributions. For instance, the output torque could be greatly

reduced. After all, the electromagnetic energy conversion should occur in the airgap. Given (2.1.8), the magnitude of reluctance torque is not quite related to the peak of inductance but derives from the changes of the inductance along the movement. It is preferred to have phase inductance profiles to steadily increase. For some designs, the inductance profiles show slight flat top nearby aligned positions. This is because a phase needs to discharge its magnetic energy when the rotor position passes the aligned position in order to avoid generation of negative torque. In fact, the energy stored in inductors cannot be discharged immediately. The turn-off current tails of excitations are inevitable such that excitations could be turned off in advanced before rotor position reaches the aligned position. In practice, the span of a phase inductance profile may not be fully exploited when the machine speed is built up. Thus, the flat regions in phase inductance profile are sometimes designed to provide a safe window for turn-off current transients.

2.2 Fundamental Magnetic Design

Magnetic paths and flux plots are significant indicators of torque generation capacity of any SRM. No matter how outstanding a machine configuration is, the winding configurations, pole configurations, structures, and other properties are all served to form the desired magnetic field. Before designing an electric machine, one would have some rough ideas of the expected magnetic field layout. Consequently, one tries out feasible combination of machine properties. If the designed magnetic field is difficult to achieve under design constraints, the field distribution can be changed while keeping the desired pattern. At a high level, the design process is similar to a large dynamic network with nodes representing machine properties. Each node could offer multiple options. Once parameters of a few nodes are fixed, there will be some corresponding

nodes or options that are out of Table Depending on combinations of parameters or the sequences of parameter selections, the mesh network could present different patterns. It is desired to have high level understandings of design flows and machine parameters at the very beginning to avoid total reworking or design conflicts at later phases of machine design. Thus, reviewing the fundamental design principles of conventional SRMs at first could be helpful for highlighting the main map of the proposed structure. To study the magnetic paths and field distribution, a 6/4 conventional inner rotor SRM is simulated via the 2D finite element analysis (FEA) commercial package Maxwell. The flux lines of the 6/4 SRM model at unaligned position and aligned position are presented in Figure 2.4 where the rotor rotates in counterclockwise (CCW) direction. The closed-loop contours are flux lines presenting magnetic paths. By increasing the divisions of the Wb/m, more flux lines with a finer division could be seen. At the unaligned position, the stator pole, S_{p1} attempts to attract the rotor pole, R_{p1} . Due to the symmetrical design, the stator pole, S_{p4} attempts to simultaneously attract the rotor pole, R_{p3} as well. By the nature of the reluctance machine, rotor poles always tend to align with the active stator poles to form the magnetic paths with minimal magnetic reluctances. The large airgap between the S_{p1} and R_{p1} places decent magnetic reluctance in each magnetic path. Along the movement, the airgap in between shrinks. Assuming that the reluctances of the magnetic core under local saturation is still way less than the airgap reluctance, the overall reluctances of magnetic paths are minimized at the aligned position. The simplified magnetic circuits are shown in Figure 2.5 where the irrelevant conductors are hidden.

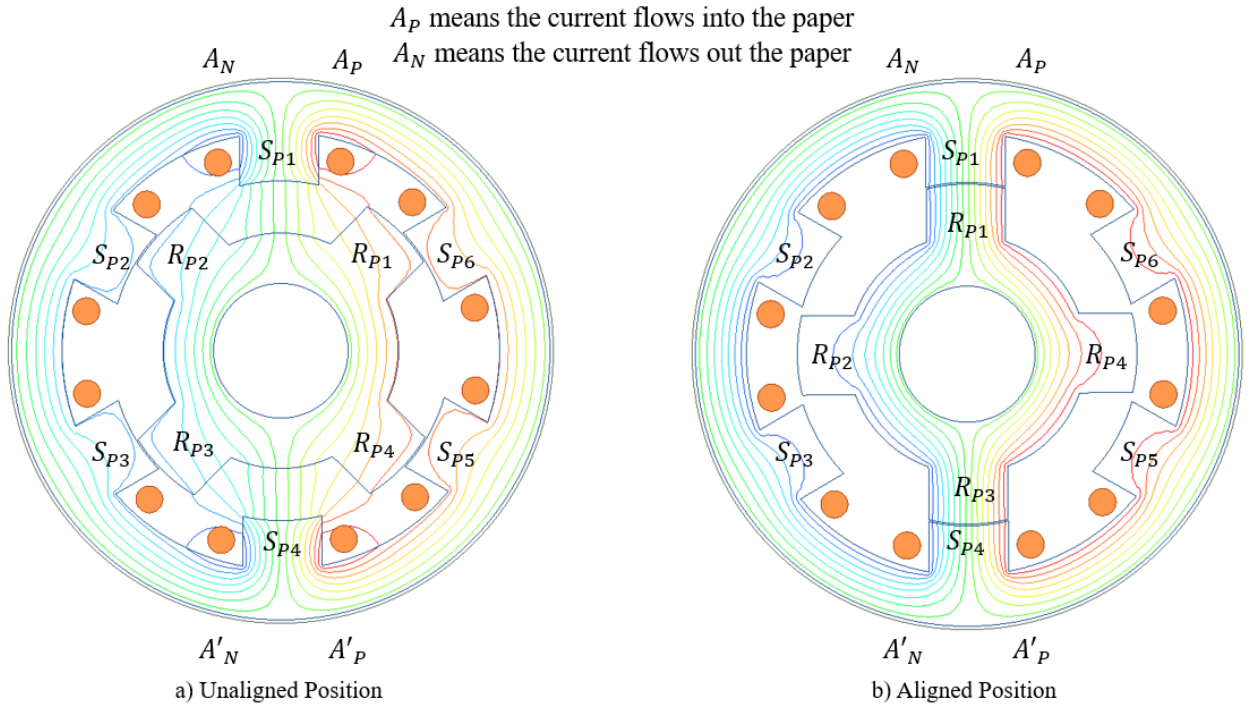


Figure 2.4 Flux lines of a 6/4 SRM: a) unaligned position b) aligned position.

The lumped-parameter magnetic circuit are commonly seen in the literature. For 2D magnetic designs with simple structures, the lumped-parameter magnetic circuit could offer sufficient accuracy. As complexities of machine design increases, the lumped-parameter magnetic circuit may not be the most efficient approach compared to numerical methods. In this study, the magnetic circuits are used for illustrating the operational principle of machines. The magnetic circuit shown in Figure 2.5 only present one magnetic path of a half model for simplicity. There should be multiple magnetic paths as shown in Figure 2.4. The location and strength of each path could be different. Some of flux lines link the stator magnetic core and rotor magnetic core. Some of them present local leakage flux caused by the fringing effects. The circuit shown in the following figure is to present the principle of operation in the machine.

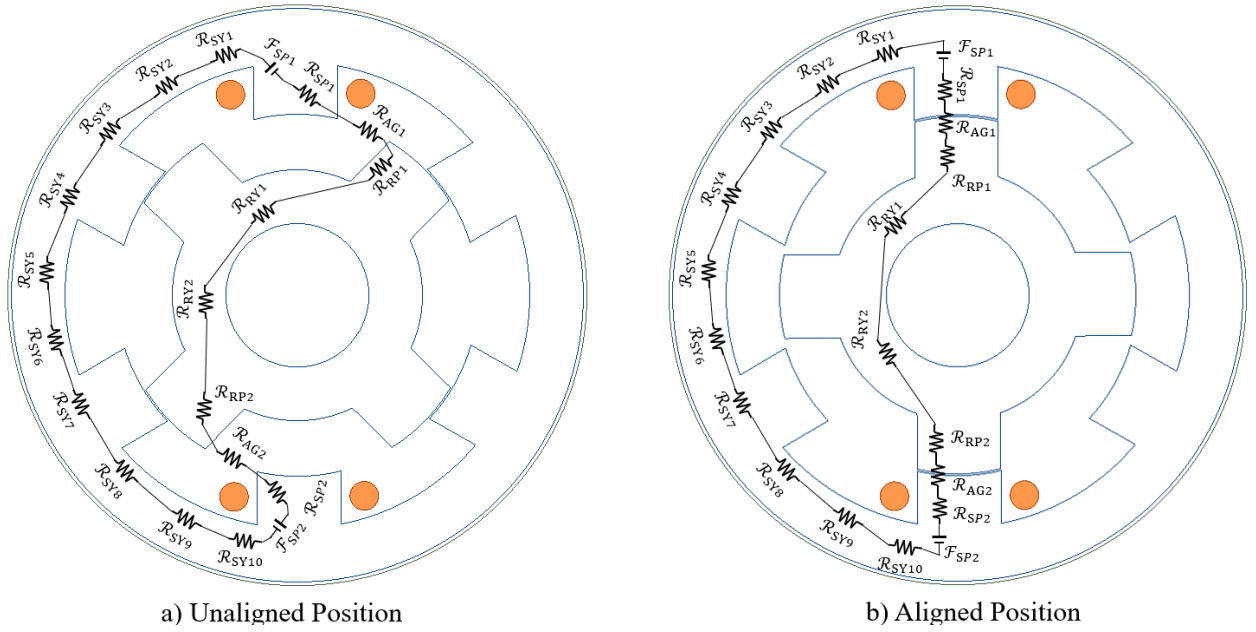


Figure 2.5: The simplified magnetic circuit of one magnetic flux path of a 6/4 SRM.

The denotation of used terms are as follows:

\mathcal{R}_{RP1} and \mathcal{R}_{RP2} : reluctances of the rotor poles

\mathcal{R}_{AG1} and \mathcal{R}_{AG2} : reluctances of the airgap

\mathcal{R}_{SP1} and \mathcal{R}_{SP2} : reluctances of the stator poles

\mathcal{R}_{RY1} and \mathcal{R}_{RY2} : reluctances of the rotor yoke

\mathcal{R}_{SY1} to \mathcal{R}_{SY10} : reluctances of the stator yoke

\mathcal{F}_{SP1} and \mathcal{F}_{SP2} : magnetic motive force of winding mounted on the stator poles.

The above symbols are high-level representations of the localized reluctance. All of them are multi-parameter dependent functions. The excited windings generate magnetomotive force (MMF) $N \times i$ and could be viewed as a magnetic “voltage source”. Multiple magnetic paths connect to the magnetic “voltage sources” in parallel. The summation of \mathcal{F}_{SP1} and \mathcal{F}_{SP2} is the total MMF. As aforementioned, the airgap reluctance is assumed to dominate over the others

regardless of local saturations in machine core. If bulk saturation does not occur in the machine core, the variations of reluctances in the stator poles, stator yoke, rotor poles, and rotor yoke may not be quite significant, compared to the airgap reluctance. In an alignment process, the reduction in \mathcal{R}_{AG1} and \mathcal{R}_{AG2} enlarges the phase inductance and the strength of the magnetic flux. This could be explained by the following equations (2.2.1) through (2.2.10).

$$\mathcal{R}_{path1} = \sum_{i=1}^n \mathcal{R}_{SPi} + \sum_{i=1}^m \mathcal{R}_{SYi} + \sum_{i=1}^p \mathcal{R}_{RPI} + \sum_{i=1}^q \mathcal{R}_{RYi} + \sum_{i=1}^s \mathcal{R}_{AGi} \quad (2.2.1)$$

where n , m , p , q , and s are the upper limits denoting the numbers of sections of each group. The reluctances of leakage flux paths are not included here and are neglected.

The analytical equations of magnetic reluctance are (2.2.3) and (2.2.4)

$$\mathcal{R} = \frac{l}{\mu_0 \mu_r A} \quad (2.2.3)$$

where μ_0 is the permeability of vacuum, equals to $4\pi \times 10^{-7} \frac{H}{m}$. μ_r is the relative magnetic permeability of the material. A is the cross-sectional area of the objective. l is the length of the circuit.

$$\mathcal{R} = \frac{\mathcal{F}}{\Phi} \quad (2.2.4)$$

The magnetic flux could be written as (2.2.5) where N denotes for the number of turns of windings. Also, it is known that the inductance could be represented by (2.2.6) where i denotes the phase current. Thus, the phase inductance could be rewritten as (2.2.7).

$$\Phi = \frac{\mu_0 \mu_r N i A}{l} \quad (2.2.5)$$

$$L = \frac{\Phi(i)}{i} \quad (2.2.6)$$

$$L = \frac{N^2}{\mathcal{R}} \quad (2.2.7)$$

Substitution of (2.2.1) into (2.2.7) yields (2.2.8).

$$L_{path1} = \frac{N^2}{\sum_{i=1}^n \mathcal{R}_{SPi} + \sum_{i=1}^m \mathcal{R}_{SYi} + \sum_{i=1}^p \mathcal{R}_{RPi} + \sum_{i=1}^q \mathcal{R}_{RYi} + \sum_{i=1}^s \mathcal{R}_{AGi}} \quad (2.2.8)$$

Considering the high permeability of magnetic cores under unsaturated conditions, (2.2.8) could be simplified as (2.2.9).

$$L_{path1} = \frac{N^2}{\sum_{i=1}^n \mathcal{R}_{EAI} + \sum_{i=1}^m \mathcal{R}_{AGi}} \quad (2.2.9)$$

where \mathcal{R}_{EAI} denotes the reluctance the equivalent airgap. The reluctances of unsaturated magnetic cores are ignored since the reluctances of airgap could be two to three orders of magnitude higher than them. However, the term corresponding to equivalent airgap could be added into the equation where the equivalent airgap adheres to the saturated thin layer and conners of stator poles and rotor poles. This term may or may not be considerable depending on the saturation level and the airgap length. Common airgaps could vary between 0.3mm to 0.5mm in small and midsize SRMs. The airgap of 0.2mm have been seen in some commercial products with the elaborated mechanical design. As the airgap becomes smaller, the term of equivalent airgap could become significant. Given this, (2.2.4) could be rearranged as (2.2.10).

$$\Phi_{paht1} = \frac{\mathcal{F}}{\sum_{i=1}^n \mathcal{R}_{EAI} + \sum_{i=1}^m \mathcal{R}_{AGi}} \quad (2.2.10)$$

Since multiple magnetic paths coexist in the machine cores as shown in Figure 2.4, the total phase reluctance could be written as (2.2.11). The phase inductance could be approximated as (2.2.12).

$$\mathcal{R}_{phase} = \frac{1}{\sum_{i=1}^n \frac{1}{\mathcal{R}_{pathi}}} \quad (2.2.11)$$

$$L_{path1} = \frac{N^2}{\mathcal{R}_{phase}} = N^2 \times \sum_{i=1}^n \frac{1}{\mathcal{R}_{pathi}} \quad (2.2.12)$$

The analytical reluctances of terms in Figure 2.5 could be written as (2.2.13) through (2.2.20).

The radius, length, and arcs are marked in Figure 2.6 for illustration. The cross-section area of each reluctance term is denoted separately. The magnetic circuit is similar to an electrical circuit.

In a magnetic path, the magnetic flux is identical everywhere. Also, the total magnetomotive force is a constant number. By iteratively solving multiple magnetic flux paths, the flux distribution in the magnetic core could be approximated.

$$\mathcal{R}_{RP1} = \frac{L_1}{\mu_0 \mu_{rRP1} A_{RP1}} \quad (2.2.13)$$

$$\mathcal{R}_{RP2} = \frac{L_1}{\mu_0 \mu_{rRP2} A_{RP2}} + \frac{2\pi R_2}{\mu_0 \mu_{rRP2} A_{RP2}} \times \frac{\theta_6}{360} \quad (2.2.14)$$

$$\mathcal{R}_{SP1} = \frac{L_2}{\mu_0 \mu_{rSP1} A_{SP1}} + \frac{2\pi R_2}{\mu_0 \mu_{rSP2} A_{SP1}} \times \frac{\sum_{i=3}^{i=5} \theta_i}{360} \quad (2.2.15)$$

$$\mathcal{R}_{SP2} = \frac{L_2}{\mu_0 \mu_{rSP2} A_{SP2}} \quad (2.2.16)$$

$$\sum \mathcal{R}_{SYi} = \frac{2\pi R_3}{\mu_0 \mu_{rSY} A_{SY}} \times \frac{\sum_{i=5}^{i=8} \theta_i}{360} \quad (2.2.17)$$

$$\sum \mathcal{R}_{RYi} = \frac{R_1}{\mu_0 \mu_{rRY} A_{RY}} \times \frac{\theta_8 + \sum_{i=2}^{i=5} \theta_i}{360} \quad (2.2.18)$$

$$\mathcal{R}_{AG1} = \frac{R_2}{\mu_0 \mu_{rAG1} A_{AG1}} \times \frac{\theta_2}{360} \quad (2.2.19)$$

$$\mathcal{R}_{AG2} = \frac{R_2}{\mu_0 \mu_{rAG2} A_{AG2}} \times \frac{\theta_7}{360} \quad (2.2.20)$$

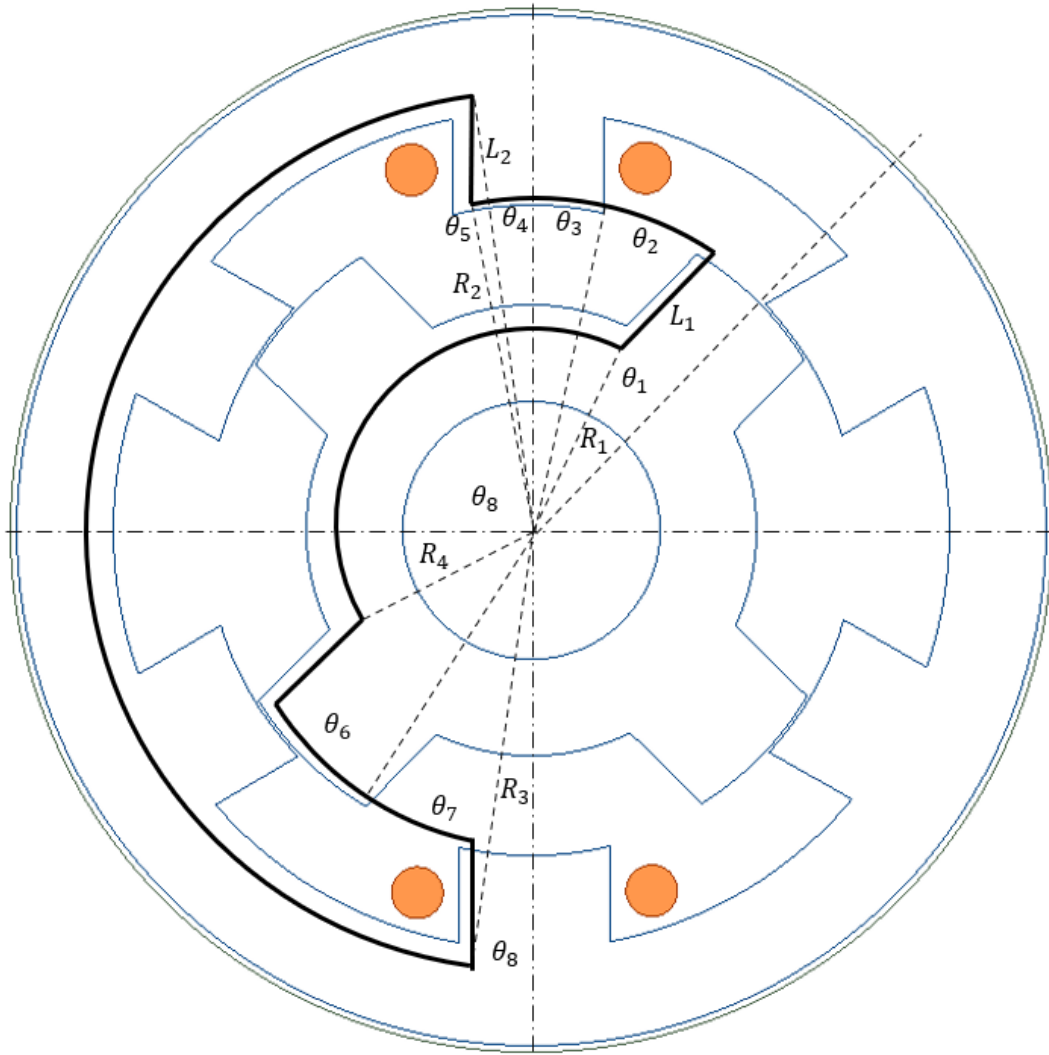


Figure 2.6: The dimension drawing of the 2D model.

In the past, one would use lumped parameters to estimate the flux field in the machine, however, the calculation is tedious, and the accuracy may not always be satisfactory. Nowadays, researchers attempt to improve the analytical method for the better accuracies. [28] mapped more than 10 magnetic flux paths to the 2D model and solved all analytical magnetic equation iteratively. The analytical results are compared with the FEA results, and they are close. Per Miller's book [6], the positive torque zone for each phase is the range from an unaligned position to the nearby aligned position. In this torque zone, the machine could generate positive torque

from one active phase. However, this is not the efficient way to operate the machine because it does not fully harvest the available torque. To maximally harvest torque, multiple phases should be simultaneously energized by patterns of strokes. Over the period of every stroke, the magnetic core could be fully utilized. The positive torque harvested from adjacent phases could be somehow superimposed to the output torque. In general cases, the positive torque zone and stroke could be defined as (2.2.21) and (2.2.22) [6].

$$\theta_{positive\ torque} = \frac{360^\circ}{2 \times N_r} \quad (2.2.21)$$

$$\theta_{stroke} = \frac{360^\circ}{N_{phase} \times N_r} \quad (2.2.22)$$

where N_r denotes the rotor pole number. N_{phase} denotes the number of phases. The better way to interpret the stroke and positive torque zone could be summarized as Table 2.1. $\theta_{overlap1}$ denotes the span of the active phase overlapping with the outgoing phase. $\theta_{overlap2}$ denotes the span of the active phase overlapping with the incoming phase. The interpretations of those for common 3-phase and 4-phase machines are slightly different.

Table 2.1: Positive Torque Zone and Stroke of Common Topology

	6/4 SRM	8/6 SRM	12/8 SRM	16/12 SRM
$\theta_{positive\ torque}$	45°	30°	22.5°	15°
$\theta_{overlap1}$	15°	15°	7.5°	7.5°
$\theta_{overlap2}$	15°	15°	7.5°	7.5°

To keep the consistency, the discrepancy of positive torque zone and stroke will be illustrated by the 06/04 2D model shown in Figure 2.4. The geometry of the example 2D model is summarized in Table 2.2. The inductance profile of single phase from an unaligned position to an aligned

position under single phase excitation is shown in Figure 2.7 a. The inductance profile of the same phase from an unaligned position to an aligned position under strokes is shown in Figure 2.7b. The torque profiles under single phase excitation and stroke excitation sequences are shown in Figure 2.8 where the current density is assigned a few distinct values to illustrate the previous discussion. Figure 2.9 provides examples of single-phase excitation and stroke excitation sequences. In a 6/4 SRM, the full cycle of the excitation sequence is 90° which is the span of three strokes. Since the FEA mesh quality has considerable impacts on the calculation results it must be noted that the accuracy is linearly proportional to the mesh quality and hence computation time. To demonstrate this observation, the minimal mesh length is chosen to be 2mm. The simulation results are collected and presented in Figure 2.7 and Figure 2.8. For the simulation results of stroke excitation, each phase is turned off in advanced by 0.5 mechanical degree to avoid commutation at the exact aligned position. The model without proper optimization is only used for presenting the idea and as a result the static torque ripple is way larger than what is observed in practice.

Table 2.2: Sample parameters

Machine Parameters	Quantities
Stator OD	160mm
Stator ID	101mm
Rotor OD	100mm
Stator Pole Arc	27°
Rotor Pole Arc	27°
Copper Area	244mm^2
Stack length	1m
Number of branches per phase	10
Number of turns per branch	100
Airgap	0.5mm

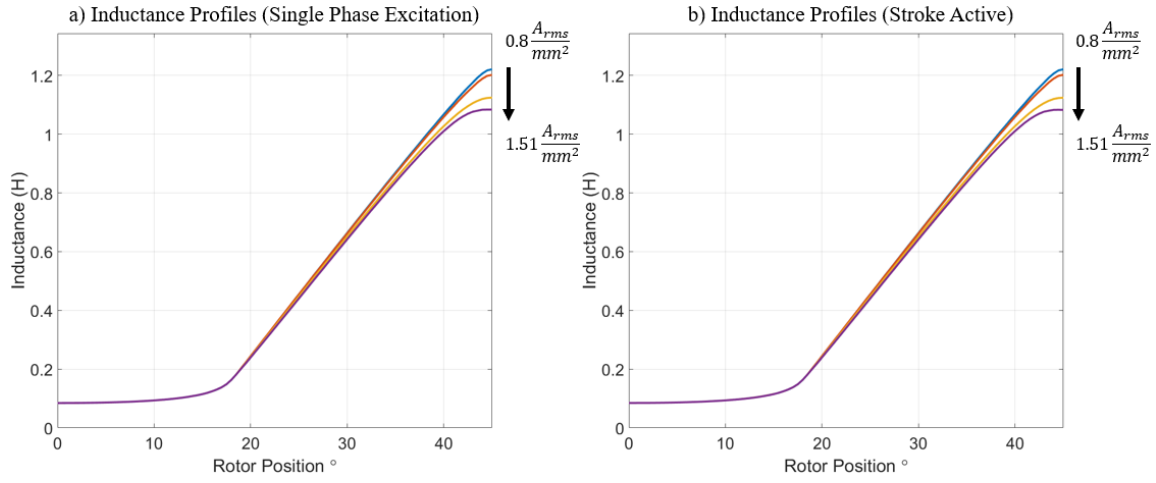


Figure 2.7: Self Inductance of Phase A: a) single phase active b) stroke active.

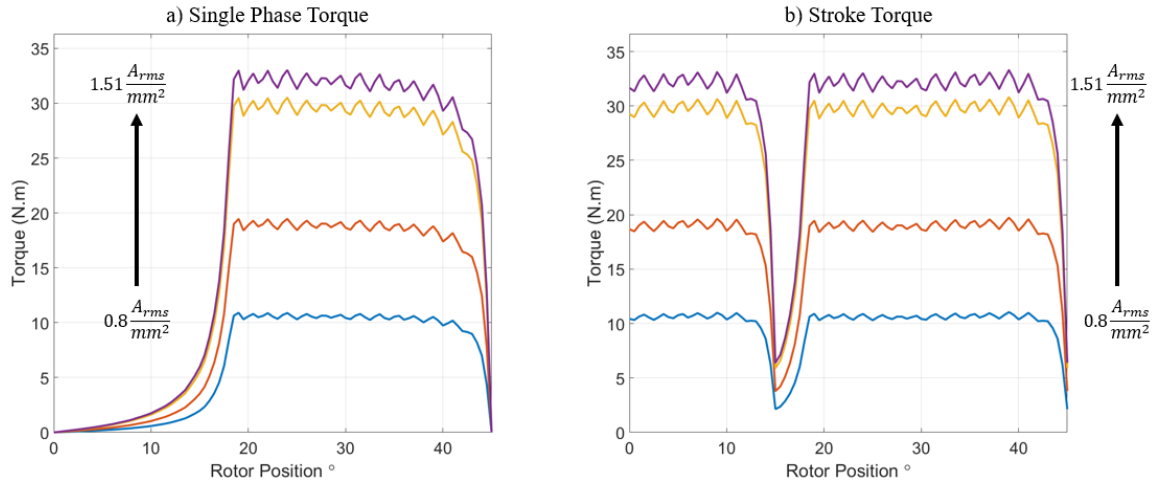
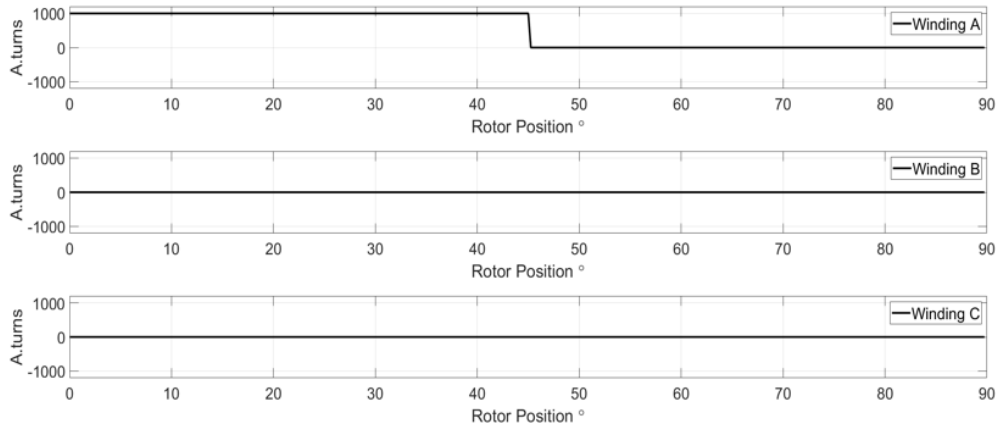
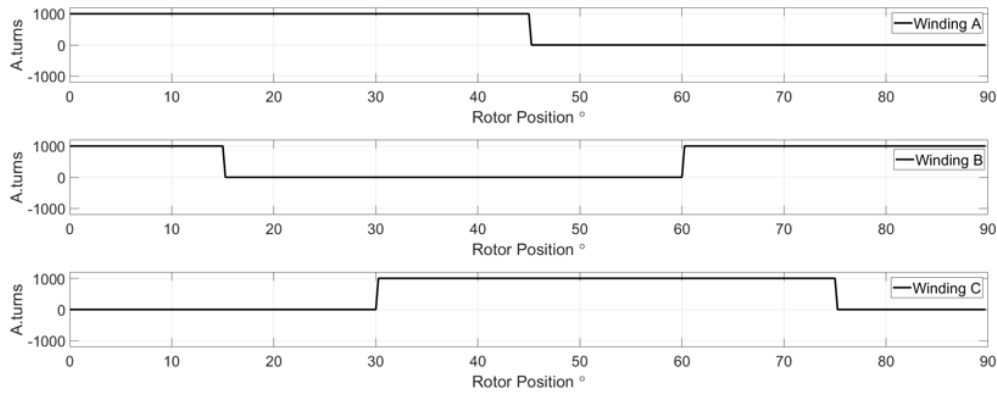


Figure 2.8: Torque Profiles: a) Single Phase Torque (Phase-A active) b) Stroke Torque.

In Figure 2.7, the machine operates in unsaturated region. The stroke torque could be viewed as the summation of single phase torques stemming from phase A, phase B, and phase C. Even though Figure 2.8 only shows one stroke, it is easy to observe that the commutation torques at 45° are identical with those at 15° . Figure 2.9 shows the points of commutation at 15° , 30° , 45° , 60° , 75° , and 90° . In Figure 2.8a), the single-phase torque is asymmetric due to the absence of proper optimization. Thus, the torque dips are only present every 30° .



a) Single Phase Excitation (Phase A)



b) Normal Excitation Sequences (Stroke Active)

Figure 2.9: Single phase excitations and normal excitation sequences.

In fact, magnetic paths formed by multiple active phases are different from those that are due to single phase excitation such that the stroke torque in practice may not be always the exactly superimposed version of single phase torque waveforms. The discrepancies could be due to the short magnetic paths formed by adjacent active phases. Such a short magnetic path is presented in Figure 2.10. By reviewing the flux lines in Figure 2.10 a, one can note that the short magnetic flux paths formed by double-phase excitation seemingly does not impact torque generation considering the large airgap between the stator pole #1 and rotor pole #1. As a result, the majority of fluxes link stator pole #2, rotor pole #2, rotor pole #4, and stator pole #5 since the airgap of Phase B is about to minimized at the aligned position. This could be explained by a few

aspects including the pole configurations and absence of optimization for pole geometries.

However, short magnetic flux paths do have considerable impact in many SRM applications and play a key role in the proposed structure. The corresponding reasons will be explained in the next subsection. The equivalent magnetic flux paths are shown in Figure 2.10 b).

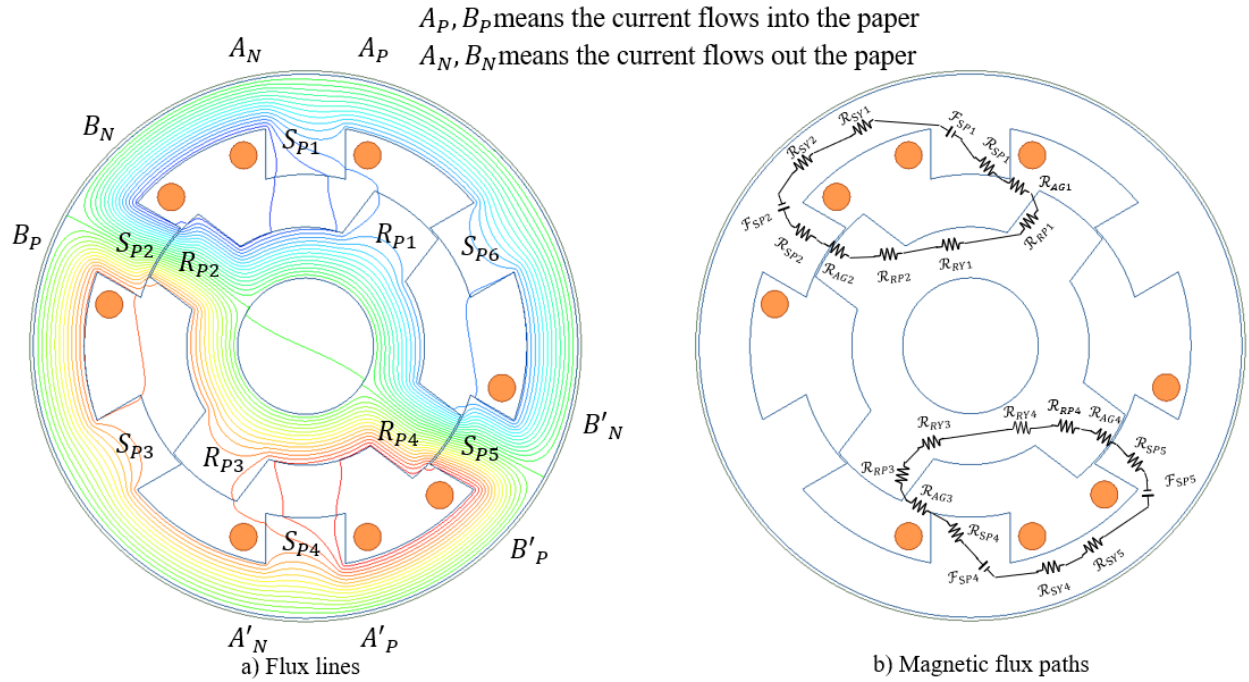


Figure 2.10: The short magnet flux path formed by double-phase excitations.

The axial flux salient-pole machine operates in the same way as in the 6/4 radial flux salient pole machine. One of major differences between the two machines is related to the pattern of magnetic paths. In axial flux machines, magnetic paths is located between horizontal planes because magnetic energy conversion occurs in axial airgap between axial stator poles and axial rotor poles. The axial magnetic paths are distributed in a 3D space because magnetic fluxes tend to travel along those paths that offer minimal magnetic reluctances. This is due to the variation in magnetic core material density along the axial direction. In radial flux machines, the field distributions in radial cross-section planes stack along the axial direction. Notably, the distinction

mentioned here does not suggest a disadvantage for axial flux machines. The axial flux machines generally offer large axial pole surfaces which could vastly reduce the magnetic reluctances at aligned position, thereby boosting the torque generation capacity. In addition, the volume of the machine could be minimized due to the absence of the radial flux. There are many variants of axial flux PM machines and SRMs. The axial flux machines are inherently suitable for in-wheel drive applications. Due to their superior compactness and high torque density, some of them could be used for unmanned aerial vehicles (UAVs) or drones. Depending on the requirements of the targeted applications, either radial flux machines or axial flux machines could offer a suitable solution. On the contrary, as mentioned in the introduction, both topologies have partial conductors placed outside of the useful overlapped area between the rotor and stator. Those conductors are called end-windings which yield leaking magnetic fields and additional thermal stress. Furthermore, a part of the machine volume has to be used to house these end-windings as shown in Figure 2.11. Over the past decades, industries offered a few solutions to remedy the end-winding issue such as cast copper conductors and PCB windings to minimize the volume of end windings. Considering the additional cost and complexity of those winding designs those end-windings are still treated as negative factors in the machine design. In the proposed structure, the end-windings issue could be solved using a novel arrangement.

End windings of axial flux machine



End windings of radial flux machine



Note: the pictures are copied from the Google image

Figure 2.11: Images of end windings of radial flux machines and axial flux machines [29].

2.3 The proposed 3D flux structure

In any rotary machine, there are three surfaces, two axial surfaces and one cylindrical surface. A radial flux machine generally has a stack length greater than its pole pitch while an axial flux machine generally has a larger OD in the rotor when compared to its axial length. Usually a machine is built either with radial flux structure or an axial flux structure depending on the defined space. In EV and drone applications, the available volume for electric motors is normally limited. Especially, in case of in-wheel drive, the OD of the machine could be equal or slightly greater than the stack length. (2.3.1) presents the ratio of axial surfaces to the radial surface.

$$Surface\ ratio = \frac{S_{two\ axial\ surfaces}}{S_{radial\ surface}} = \frac{2 \times \pi \times \left(\frac{OD}{2}\right)^2}{\pi \times OD \times L_{stack}} = \frac{OD}{2L_{stack}} \quad (2.3.1)$$

If the surface ratio is close to 1, the machine may have similar axial surface and radial surface.

Thus, it is hard to decide whether axial surface or radial surface should be chosen. Note that the

ratio of 1 just presents a situation of a small difference in radial surface area and axial surface area. Considering the volume occupied by the end windings, the choice could be even harder. No matter which flux structure is adopted, there could be always a way to optimize the design. Clearly, it is unlikely to optimize all possible options for a given machine space and have them fabricated such that a final answer for that given space is known. Consequently, a fundamental question arises as what if both radial flux structure and axial flux structure could coexist in one machine? If the machine core could be properly energized, the machine space will be greatly utilized. The torque capacity could be boosted by both radial flux structure and axial flux structure. To further utilize the machine space, the end winding should be minimized as claimed in the previous section. The question is how to arrange all the above requirements and simultaneously realize them. It is necessary to review the two approaches in building the radial flux structure and the axial flux structure. A possible thought would be to directly install axial and radial windings on an exterior stator. With this small modification, the design could be quickly populated by conventional methodologies. To provide geometrical insights on the discussion, Figure 2.12 shows the exterior stator installed with radial and axial windings. The part corresponding to end windings are encircled in Figure 2.12. The volume of end windings is not reduced but increased by a factor of 2. This contradicts with the requirements. The winding installation will be complex because the radial windings and axial windings share common area. Moreover, the axial windings step in the way of the shaft. To fabricate this structure, one has to make tradeoff between the torque capacity and shaft diameter which also raises the concern of mechanical integrity. Therefore, the option of exterior stator with 3D flux structure is not quite practical and as such it is abandoned at the early stage of the study.

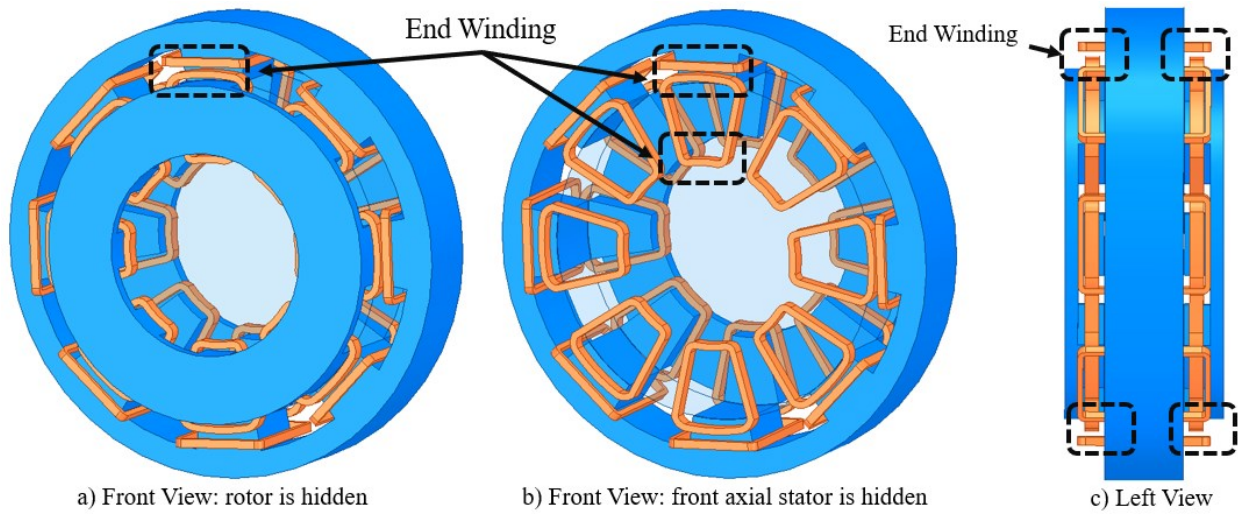


Figure 2.12: Structure with interior rotor.

The second option is to build radial flux structure and axial flux structure using an interior stator as shown in Figure 2.13. The axial flux links axial rotor poles and axial stator poles while the radial flux links the radial stator poles and radial axial poles. The reasonable way to energize the machine core and to form the 3D magnetic field is to use toroidal windings. As shown in Figure 2.13, toroidal windings installed on flux tubes could generate magnetic flux that circulates in the stator core. Basically, the stator core is not quite different to that of a regular inductor core if no specific treatment is applied. To regulate the direction of magnetic fluxes and to channel them through axial stator pole surfaces and radial pole surfaces, the additional magnetic fluxes with counter circulating direction from the adjacent toroidal windings must exist. If magnetic fluxes with the identical electromagnetic poles flow towards each other in stator poles, they will have to find alternate paths to link the respective opposite magnetic poles. In this case, the fluxes have to leave the stator pole, and travel through the adjacent airgaps, rotor poles and finally return to the corresponding stator poles. Most parts of the toroidal windings are placed in the radial flux structure and axial flux structure. Only the partial volume of toroidal windings encircled in

Figure 2.13 can be viewed as an unproductive end windings. In other words, the volume of end windings of the proposed interior stator is minimized. Notably, the torque of the exterior rotor is typically transferred from the exterior rotor frame such that its shaft mainly serves as the mechanical support.

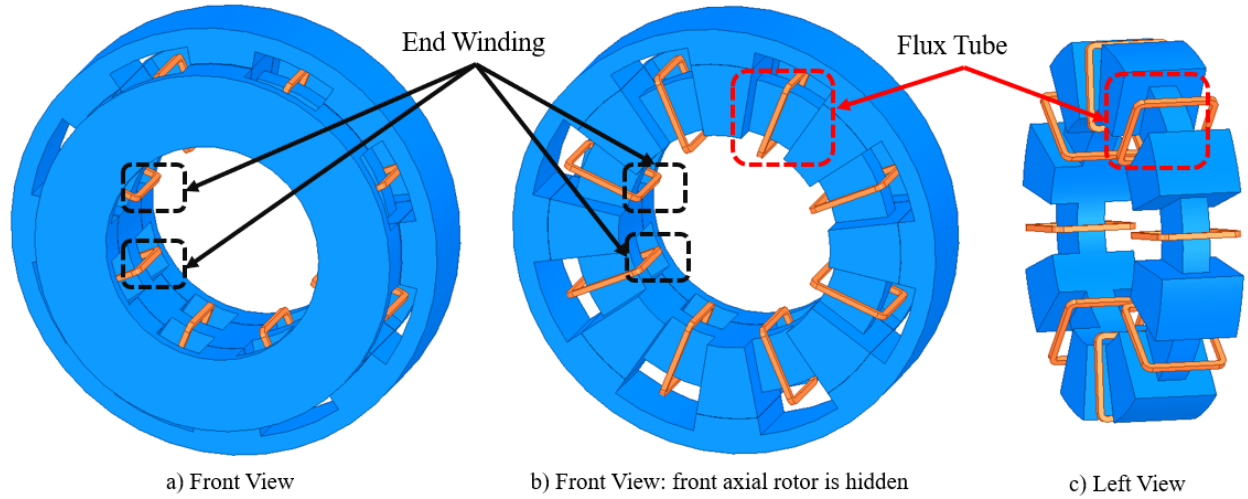


Figure 2.13: Structure with interior stator.

The inner space can be greatly used for housing the stator supports and end windings. The end windings would not step in the way of rotor. The combination of interior stator and exterior rotor is the suitable option for the proposed structure. In addition, an exterior radial rotor could offer a large rotor radius compared to the inner rotor structure shown in Figure 2.12. The rotor radius of inner rotor is known to be limited by many factors. Per the equation of Maxwell Stress Tensor (1.2), a larger radial rotor radius could be helpful to develop a higher torque. Figure 2.14 provides cross section view and side view of axial stator pole and axial rotor pole. In the side view of Figure 2.14, the magnetic flux lines perpendicular to both axial stator pole surface and axial rotor pole surface contribute to reluctance torque generation.

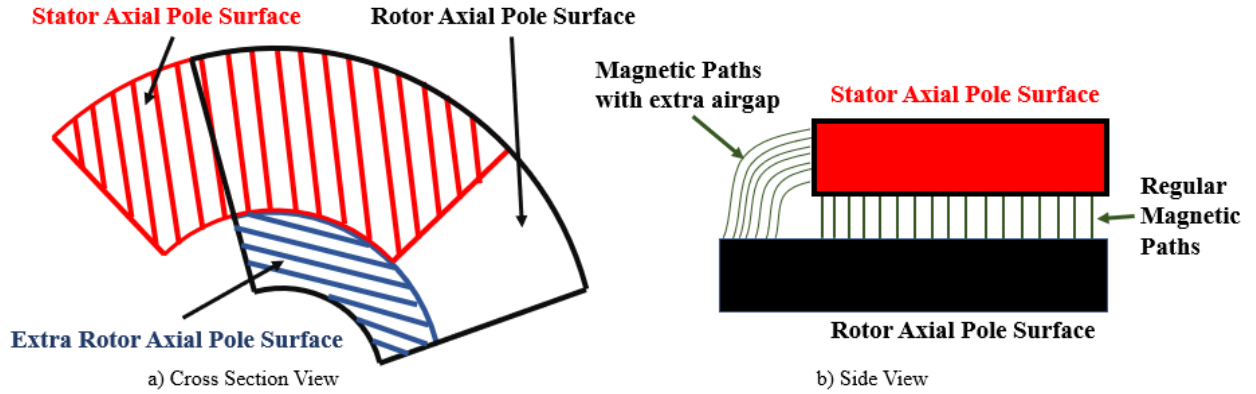


Figure 2.14: The views of extra axial rotor pole surface.

The extra axial rotor surfaces are not necessary since the linking magnetic fluxes have to travel through additional airgaps. Consequently, the flux density will be weakened. The magnetic core at the smaller radiuses is more prone to saturation at early stages of alignment. As a quick deduction, the magnetic paths at smaller radius may not generate significant reluctance torque. It is not quite worthy to pay much attention to those regions such that the extra axial rotor pole surface is removed to simplify the design. The scope of this study is refined to boost the torque capacity of the proposed 3D flux exterior rotor structure. The study is an iterative learning curve where multiple revisions have been carried out and multiple machine parameters beneficial to boost torque capacity will be discussed as well. In the next subsection, the first version of proposed structure with double-salient pole structure is developed where it represents the closest transformation from the conventional topologies.

2.4 First version: a double-salient pole 3D flux SRM

At the beginning of the design process, the machine space is constrained by a volume of 2.5 Liters. The 2.5 Liters comes from an early-stage estimation on the overall available space for mounting the motor. This thesis does propose the detailed configurations for a 2.5-Liter space. But it mainly introduces the high-level structure and the design method. The tasks of machine

design normally include: 1) develop proper phase inductance profiles 2) properly saturate the core 3) take advantages of saturation point of the materials 4) tradeoff among all requirements. As a rule of thumb, it is desired to fill in a space with a higher number of stator poles and rotor poles to shorten the span of magnetic flux paths and increase the phase flux linkage at aligned positions. This is beneficial to make a higher output torque in a low-speed machine. On the other hand, it is also required to have sufficient magnetomotive force from phase windings to ensure the strength of the magnetic field. The sufficient magnetomotive force raises requirements on magnitudes of excitation and the number of turns in the windings. In practice, the filling factor varies from 30% to 50% according concerning installation and cooling. This results in a minimal requirement of stator slot area which can introduce constraints for the highest number of stator poles and rotor poles for a given set of dimensions. As it is mentioned above, the design process is similar to a mesh network at high level. The design iterations could start from arbitrary initial design that emerges from requirements. In the following study, the filling factor is fixed around 50%. All simulations run with a fixed current density of $5 A_{rms}/mm^2$ which corresponds to an air-cooled winding. Under those high-level constraints, the best configuration offering the maximum torque is presented. Multiple details and considerations in tradeoff are discussed.

2.4.1 The pole configuration selection and winding configuration

Interior stator and toroidal windings are mandatory features of the proposed structure. The next task is to choose pole configurations. It is found that a valid 3D flux machine must simultaneously possess a feasible pole configuration and a feasible winding configuration. Conventional structures with exterior stator and concentrate windings have more freedom to

choose pole configurations and winding configurations. In this dissertation, only valid 3D flux designs are reviewed. The inappropriate pole configurations and their underlying reasons are not addressed. 16/12 model and 12/8 model are selected to test the capacity of the proposed structure. 16/12 SRM is a four-phase machine and 12/8 is a three-phase machine. Depending on winding configurations, toroidal windings on both sides of a stator pole should be simultaneously energized to form proper magnetic paths. For some configurations, if only one side is energized, the resulting magnetic flux will circulate in the stator core and turn the stator core into an equivalent inductor as shown in Figure 2.15.

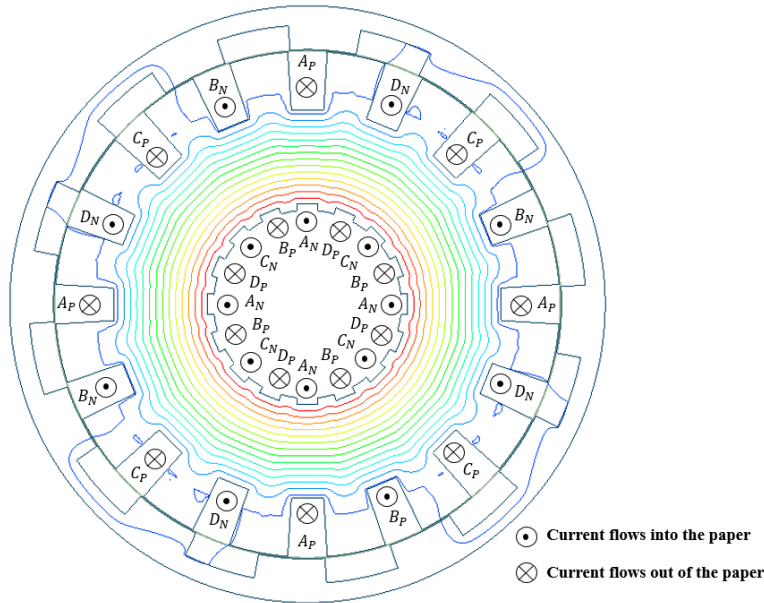


Figure 2.15: Circulating magnetic flux created by phase A excitation.

The circulating magnetic flux is prohibited in any case because it only yields thermal stress and is useless for torque harvesting. To properly operate the 16/12 model, two active and adjacent phase windings are required to form an “equivalent phase” [30]. At different time slots, the equivalent phase consists of one group of A and D, A and B, B and C, or C and D. The magnetic field distribution emerging from an equivalent phase of a 16/12 SRM is shown in Figure 2.16.

The major magnetic paths are highlighted. Some of them contribute to positive torque generation while some of them may partially contribute to negative torque depending on the rotor position.

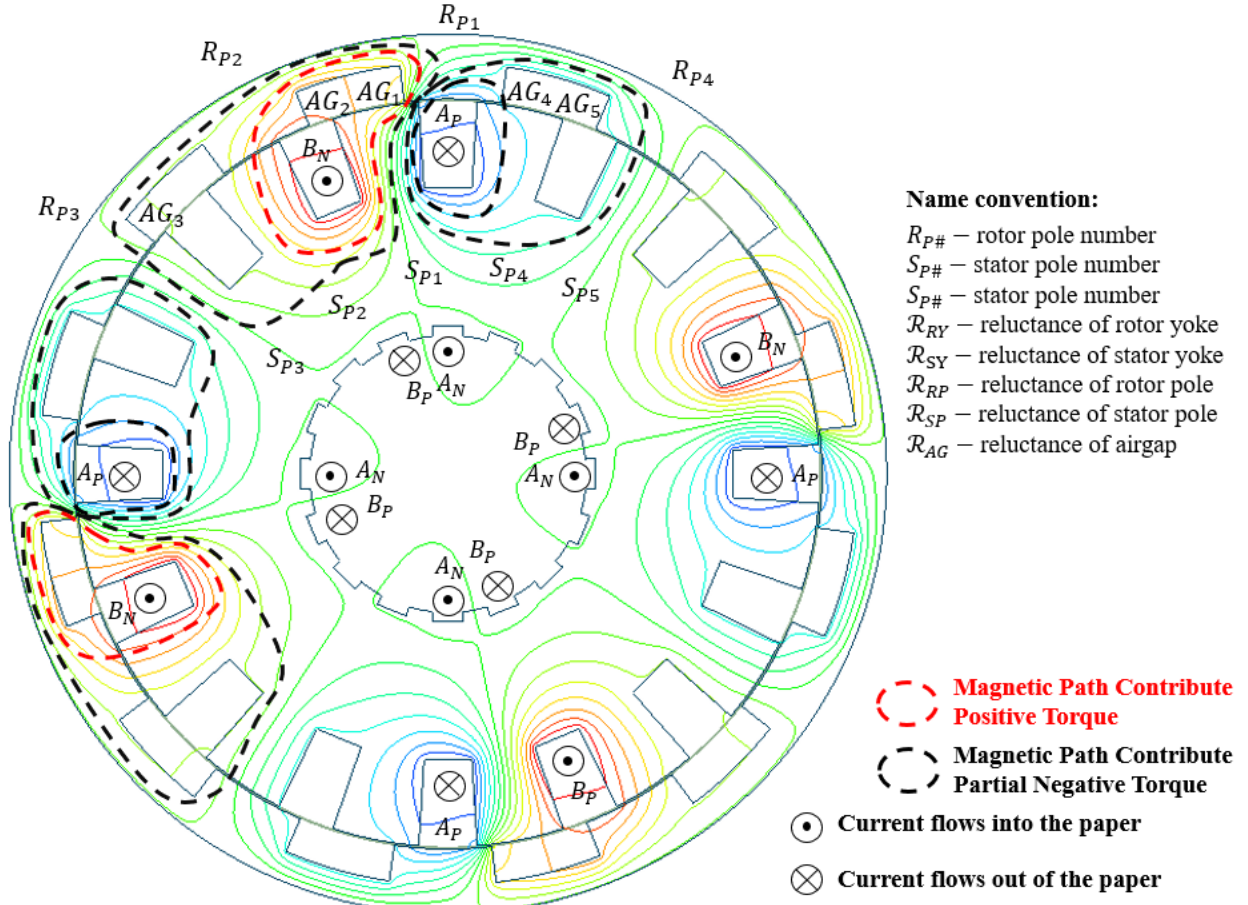


Figure 2.16 :The magnetic flux paths created by the “equivalent phase” [30].

The machine is a symmetrical four-phase machine. The pattern of magnetic field distribution repeats every 90° . The dominating magnetic paths of the half model are highlighted. The magnetic paths that yield positive torque are encircled by red dashed loop. The black dashed loops encircle magnetic paths that yield negative torque or may partially yield negative torque depending on the rotor position. It is obvious that the magnetic field is not satisfied since useful magnetic paths do not dominate the field. To characterize the magnetic paths, an equivalent magnetic circuit is derived and shown in Figure 2.17. The components in magnetic paths

yielding positive torque are labeled by red fonts in Figure 2.17 while the components in magnetic paths yielding negative torque are labeled by black fonts. As shown in Figure 2.16, the different magnetic paths may link the same stator poles and rotor poles of the machine core. To differentiate between the various reluctance terms of the magnetic paths at the same locations, they are denoted with the same subscript but with apostrophes such as \mathcal{R}_{RP1-BN} and \mathcal{R}'_{RP1-BN} where the subscript of each reluctance term explains the corresponding location. For example, the reluctance term of the rotor yoke between rotor pole #1 (R_{P1}) and rotor pole #2 (R_{P2}) is denoted as $\mathcal{R}_{RP1-RP2}$. Note that the reluctance terms at the same location are internally coupled. For instance, \mathcal{R}_{RP1-BN} , \mathcal{R}'_{RP1-BN} , \mathcal{R}_{RP1-AP} , and \mathcal{R}'_{RP1-AP} will be faced with the cross-saturation issue. They have independent impacts on different magnetic paths such that they are drawn separately in Figure 2.17 for clarity. It is obvious that $\frac{3}{4}$ magnetic paths counteract the positive torque generation, which is inappropriate. This situation could be mitigated by energizing an additional phase to form better magnetic field as shown in Figure 2.18 where phase A, B, and C are simultaneously activated. The portion of magnetic paths contributing to positive torque are enlarged. Partial magnetic flux paths are not highlighted because they disappear along the rotation, (i.e. the flux lines linking rotor pole #2, rotor pole #4, stator pole #4, and stator pole #2). The reluctance of this path increases along the rotor movement while the reluctance of magnetic paths linking winding C_p and winding A_p reduces in the meantime. Given the nature of the magnetic flux, it will stop flowing through the stator pole #4. This could be proven by Figure 2.19 which presents the magnetic field of the machine with a 3.3° forward rotation. It is worthy to note that the magnitude of excitation of the middle phase is needed to double in order to

prevent the magnetic flux from winding A_p directly linking magnetic flux from winding C_p . In other words, this is to avoid forming circulating flux.

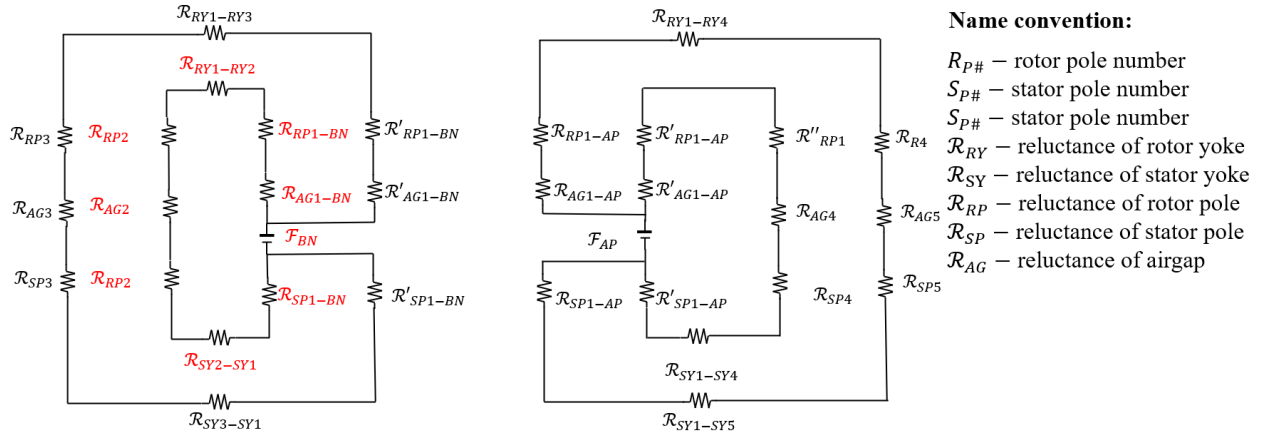


Figure 2.17: The equivalent magnetic circuit of $\frac{1}{4}$ model.

Figure 2.20 illustrates the equivalent circuit of $\frac{1}{4}$ model. It presents the magnetic paths from the vantage point of stator pole #1 and stator pole #2 which are energized by windings of A_p , B_N , and C_p . The partial magnetic paths links energized stator poles and rotor poles 90° ahead and behind. So, the magnetic circuit shown in Figure 2.20 also includes the magnetic paths linking S_{P5} and S_{P8} . The pattern of magnetic field still repeats every 90° . Compared to Figure 2.17, magnetic flux paths yielding positive torque dominate the magnetic field under three phase excitations. Thus, the correct winding configuration and excitation pattern for 16/12 double-salient pole 3D flux SRM is found. In every electrical cycle, a phase excitation profile has a duration which is doubled. This duration will be taken into account for the final current density.

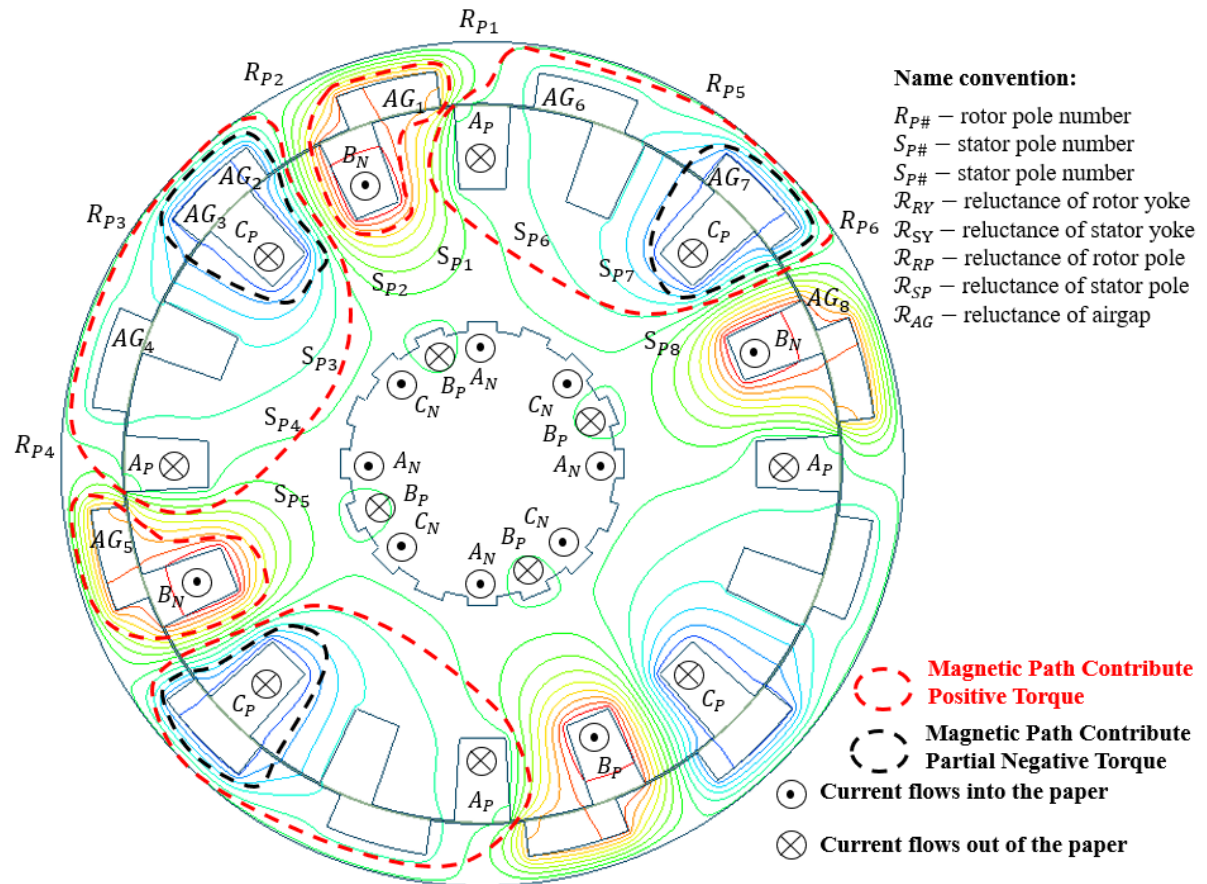


Figure 2.18: The magnetic flux paths created by three-phase excitation.

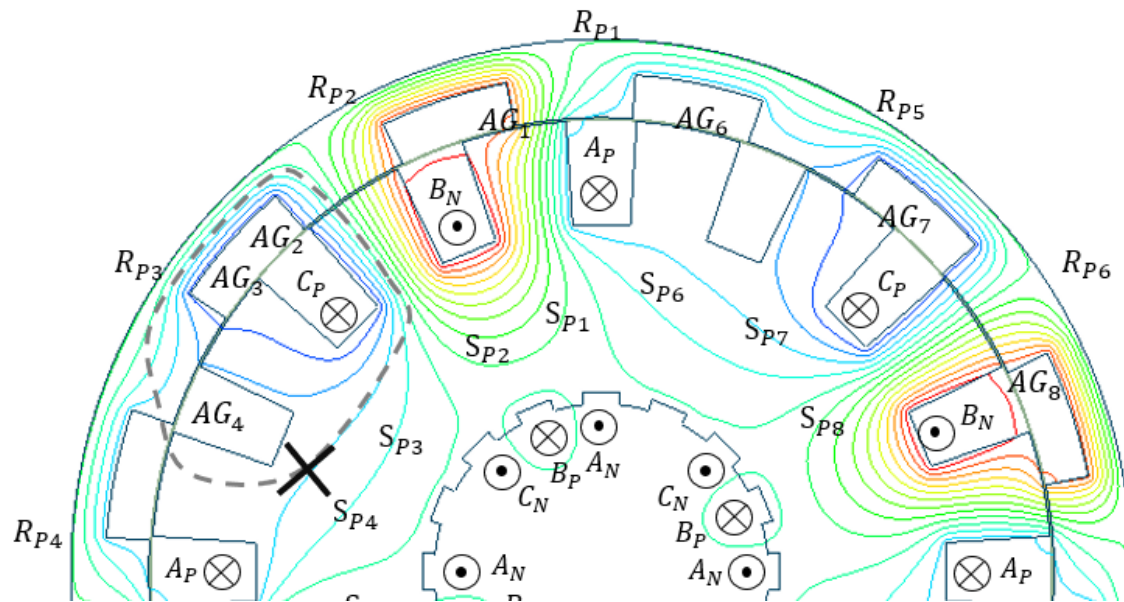


Figure 2.19: The magnetic field of 16/12 machine with 3.3° forward rotation.

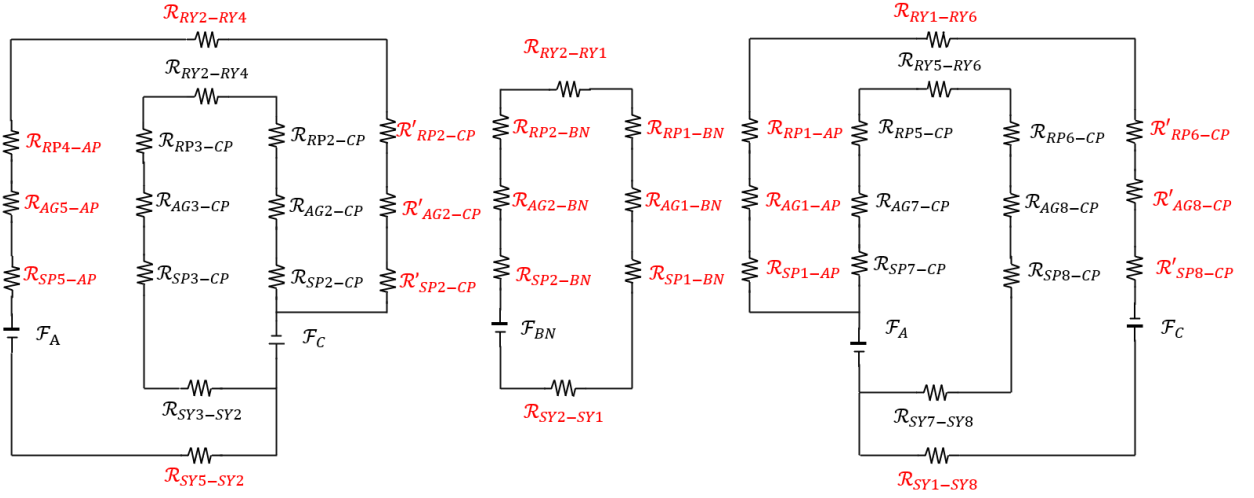


Figure 2.20: The equivalent magnetic circuit of $\frac{1}{4}$ model.

2.4.2 The 3D magnetic flux paths

The magnetic field of a 12/8 3D flux SRM could be tailored by the same approach as explained for the above 16/12 machine. The winding configurations of the 12/8 model is not discussed here. Before final selection of the best pole configuration within 2.5 Liters, it is worthy to observe the 3D magnetic flux distribution of the proposed structure and check for the necessary details. Although the pole configuration could be something else rather than 16/12 or 12/8 while the behavior of magnetic flux distribution in 3D space is similar. Therefore, the illustration of 3D magnetic flux field follows the same pattern as in the 16/12 model. The 3D flux vectors of 16/12 machine under three phase excitations are shown in Figure 2.21 and Figure 2.22. Patterns of magnetic field distribution in axial plane and radial plane are expectedly identical. Once there exist magnetic paths linking the certain energized radial stator poles and radial rotor poles, there will exist magnetic flux path linking the respective axial stator poles and axial rotor poles at the exact same positions. In the proposed structure, magnetic fluxes seemingly do not transverse among radial stator poles, radial rotor poles, axial stator poles, and axial rotor poles. The radial

magnetic paths refer to the loops linking radial stator pole surface, radial rotor poles, and flux tube. The axial magnetic paths are represented by the loops linking axial stator pole surfaces, axial rotor poles, and flux tube. By definition, it is not possible to have radial magnetic fluxes travel through axial stator poles and axial rotor poles. Thus, the 3D magnetic field can be viewed as a combination of separated radial magnetic field and axial magnetic fields, even though the cross-saturation could be found in the stator core (i.e. flux tube). Due to potential cross saturation in stator poles and flux tube, the best machine design does not necessarily mean to merge from the best radial flux structure and the best axial flux structure. The best machine design is the one that reaches a balanced point at which radial flux structure and axial flux structure are properly energized to obtain the maximum output torque. Such balancing must consider many machine parameters and is a nonlinear optimization process. The Genetic Algorithm (GA) global optimization discussed in Chapter 4 is used for this purpose.

To obtain a better understanding, the radial magnetic field and axial magnetic field are presented separately in Figure 2.21 and Figure 2.22 respectively. There are still too many flux vectors which make the plots difficult to read. To further improve the views, the windings are hidden in the figures and the model is sectionalized by the center radial clipping plane. Figure 2.21 presents the radial magnetic field in the $\frac{1}{2}$ model. The machine has a symmetrical structure such that the magnetic fields on both sides of the center clipping plane will be symmetric. The blue vectors in Figure 2.21 are flux density vectors. The arrows illustrate the flux direction. If read along the arrow directions, one can roughly figure out the radial magnetic paths and axial magnetic paths. The magnetic paths drawn by vectors are presented as red dashed contours and

black contours where the red contours denote the loops yielding positive torque and black contours denote the loops yielding negative torque.

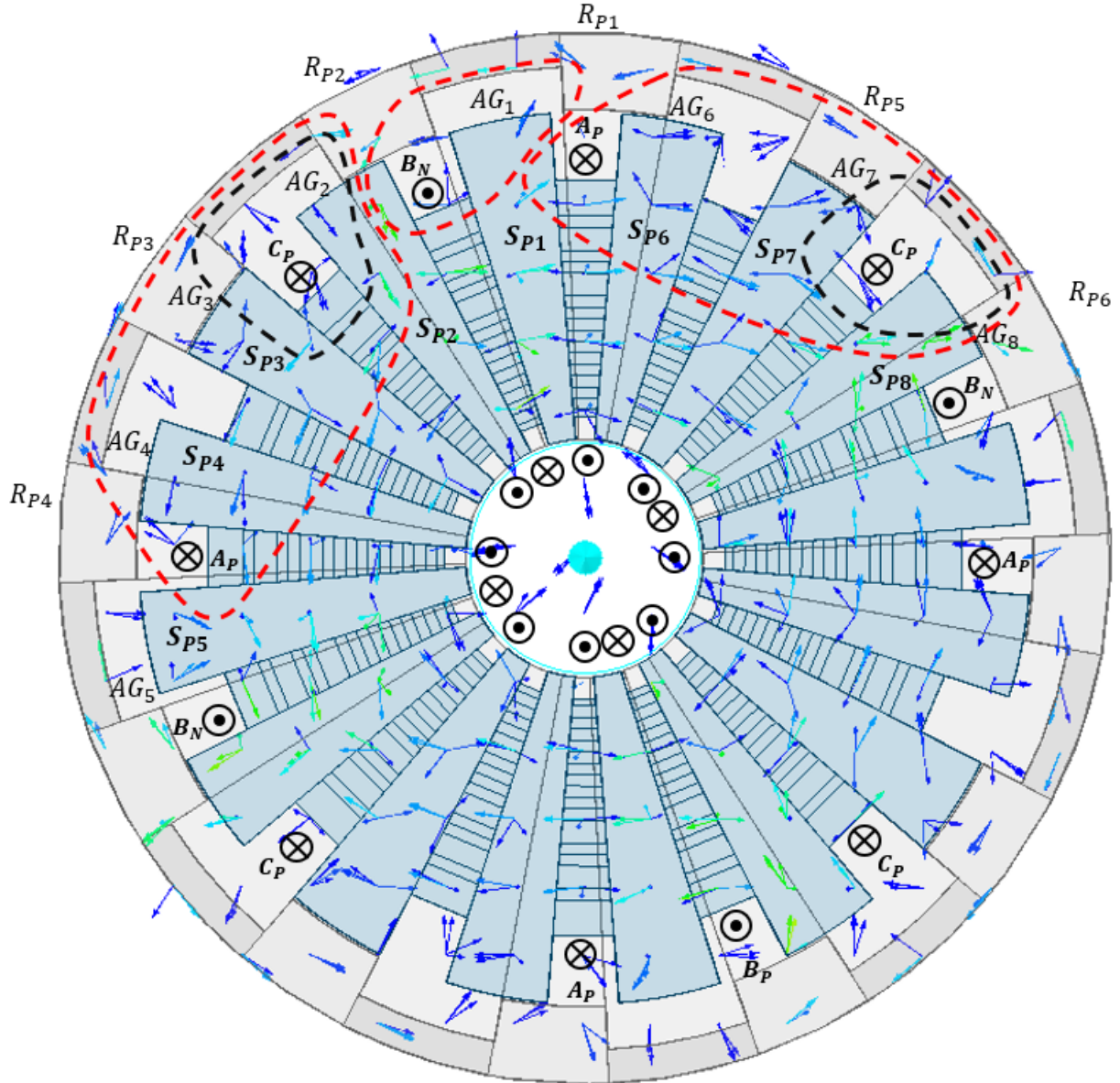


Figure 2.21: The radial magnetic field of the 16/12 3D flux SRM under three-phase excitation. The windings of A_P , B_N , and C_P are active. The current magnitude of winding B_N is doubled at this moment. The useful radial magnetic paths consist of three groups: group-one links stator pole S_{P1} , stator pole S_{P2} , rotor pole R_{P1} , and R_{P2} ; group-two links stator pole S_{P2} , stator pole

S_{p5} , rotor pole R_{p2} , and rotor pole R_{p4} ; group-three links stator pole S_{p1} , stator pole S_{p8} , rotor pole R_{p1} , and rotor pole S_{p6} . The rotor rotates counterclockwise (CCW). It is easy to imagine that the loop reluctances of these three groups of magnetic paths decreases along the direction of rotation. There are also mainly two groups of magnetic paths yielding negative torque: group-one links stator pole S_{p2} , stator pole S_{p3} , rotor pole R_{p2} , and rotor pole R_{p3} ; group-two links stator pole S_{p7} , stator pole S_{p8} , rotor pole R_{p5} , and rotor pole R_{p6} . The loop reluctances of these two groups increases with the rotation. The corresponding magnetic paths from the windings of A_p , B_N , and C_p in the remaining $\frac{3}{4}$ of the model will repeat the patterns shown in Figure 2.21 and are not presented here.

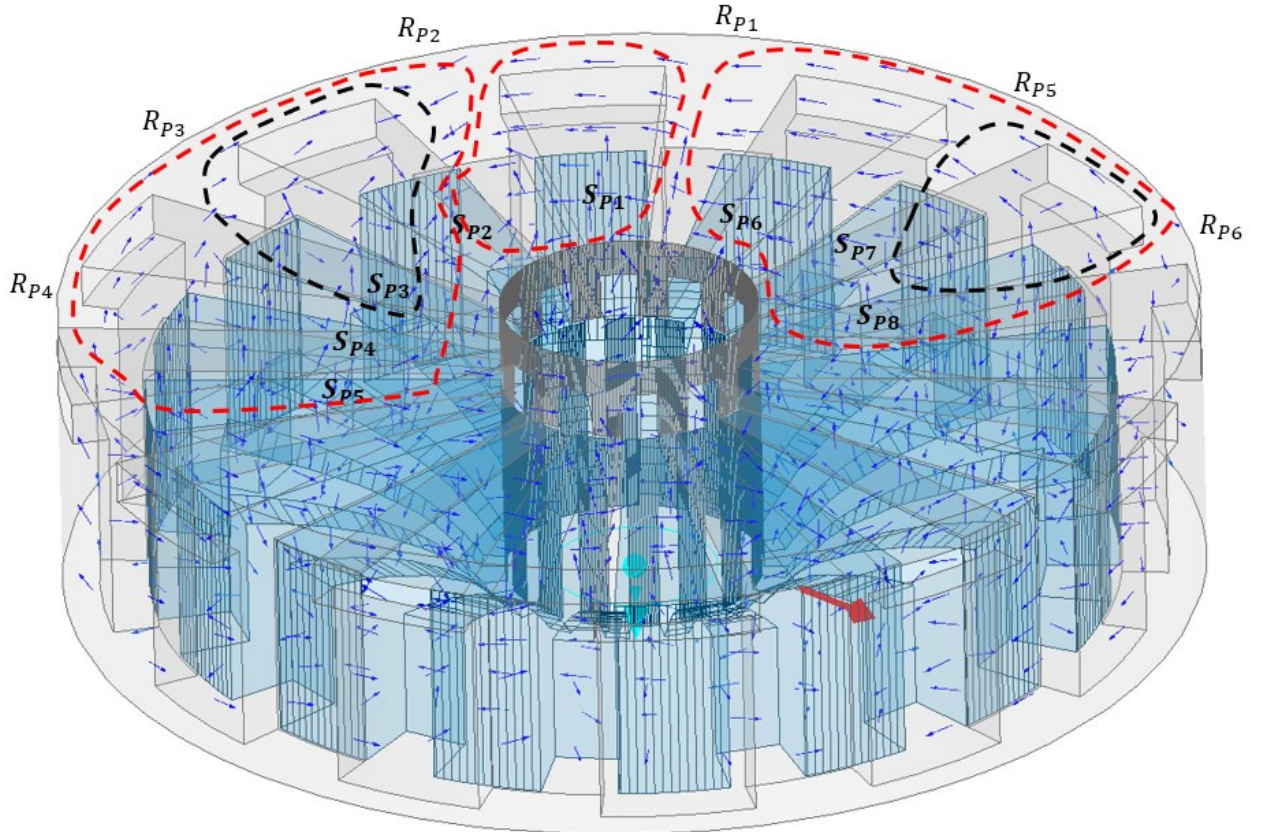


Figure 2.22: The axial magnetic field of the 16/12 3D flux SRM under three-phase excitation.

The axial magnetic fields are highlighted in the same manner as in Figure 2.22. The magnetic paths link the corresponding axial stator poles and axial rotor poles. The rotor positions of axial stator poles and axial rotor poles coincide with those of radial stator poles and radial rotor poles. Axial fluxes and radial fluxes have their independent paths; however, they will share the same flux tube. Different from conventional structures having windings directly installed on stator poles, the proposed structure has windings installed around the flux tube. The radial fluxes and axial fluxes stemmed from the windings travel through the internal flux tube and leave stator poles from the corresponding radial stator pole surfaces and axial stator pole surfaces as show in Figure 2.23 [30]. The model is sectionalized by an axial clipping plane to illustrate the magnetic flux vectors in the cross-section of the sectionalized flux tube. A simplified drawing demonstrates the flux vectors distribution in the flux tube and the respective stator poles and rotor poles. In the simplified drawing, the magnetic flux in the flux tube flows out of the paper. The fluxes travel through the radial airgap and axial airgap and enter the respective rotor poles. In the rotor parts, the magnetic fluxes flow into the paper. In fact, the magnet flux directions do not have to be identical with the drawing which only presents the idea of rotor fluxes traveling in the rotor back iron. The directions are changeable via the change in the actual excitation sequences and status of the alignment.

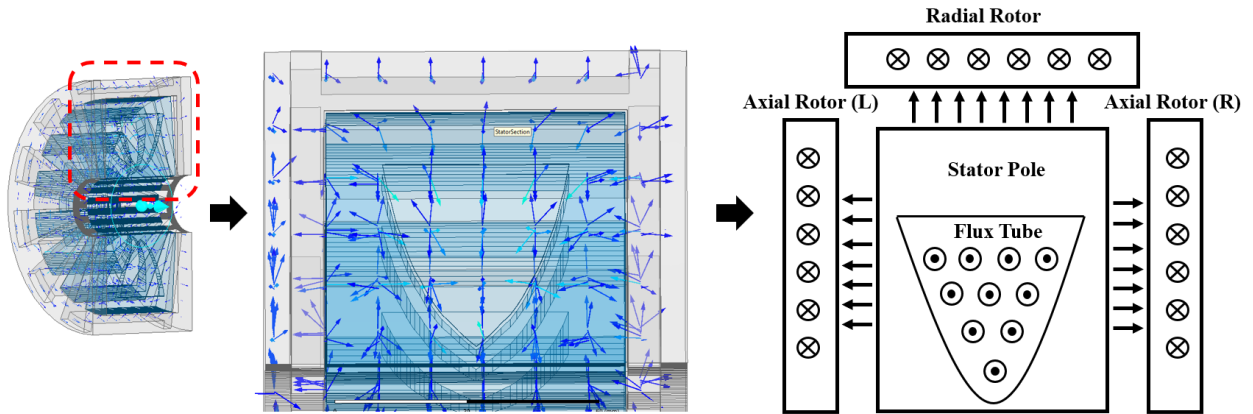


Figure 2.23: The magnetic field in the cross section of flux tube [30].

This is where the name “3D flux structure” makes sense. The ideal shape of the cross section of the flux tube has curvatures on both axial sides because it holds the minimal radial stator slots area for the windings. The minimal copper area of the stator slots along the radial direction and axial direction must be theoretically identical, after all the conductors in axial slots and radial slots belong to the same phase windings. One of the design challenges appears at this stage. The total cross section area of the inner stator is somehow under constraint. It is shared by the cross-section of flux tube and cross-section areas of radial and axial stator slots. Certainly, the larger cross-section of flux tube is always preferred to avoid bulk saturation. The bulk saturation in flux tube will significantly increase the “impedance” for MMF sources, which is not desired. On the other hand, minimal stator slot areas must be ensured to fill in sufficient number of turns of windings. The toroidal windings may be difficult to install compared to the regular windings and as such the larger stator slots are preferred in the process of fabrication. Thus, the balancing act between the volume of flux tube and total MMF forms one of crucial design steps in the 3D flux structure.

2.4.3 Fundamental dimensions

As multiple fundamental design principles have been discussed in the previous sections, it is necessary to physically map those principles to the actual machine design. The sectionalized stator poles and rotor poles with dimension labels are demonstrated in Figure 2.24 and Figure 2.25. In Figure 2.24, the stator section includes the radial pole, axial poles, and flux tube on both wings of the stator pole. In the case of the 3D flux double salient-pole structure, the shape of stator pole is simplified considering the common manufacturing practices. The top arc of stator pole is identical to the bottom arc of the stator pole. Even though the top arc and bottom arc could be different for optimization purposes, it may yield a complex alignment pattern between axial rotor poles and axial stator poles. In fact, the radial rotor and two axial rotors could be installed with a few degrees' deviation to modify the total torque profile by reducing torque pulsation. Alternatively, the interior stator could be designed with a certain skewing rate. However, the design rules are made to examine the principal advantages of the proposed structure such that the specified machine parameters and complex geometries which could potentially boost the torque capacity are not sought here. The radial stator pole arcs are identical to the axial stator pole arcs to synchronize alignments of the radial parts and axial parts. The axial parts and radial parts of the machine all yield the positive torque while the torque profiles from each portion could be different. It is worthy to clarify that the axial flux structure and radial flux structure must have the same pole configurations. Models with multiple pole configurations have been developed and tested to check the feasibilities. Before examining the machine structure for a specific pole configuration, the proper winding configuration is studied as well as for the polarities of toroidal windings. Subsequently the interior structure will be mainly

modified to seek proper stator slot area, stator OD, stator ID, stator pole arcs, etc. After all procedures are done, it is fair to conclude whether the pole configuration is suitable for the 2.5 Liters' of the available space. The double salient-pole structure is studied, compared to the segmented-rotor structure that will be introduced in Chapter 3. This is because the inherent design criteria of double salient-pole structure: rotor pole arcs must be smaller than stator slot allows for avoiding overlaps between stator poles and rotor poles at unaligned positions. As a result, the workload of trend study for each pole configuration is limited.

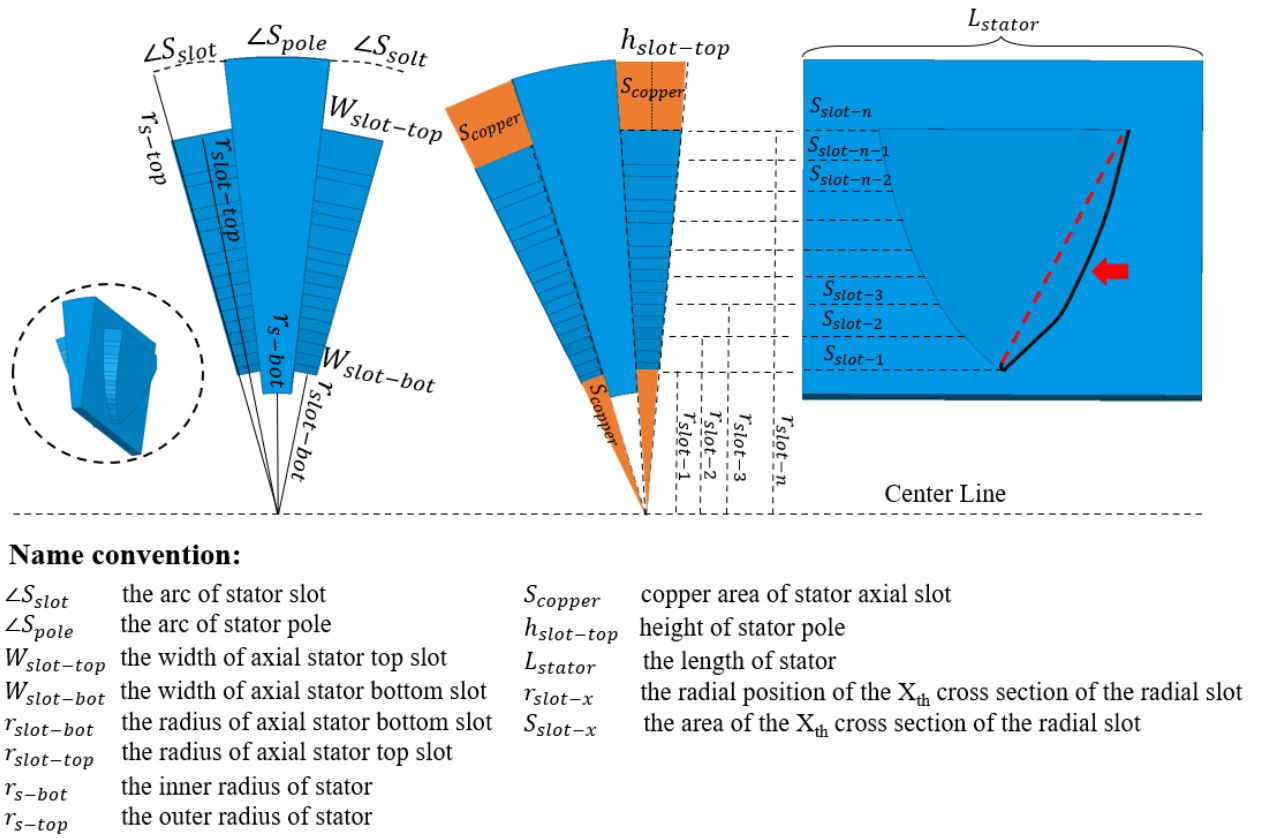


Figure 2.24: The sectionized stator pole with dimension labels.

Beside ensuring the radial stator slots and axial stator slots, the bottom regions must be sufficient to house the windings. The axial stator slots and bottom regions are filled with orange color in Figure 2.24. In practice, the $r_{slot-bot}$ could be enlarged a bit to increase the bottom slot area. The

radial stator slot along the radial direction is sectionized into a few segments. The cross-section area of each segment is denoted by S_{slot-n} where 'n' increases with the radial distance of the cross section. The curvature of the highlighted solid black curve of the cross-section of the flux tube is a result of computation which ensures S_{slot-n} ($n=1,2,3,4,\dots, p$) to be equal or greater than S_{copper} . The curve defines the borderlines of flux tube. The edge of flux tube must not extend over this line. In fact, curve can be pushed inward as shown in Figure 2.24 to make more space for toroidal windings and to make the manufacturing easier. The extreme case is to make the edges of the flux tube totally straight as shown by the red dashed line. On the other hand, pushing the edges inwards makes the flux tube prone to bulk saturation due to their reduced cross section area. At the early stages of the study, the primary objective is to seek the principal advantage of the proposed structure. The mechanical integrity and feasibility of the manufacturing are not investigated at this stage. To simplify the validation process, the flux tube of the targeted models is all built with curved edges which ensure the minimal cross-section areas for radial stator slots along the radial direction. Moreover, the maximum applicable stator slot area of an interior stator can be found. The thought process is straightforward: if the flux tube with curved edges shows bulk saturation, the stator slot area should be reduced. The stator pole pitch consists of the stator pole arc and stator slot opening. A higher number of stator poles means a smaller stator pole pitch, a smaller stator pole arc, and a smaller stator slot opening. It also means that a smaller number of turns in the windings could be placed in every stator slot. On the contrary, if the magnetic field can be properly tailored, the lengths of the partial magnetic paths reduces when the number of stator poles increase. Note that the shorter magnetic paths provide the smaller loop reluctance and the higher flux linkage. As a result, if the partial short

magnetic paths can yield dominating output torque, the interior stator with more stator poles could be helpful to boost the torque capacity. As discussed in previous sections, to obtain a higher flux linkage, a phase must provide sufficient MMF. Since the current density in this study has an upper limit of 5 Arms/mm^2 , a phase winding must have sufficient number of turns to obtain the sufficient MMF. The logical type of flow presented here is bidirectional. If an interior stator with a high number of stator poles cannot provide sufficient stator slot area, the number of turns of the installed windings will be limited. Since there is no sufficient MMF to take advantage of the shortened magnetic paths, the number of stator poles should be decreased. In Figure 2.25, the radial rotor section and axial rotor section are demonstrated separately. According to the above discussions, $R_{rr-pitch}$ and $R_{ar-pitch}$ are identical and so are the arcs, $\angle R_{rr-pole}$, $\angle R_{ar-pole}$, $\angle R_{rr-slot}$, and $\angle R_{ar-slot}$. The positive torque period of radial parts and axial parts coincide. The total length of the outer rotor is the summation of $L_{rr-stack}$ and two times of $L_{ar-stack}$. The length of radial part, $L_{rr-stack}$ is the summation of L_{stator} and two times of the axial airgap. Considering the fabrication and actual assembly, the inner radius of axial rotor, r_{ar-bot} could be adjusted by the OD to allow for fitting ball bearings. Since the region of axial rotor closed to shaft and bearing does not contribute significant torque, the inner radius does not have to be identical to the inner radius of axial stator pole. The radial yoke thickness and axial yoke thickness, $L_{rr-yoke}$ and $L_{ar-yoke}$, do not only determine the performance of the magnetic fields but also determine the mechanical integrity of the design. After all, the torque of three rotors transfers from one axial rotor to the externally coupled shaft. This put requirements on the exterior rotor structures in terms of stiffness and elongation. As a result, the thickness of rotor back iron is required to support the magnetic flux conduction and torque transmission. To

support torque transmission and avoid deformation, rotor back iron is generally thicker than what it is only for magnetic purposes. In Figure 2.26, the stator and rotor are sectionized to provide the clear insights about the alignment patterns of stator poles and rotor poles. The sectionized rotor has three parts, one radial piece and two axial pieces. Again, to provide a clear sight, the back side axial rotor is hidden. And the axial rotor model is set to be transparent such that the internal edges and surface could be easily observed. The axial rotor pole and the radial rotor pole align to their counterparts following the same pattern. At the aligned position, both rotor poles will fully overlap with the stator poles. Even though the machine has independent radial field and axial fields, the radial rotor and axial rotors can be merged into one piece. There are no transverse fluxes between radial part and axial part. The axial magnetic paths and radial magnetic paths only share the same flux tube and partial region of stator poles. By duplicating the stator pole and rotor poles along the axial centerline, the completed machine geometry could be seen. The exploded view of the completed 16/12 3D flux SRM is presented in Figure 2.27. In practice, the axial rotors and radial rotor are needed to be manufactured separately and be assembled by bolt screws where the installation bores are not drawn in the figure for simplicity. In addition, the extra thickness of the radial back iron is needed to house the installation bores. In this thesis, the axial airgap is set to be identical with the radial airgap to make the actual assembly easier. The axial airgap and radial airgap are both 0.4mm in this thesis. In fact, the airgaps could be shrunk by proper fabrication treatment. The radial airgap can be shrunk to 0.2mm which has been seen in a few commercial products. When shrinking the axial airgap, carefulness and sufficient simulations are needed since the axial electromagnetic forces are quite strong and can raise mechanical integrity concerns.

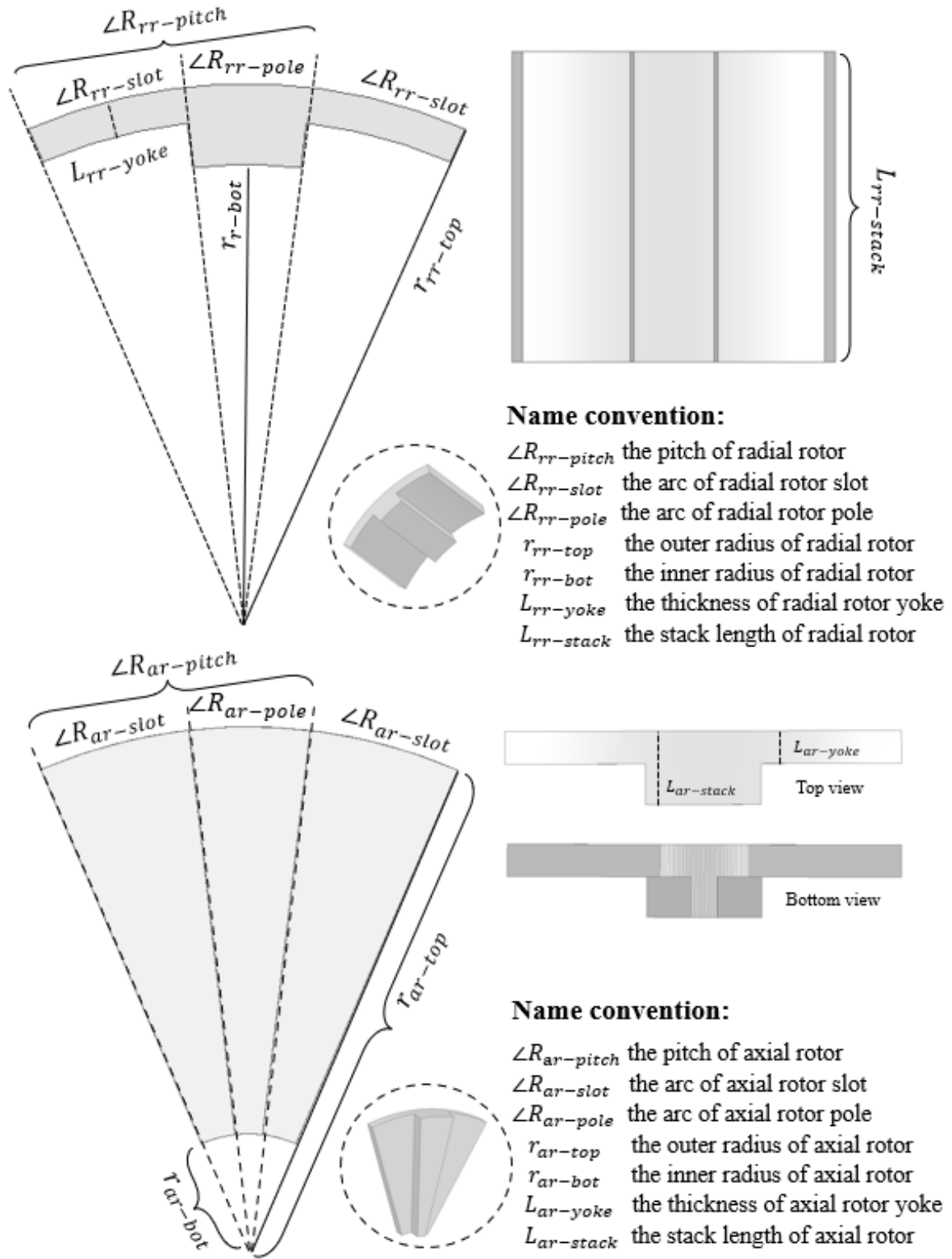


Figure 2.25: The sectionized rotor poles with dimension labels.

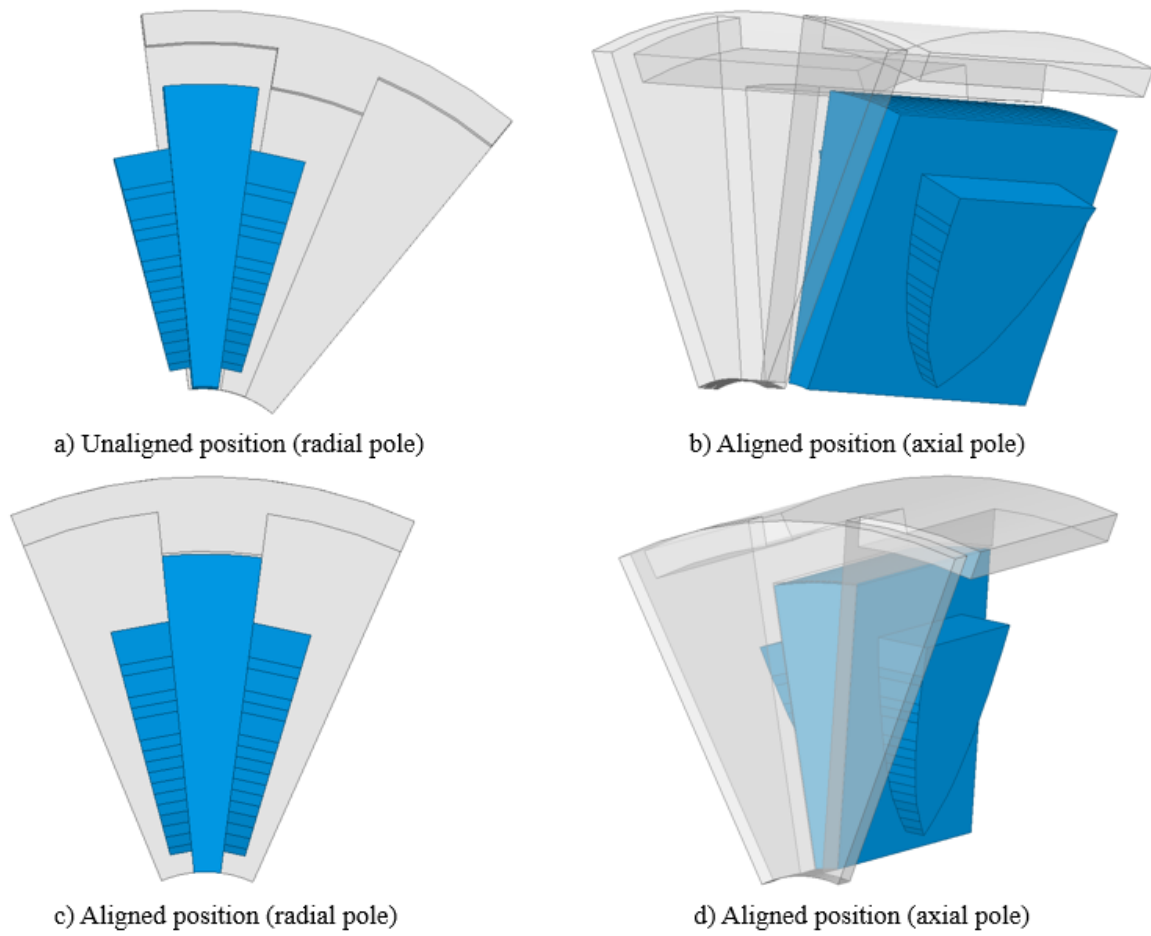


Figure 2.26: The alignment pattern of the stator and rotor.

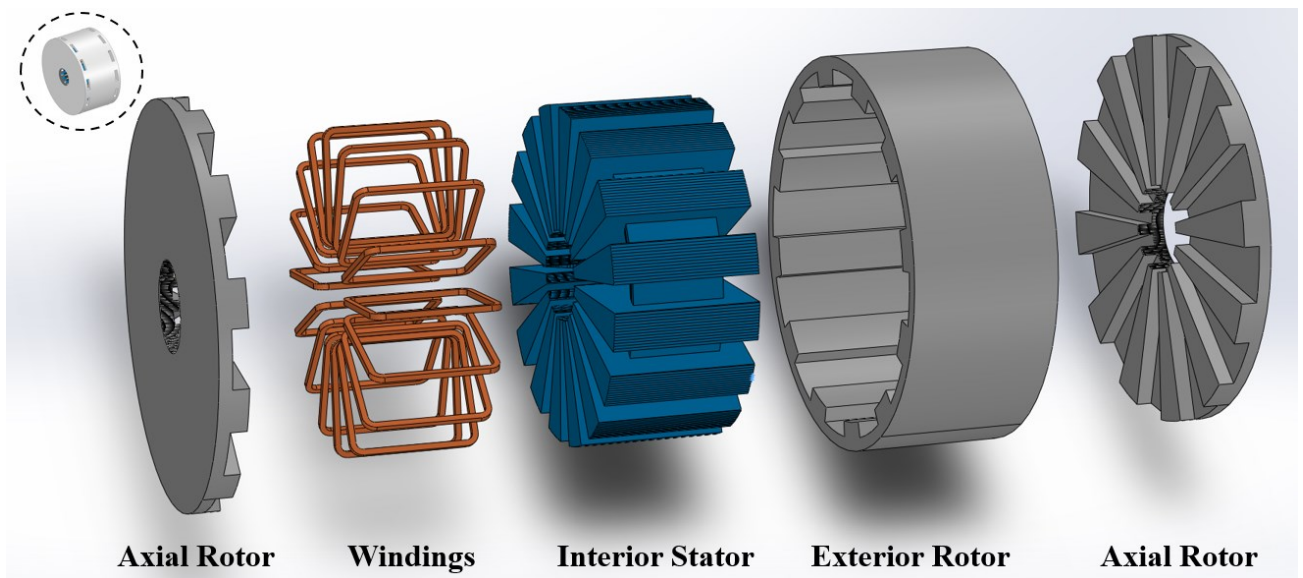


Figure 2.27: The exploded view of the 16/12 salient pole structure.

2.4.4 The optimal configuration

Multiple pole configurations and winding configurations have been tested under the space constraints around 2.5 Liters. One crucial objective is to draw balancing between strength of the field and the lengths of magnetic paths. The objective will be eventually narrowed down to simultaneously decide the pole configuration and number of turns in the windings. The concluding result of this study indicates that the torque capacity under rated condition could be less than that of the pole configuration in which there is a higher number of rotor poles than stator poles. In Figure 2.28, the 08/14 model are presented. The 08/14 model has a higher number of rotor poles than stator poles. Again, the magnetic field analysis is based on the 2D model since the 3D field will show the same pattern.

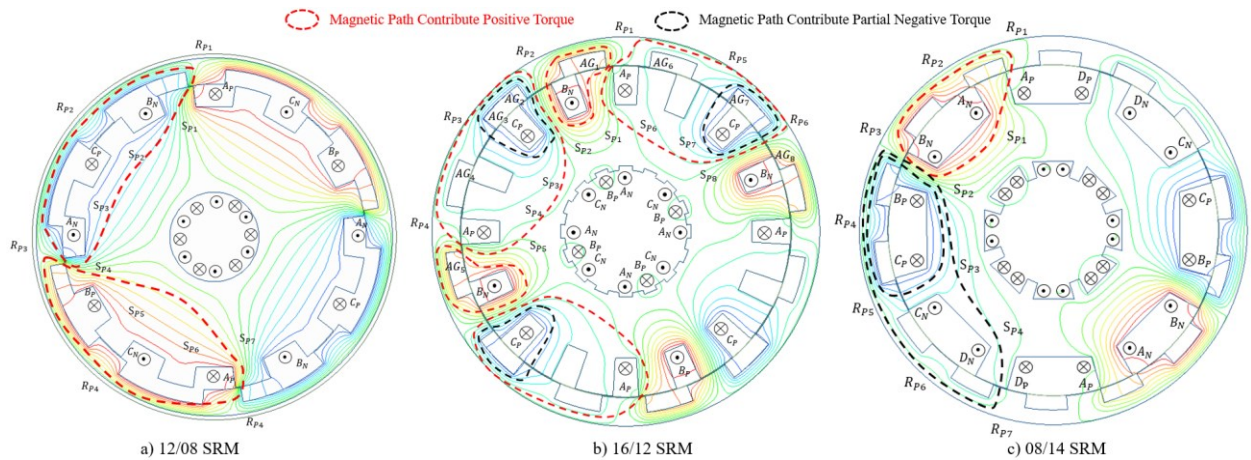


Figure 2.28: The radial magnetic field layout of three different pole configurations.

In general, pole configurations with a higher number of rotor poles offer the shorter magnetic flux paths which indicates the higher developed torque [21-22]. Even though, there are magnetic paths that potentially yield negative torque. In the pole configuration presented in Figure 2.28, the major magnetic paths distributed between two active stator poles. Since there are only 8 stator poles, the stator slot area is much larger than those of 16/12 and 12/08. More number of

turns in the windings can be installed in the stator slots such that the MMF per loop becomes considerably large while the length of the major magnetic paths offers a span of 45° . The magnitudes of magnetic flux are boosted as well. Thus, the output torque will be theoretically larger than 16/12 model and 12/08 model. Different to the 16/12 and 12/08 structures, the concentrated winding is adopted for 8/14 structure where phase windings are placed on both sides of the stator pole. To energize a stator pole, only one phase is required to be energized. The 8/14 model can provide the single-phase torque and stroke torque. To harvest stroke torque, two adjacent phases are required to be energized to form the shortest magnetic path. The machine structure is symmetrical. Stator poles belonging to one phase have a 180° spacing. The magnetic path from one phase has spans of 180° while the magnetic path formed by stroke excitations has a span of 45° . The stroke excitation refers to the necessary multiple-phase excitations with respect to rotor position to form a short flux path. The magnetic flux path of three models under stroke excitations are presented in Figure 2.28. In the 16/12 model, there are magnetic path having a span of 22.5° . However, this pole configuration is not suitable for the 2.5 Liter space. Even though the maximum number of turns in windings have been applied, there is not sufficient MMF to fully exploit the short magnetic path. Compared to 16/12 model, the 8/14 model is a good fit for the 2.5-Liter space where all conditions are fairly exploited. Besides short magnetic paths, there are long magnetic paths potentially yielding negative torque, which is an inherent drawback of the pole configuration of double-salient pole structure with a higher number of rotor poles [21]. However, the total torque is superior to that of 16/12 model and 12/8 model as demonstrated in Table 2.3. Table 2.3 summarizes the optimal structure under the same constraints of the total machine space, current density, and the filling factor. The OD and stack length of the

machine are 184mm and 96mm, respectively. The current densities of three models are kept at $5A_{rms}/mm^2$. In each model, the stator pole arc and rotor pole arc are set to be identical as it was explained in the previous sections. Compared to 16/12 model and 8/14 models, the 12/8 model does not have the adequate startup torque which is a major drawback. The advantage of 12/8 configuration, as shown in Figure 2.28, is the absence of magnetic flux paths potentially yielding negative torque. The stator pole arcs and rotor pole arcs of all models in Table 2.3 [30] have been optimized to exploit the best torque density. The magnetic core material is Hiperco 50 which has a saturation point between 2.2 Tesla and 2.4 Tesla. The slot area of each model can be enlarged as much as possible in view of the high saturation knee point. It is desired to evaluate the models under marginal saturation. However, marginal saturation may not be achieved in all models. The static torque profiles of the three models under the same current densities are simulated via commercial 3D FEA package Maxwell. The 16/12 model offers the minimal torque capacity. 12/8 model offers good average torque while it is not practical due to the absence of adequate startup torque. The 8/14 model offers the maximum average torque and as such it is considered as the first contender for 3D flux SRM. The torque ripple levels are not quite a concern at this stage of design. The geometries of the three models are shown in Figure 2.29 [30] where the axial rotors are hidden in order to demonstrate the interior stator. The geometry of the axial rotor could be seen in Figure 2.27. The magnetic flux density plots of the center cross section of the machines are also presented in Figure 2.29 [30].

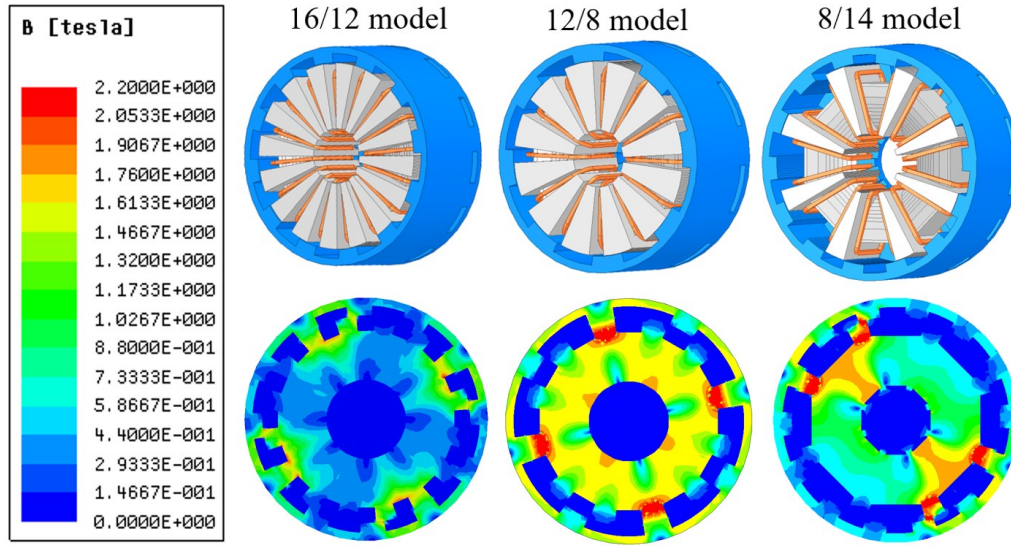


Figure 2.29: The geometric view of the simulated models [30].

Table 2.3: The Comparison Of Different Pole Configurations [30]

Machine Parameters	12/8 model	16/12 model	8/14 mode (Original)
Stator Pole Arc (°)	14	12	12
Stator Pole Pitch (°)	30	22.5	45
Rotor Slot Arc (°)	14	18	13.7143
Rotor Pole Arc (°)	36	12	12
Machine OD (mm)	184	184	184
Machine Length (mm)	96	96	96
Rotor Pole Depth (mm)	7.5	7.5	7
Rotor Back Iron (mm)	6	6	6.5
Stator Length (mm)	68	68	68.2
Stator Radius (mm)	78	78	78.2
Radial Airgap (mm)	0.4	0.4	0.4
Axial Airgap (mm)	0.4	0.4	0.4
Axial Slot Area (mm^2)	210	136	460
Radial Slot Area (mm^2)	210	136	460
Shaft Radius (mm)	20.8	20.8	25
Iron Material	Hiperco	Hiperco	Hiperco
Current Density (A/mm^2)	5	5	5
Turns Number	40	40	80
Phase Number	3	4	4
Stroke (°)	15	7.5	6.4286
Effective Torque Zone (°)	15	15	12.8571
Avg Storke Torque (N.m)	20.1	8.3	28.46

As mentioned before, the 16/12 model is not quite suitable for the 2.5-Liter space due to the insufficient number of turns in its windings. The flux density of the interior stator is weak. 12/8 model and 16/12 model show marginal saturation at stator pole bases. The actual flux densities of those regions are around 2.2 Tesla and 2.4 Tesla. For demonstration purposes, the upper limit

of the color map is set to 2.2 Tesla. The magnetic flux plot of the 8/14 model proves that major field concentration is located between the active adjacent stator poles. The flux densities of rotor back iron outside of the major magnetic path are lower than 0.7 Tesla. The 3D magnetic field under stroke excitations is presented in Figure 2.30. Notably, to have a clear view, the winding models are represented by current sheets whereas the active phases are represented by purple sheets. Following the arrows of magnetic flux density vectors, the dominating magnetic flux paths can be seen. The magnetic flux paths (red dashed loop) linking rotor pole #1, rotor pole #2, stator pole #1, and stator pole #2 are encircled by the red dashed loop which validates the discussion of Figure 2.28. The other two black dashed loops could potentially harvest negative torque. The magnetic flux paths on the other half of the model are not drawn since they will be mirror image of what has been shown in Figure 2.30. After theoretical advantages have been proven, the 8/14 3D model have been revised for manufacturing considerations. Especially, the inner diameter (ID) of the stator and axial rotors are enlarged to ensure sufficient space for housing windings, supports, and shaft. To simplify the manufacturing, the curvatures of the flux tube is removed such that the cross section of the new modified flux tube has a trapezoidal shape. The slot area is slightly enlarged to provide more space for windings. The changes are shown in Figure 2.31 [30]. The properties of the original 3D model and its revision are summarized in Table 2.4. To add a further practical insight in the comparison, the table also includes the experimental data of a commercially available 06/10 SRM V01 which is a 5-Liter 6/10 SRM. The commercial SRM is a radial flux machine and has an air-cooled interior rotor while it has a structure with a higher number of rotor poles than the stator pole. In addition, the commercial SRM has an airgap of 0.2mm which is half of the airgap in the proposed SRM. The small airgap

could greatly enhance the flux linkages of the SRM and boost the torque. This gives the commercial SRM a higher torque capacity. Even though the comparison may not be exactly fair since the proposed structure has three rotors while the commercial product just has one radial rotor, the value offered by the proposed structure could be noted. Merging more rotors in the machine space is the signature of the proposed structure.

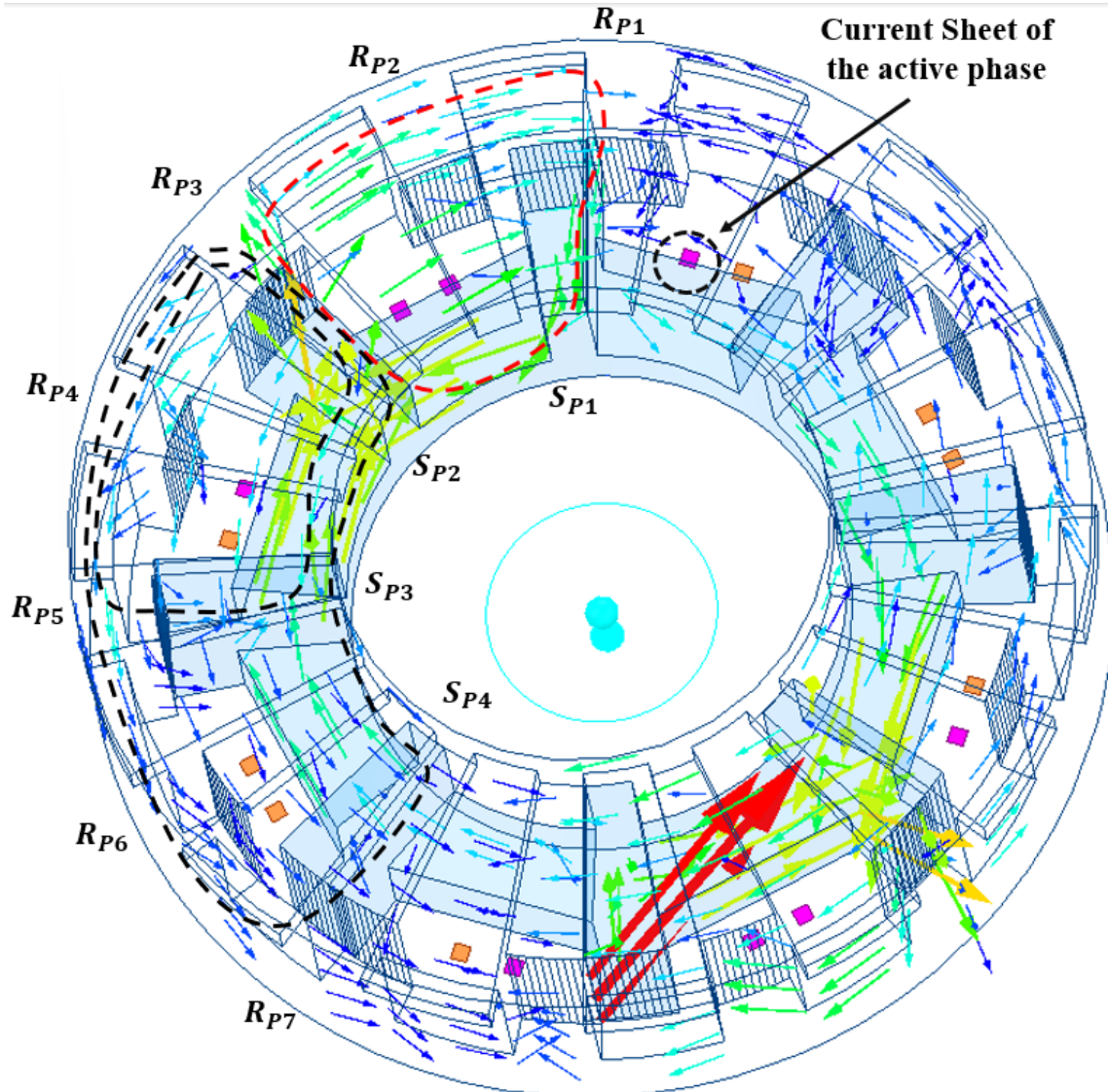


Figure 2.30: The 3D magnetic field in the 08/14 structure.

After geometrical simplifications, the 8/14 double salient-pole 3D flux SRM (2.5 Liters) has a torque density of 8.8Nm/Liter while the torque density of the commercial 6/10 SRM (5.69 Liters) is around 2.1 N.m/Liter. Generally, a conventional machine having a larger volume could offer a higher torque density since it has more space to house the windings and enlarge the volume of the flux tube. This phenomenon could be more exaggerated for the proposed structure since the magnetic cores are meant to fully exploit under rated conditions. This translates to developing the shortest magnetic paths and maximize the flux density. It must be noted that the commercial SRM uses M-19 for its magnetic core.

Table 2.4: Comparison Of 08/14 Models With the Commercial SRM

Items	08/14 (original)	08/14 (simplified)	06/10 (commercial)
Rotor Pole Arc (°)	12	10.6	16
Radial Rotor Inner Radius (mm)	78	78	49A
Radial Rotor Back Iron (mm)	7	7	N/A
Radial Rotor Length (mm)	69	69	89.6
Axial Rotor Length (mm)	13.5	13.5	N/A
Axial Rotor Back Iron (mm)	7	7	N/A
Axial Rotor Outer Radius (mm)	92	92	N/A
Axial Rotor Inner Radius (mm)	43	43	N/A
Stator Outer Radius (mm)	77.6	77.6	82.9
Stator Inner Radius (mm)	43	46	49.2
Stator Length (mm)	68	68	89.61
Stator Pole Arc (°)	12	10.6	12
Axial Slot Area (mm ²)	560	560	N/A
Filling Factor (%)	50	50	50%
Airgap (mm)	0.4	0.4	0.2
Phase Number	4	4	3
Turns Number	80	80	N/A
Phase Resistance (ohm)	0.25	0.25	0.4
Peak Phase Current (A)	50	50	10
Average Torque (N.m)	28.46	22.5	12
Overall Volume (Liters)	2.55	2.55	5.69
Torque Density (N.m/L)	11.16	9.4	2.108
Torque Ripple (%)	62.8%	94.8%	90%

If the space constraint for the proposed structure could be enlarged to 5 Liters, either the larger flux tube could be used, or the more stator poles and rotor poles could have been used, thereby increasing overall flux linkage. The torque density will be certainly higher than 8.8 N.m/Liter. Given the trend study of the proposed structure, there is a balance to be achieved between

machine space, saturation point of the soft ferromagnetic materials, and the pole configuration. This may be able to explain why 16/12 model is not a good choice for the 2.5-Liter space. With a larger dimension, the 8/14 model may be abandoned as well. If different magnetic materials are adopted, such as M15 or M19, which offer saturation points around 1.3 Tesla, 8/14 model may not be superior to 16/12 model and 12/8 model. This is because over saturation or insufficient magnetization may occur.

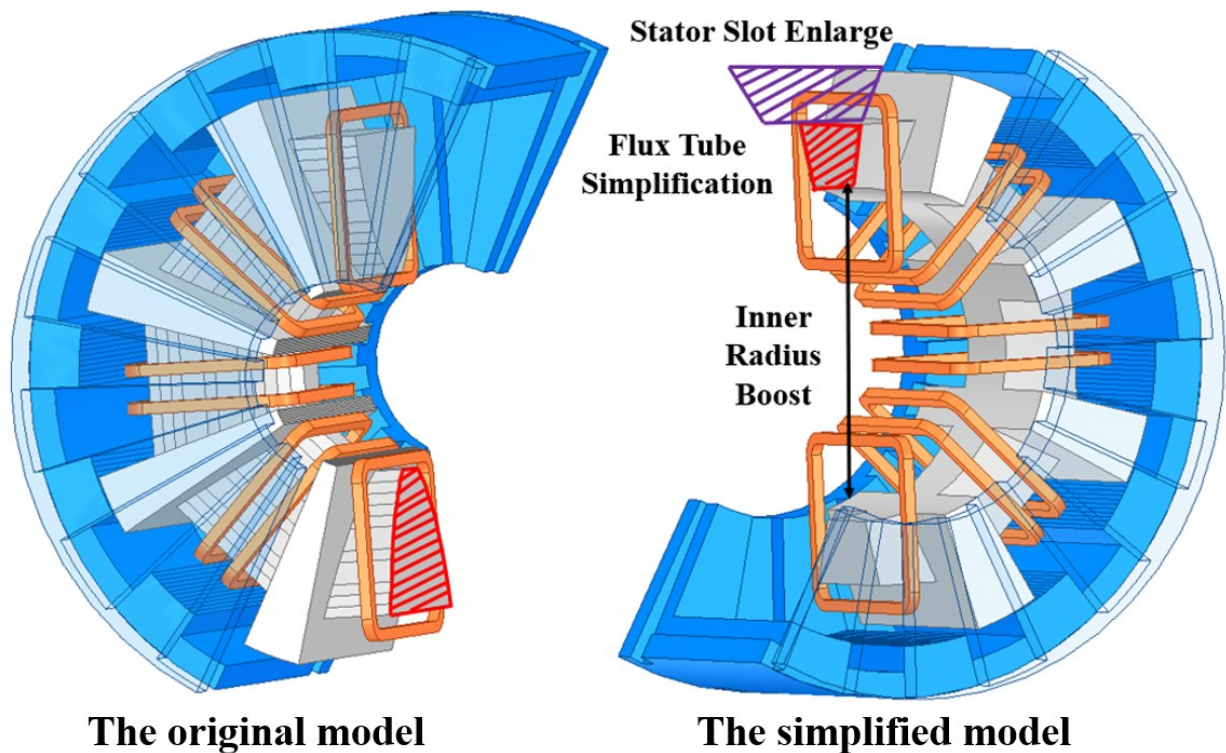


Figure 2.31: The simplification of 3D 08/14 SRM [30].

To demonstrate the magnetic field distribution in the 8/14 machine, the information is collected by multiple radial probe sheets and axial probe sheets. The location and layout of these probe sheets are shown in the Figure 2.32 [30]. The corresponding radial flux plots and axial flux plots are shown in Figure 2.33 and Figure 2.34 respectively. As discussed above, the dominating magnetic flux paths have spans of 45° , therefore, the axial probe sheets placed in the range from

20° to 70° could capture the useful information of the magnetic field yielding the positive torque. As the stroke of the 8/14 SRM is around 6.428°, the simulation step size is set to an increment of 0.8035° to obtain a better resolution. There are 16 simulation points in each stroke. The axial probe sheet at 0° demonstrates the flux distribution at the center of the flux tube between stator pole #1 and stator pole #8 where the stator pole #1 is energized by phase A and stator pole #8 is not energized. The magnetic flux density in this flux tube mainly reveals the magnitude of fluxes linking the energized stator pole #1 and the energized stator pole #6 which is 135° away from stator pole #1. As the rotor poles align to the energized stator poles, the magnitude of flux density at 0° gradually increases and reaches its peak when the rotor poles fully align with stator pole #1.

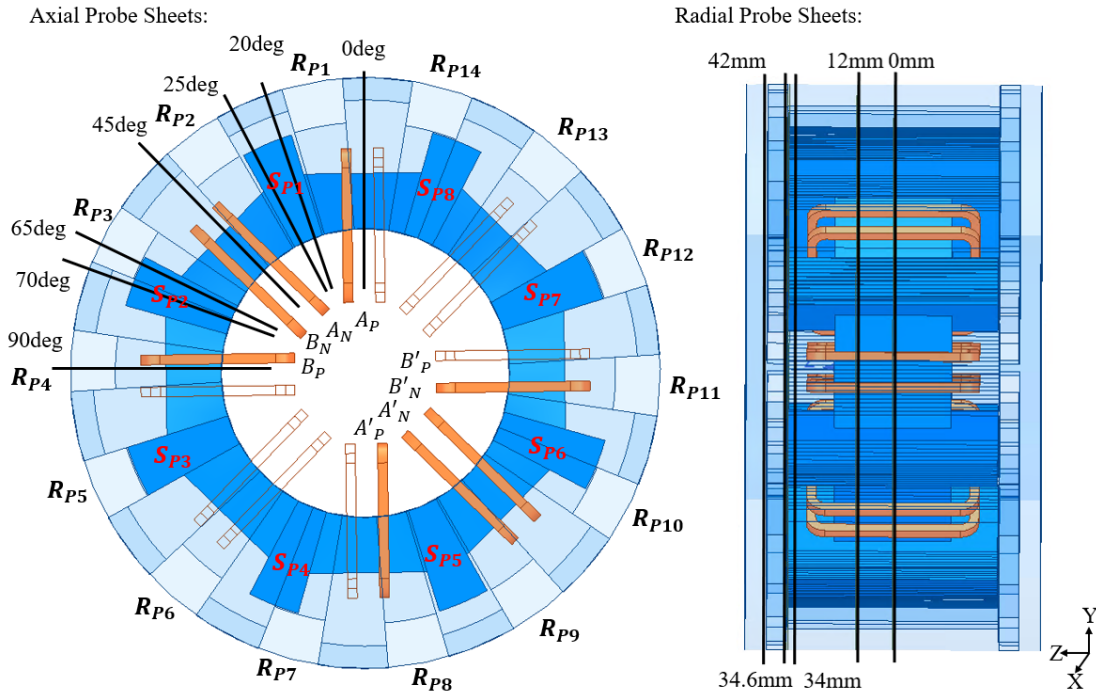


Figure 2.32: The geometrical layout of radial probe sheets and axial probe sheets [30].

The probe sheets at 20° and 25° capture field distribution on two sides of stator pole #1. Since circulating flux should not exist in the stator, the flux densities of flux plots at 20° and 25° could

be similar. Theoretically, the magnetic fluxes generated by windings A_N and B_N could be captured by the probe sheet at 25° . The magnetic fluxes generated by in windings A_P and B'_N could be captured by the probe sheet at 20° . The radial magnetic paths and axial magnetic paths share the flux tube such that bulk saturation in flux tube will affect both strength of the radial field and axial field. In the design phase, once bulk saturation is found in the flux tube, the geometry of the stator should be revised. The probe sheets at 20° and 25° do not only reveal saturation in the flux tube, but also reveal the distribution of majority of magnetic fluxes. It is known that the magnetic fluxes tend to travel through the path with and minimal magnetic reluctance and as such the flux distributions in stator poles would not be even. It is good to note that the regions that are prone to saturate to add more magnetic materials to them. On the other hand, the saturation status of those regions could indirectly hint to the torque capacity of the model. At the unaligned position, the average flux density is about 1.6 Tesla which is way below the knee point of 2.4 Tesla. When the rotor poles overlap with the stator poles, the edges and stator pole tips marginally saturate at around 2.4 Tesla as shown in Figure 2.32. The joint regions of stator pole and flux tube marginally saturate as well. As shown by probe sheets at 65° and 70° , the stator pole tips, edges, and joint regions of stator poles and flux tube exhibit high flux densities around 2.0 Tesla to 2.2 Tesla which is close to the knee points. At the beginning of this stroke, the rotor pole #3 and stator pole #2 have 50% overlap. This is the half-aligned position of the stator pole #2. As the rotor pole moves to the exact aligned position, the stator pole is slightly over the marginal level of saturation. However, saturation at the aligned position could be acceptable since the stator pole #2 will not participate in the next stroke. Also, it is not expected to harvest decent reluctance torque at the aligned position. By reviewing the flux plots at 20° ,

25°, 65°, and 70°, it could be seen that the saturation pattern of the radial field and axial fields are similar. The radial fluxes and axial fluxes flow through joint regions of flux tube and stator pole and leave the corresponding stator pole surfaces. The even contours of flux plots at 20°, 25°, 65°, and 70° can be seen. The orange contours denote the regions conducting high magnetic flux density. Those regions are generally the joint regions of stator poles and flux tube, pole surface, and pole corners. Adding more magnetic material to the joint regions and smoothing the geometrical turning could be helpful to mitigate local saturation while the modifications must be done under the space constraints. Figure 2.35 presents two groups of arrows: 1) the red arrows marking the shortest paths potentially offering the minimal reluctance but prone to saturation 2) the dark blue arrows marking the longer paths which are less prone to saturation. The probe sheet at 45° demonstrates the field information of the flux tube between stator pole #1 and stator pole #2. The overall flux density of the tube is slightly under the knee point of Hiperc 50 along the rotation which means the flux tube is fully exploited. This will determine the minimal dimensions of the flux tube. Considering the installed toroidal windings, the whole stator configuration acts as a magnetic ‘voltage source’ with internal impedance. Further shrinking the flux tube will significantly magnify the impedance of this magnetic ‘voltage source’, which is prohibited. From the flux plots at all rotor positions, the magnitude of the flux density in rotor core including the radial part and axial part are quite below the saturation point such that reluctances of the rotor part could be negligible as compared to the reluctance of the stator core. The radial probe sheets capture the radial magnetic field information. In Figure 2.34, the flux plots at 0mm and 12mm are roughly similar but the magnitude of the flux plots at 12mm are slightly higher than those at 0mm. The magnetic paths close to stator surfaces will be overall

shorter. This confirms that the magnetic fluxes tend to follow through regions close to the stator surface as shown in Figure 2.35. In conventional radial flux machines, the magnetic field distribution in radial planes along the axial direction could be similar or identical.

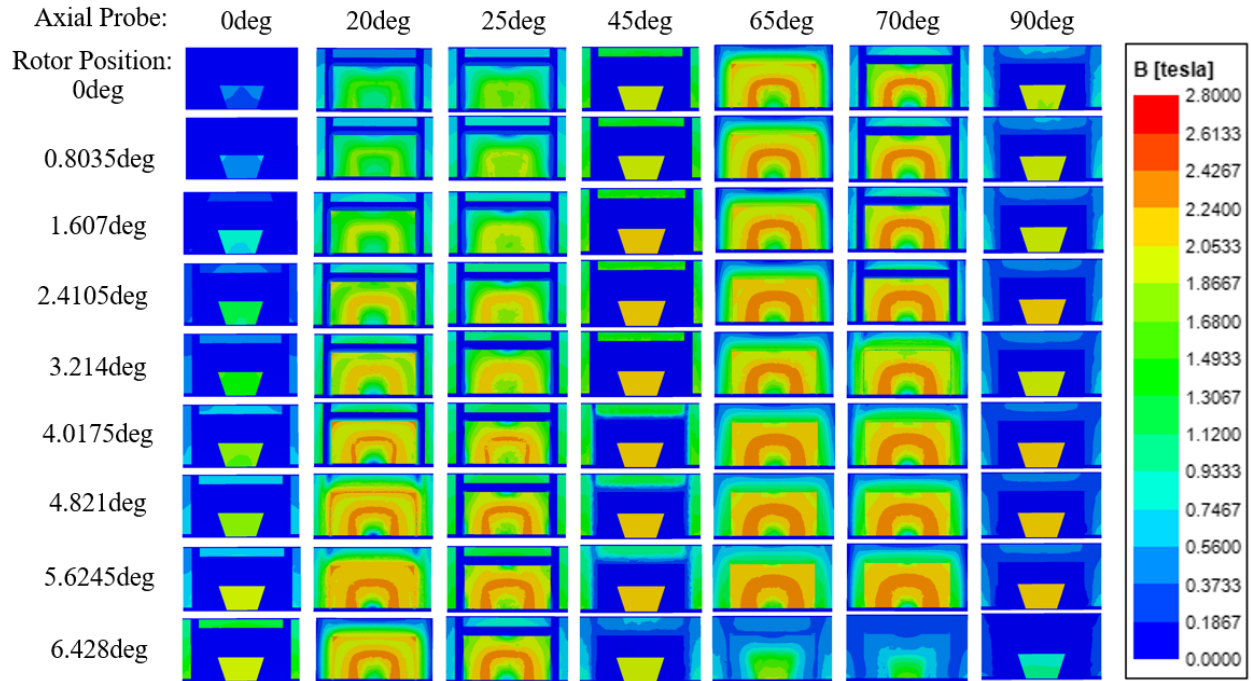


Figure 2.33: The magnetic flux distribution printed on axial probe sheets.

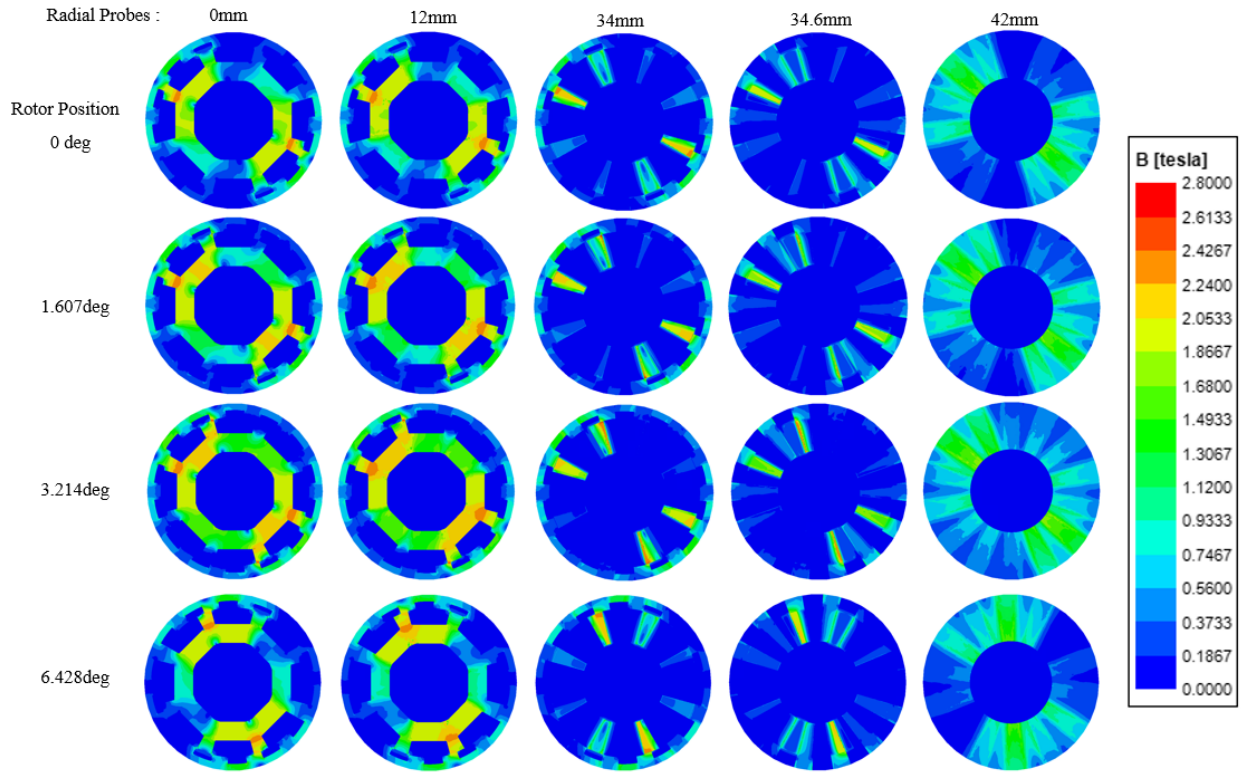


Figure 2.34: The magnetic flux distribution printed on radial probe sheets.

The radial probe sheet at 34mm captures the magnetic field distribution at 0.1mm underneath the axial stator pole surface which could represent the field information of the axial stator pole surface. The thin layer of magnetic core material on the stator pole surface generally saturates during the alignment process so does the stator pole corners. The dark orange regions and red regions in the radial flux plots denote the saturated areas which are corresponding to the overlap regions between the axial rotor poles and axial stator poles. As the rotor poles align to the axial stator poles, the saturated area increases until it fully covers the axial stator pole surfaces. The flux plots at 34.6mm present the radial field information at 0.1mm underneath the axial rotor pole surfaces. The area showing high flux density above 1.8 Tesla could match the overlap region between the axial rotor poles and axial stator poles. The overall flux density of the rotor is lower than flux density of the stator. The flux plot at 42mm demonstrates the magnetic field of

the joint regions of axial rotor poles and axial rotor back iron. Due to the large axial surface, the magnetic reluctance of back iron is quite small. The back iron does not saturate in the whole stroke. Given the magnetic flux densities of the axial rotor back iron, thickness of the back iron could be further reduced. However, the machine design has to consider the mechanical integrity since the either side of the axial rotors have to transfer the total torque. The minimal thickness of axial rotors must be ensured to avoid deformation. To investigate the mechanical integrity of the 3D flux 08/14 SRM, the co-simulation between Twin Builder and 3D Maxwell simulations have been proceeded.

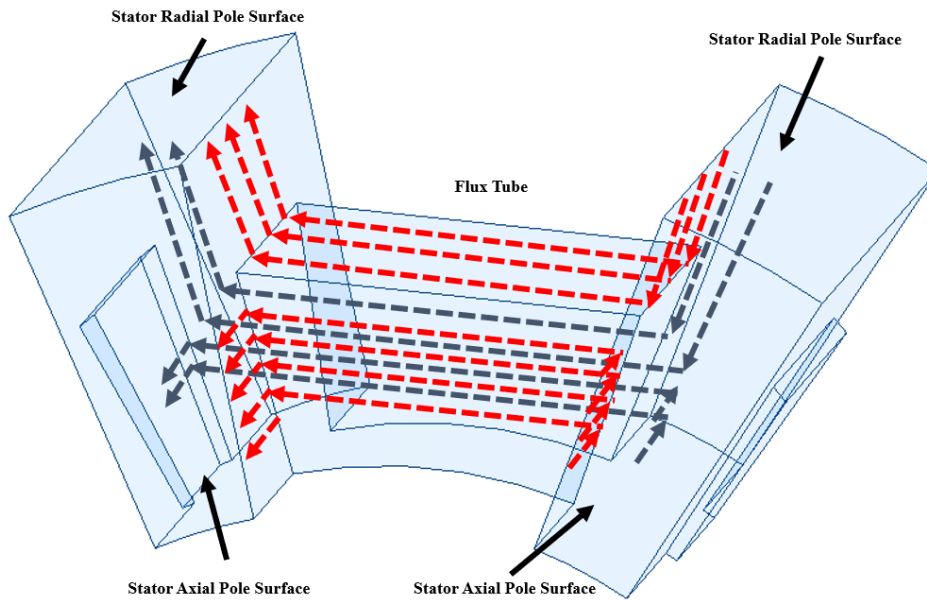


Figure 2.35: Illustration of the tendency of the 3D flux.

The post-processing analyses, the steady-state mechanical structural and the steady-state thermal simulations are conducted to observe the equivalent tensile stress, deformation, and steady-state temperature of the machine structure. The co-simulation diagram in Twin Builder is presented in Figure 2.36. It has four asymmetric bridges. The four phase outputs are connected to the 3D FEA model. The current control is implemented by hysteresis control for simplicity and tight current

regulations. The magnitude excitation can be calculated from the maximum current density, stator slot area, filling factor, and number of turns in windings. To keep certain magnitude of MMF per phase, the number of turns in windings and the magnitude of phase excitation can be accordingly adjusted. With higher number of turns, a phase could conduct less current while a phase has to conduct more current with a smaller number of turns. Since the copper area is fixed, the magnetic wire gauge will be large when a smaller number of turns are used. The magnetic wire gauge will be small when a greater number of turns are used. From the perspective of Ohms loss, the thermal stress of the two cases under the same MFF could be similar. This is because resistance of small wire is higher than big wires. The phase current and number of turns per stator slot in the co-simulation are chosen at 35.3 Arms and 20 turns, respectively.

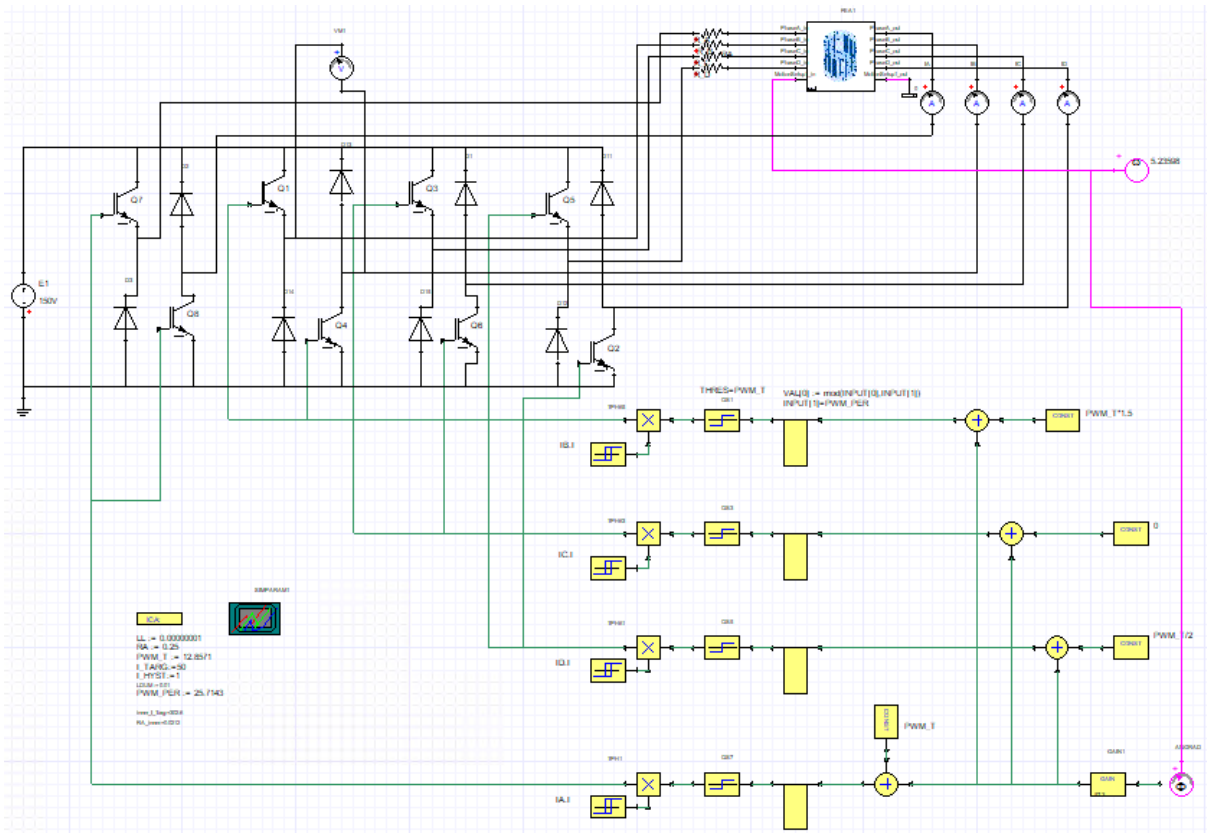


Figure 2.36: The diagram in Twin Builder.

The motor has an exterior rotor and an interior stator. Per mechanical concerns, the machine should be used as a high torque and low speed motor. The rotational speed determines the core loss, winding loss, and switching loss. At low speed, the impact of centrifugal force on the rotor may be insignificant. For simplicity, the model in Twin Builder is simulated at 180rpm. The simulations with even lower speeds are spared here since they have less thermal stress and mechanical stress. The dynamic simulation relies on the 3D magnetic transient solver. Different from the 3D magnetic static solver, the transient solver cannot apply adaptive mesh treatment to the simulated model such that the mesh of the 3D model in transient simulations will be much coarser than it is under magnetostatic solver. In terms of 3D static torque calculation, the results of magnetic transient solver will be much less than the calculated results of magnetostatic solver. As a result, the dynamic co-simulation between Maxwell and Twin Builder could only provide fundamental insights. The periodic static torque and current profiles are shown in Figure 2.37 [30] and Figure 2.38. The simulated current chattering can be seen in Figure 2.38, which also affects core loss of the magnetic core.

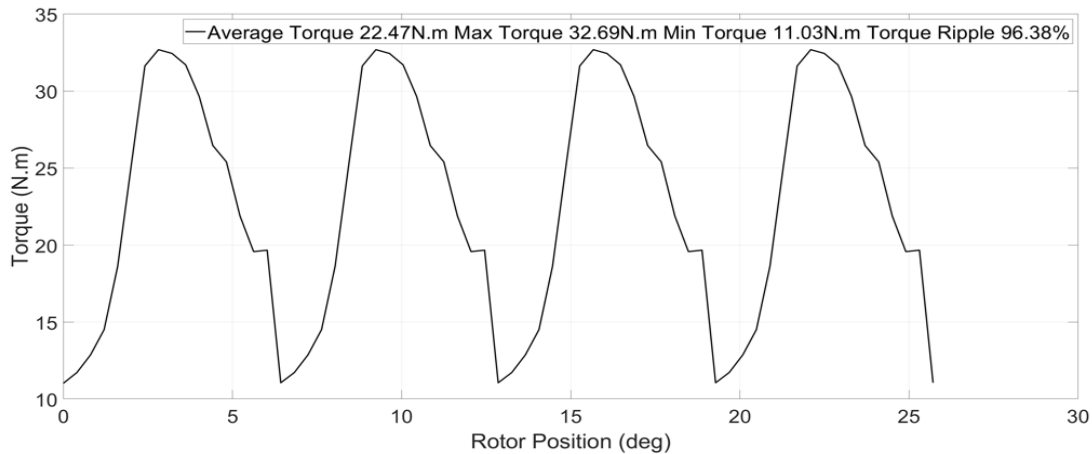


Figure 2.37: The static torque of 08/14 3D Flux SRM at 180rpm [30].

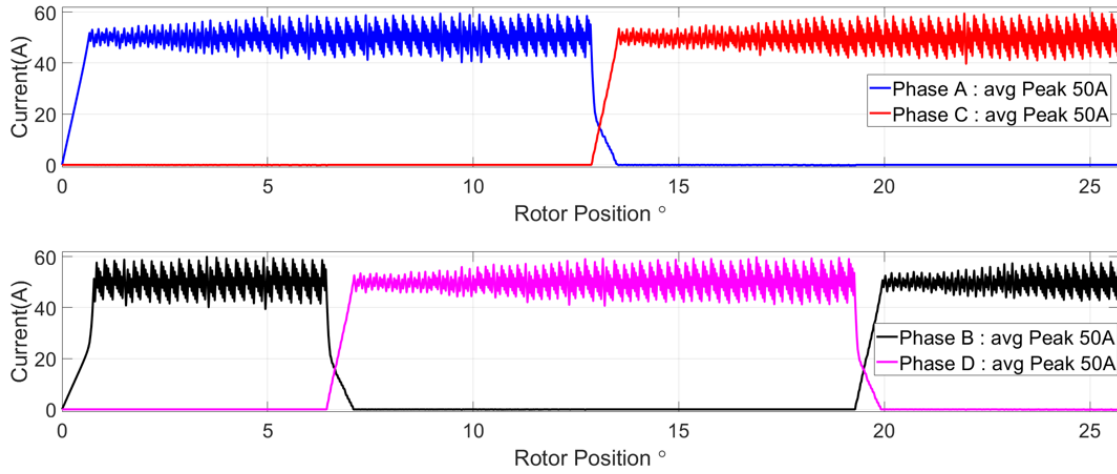


Figure 2.38: The hysteresis control based current profiles of the co-simulation.

The core loss data of the stator and rotor are shown in Figure 2.39 [30]. The high core loss at the beginning of the simulation is due to the startup transient. The total core loss is about 18W at 180rpm where the rotor core loss is estimated at 2.9W and the stator core loss is estimated at 15.1W. The rotor core loss is lower because of the overall low magnetic flux density. The simulated B-H curve of Hiperco 50 is based on the data of Hiperco 50 27-mil lamination. In practice, if one wants to simplify the fabrication, a solid magnetic core may be used for machining. The data of mechanical properties of the Hiperco 50 27-mil laminations are purchased from the *MagWeb.com*. In industry, not many applications will adopt solid magnetic core due to the concerns of core loss such that the data of Hiperco plate is not available in online data base. Thus, the core loss in real condition could be higher than this 18W. Per phase current of $35.3A_{rms}$, the feasible magnetic wire size could be AWG 9. The winding resistance is estimated around 38mOhm per phase where the length of the phase winding is estimated by the stator length, the radial distance between stator outer radius and inner radius, and the number of turns in the windings. The AC resistance is ignored due to the low fundamental frequency.

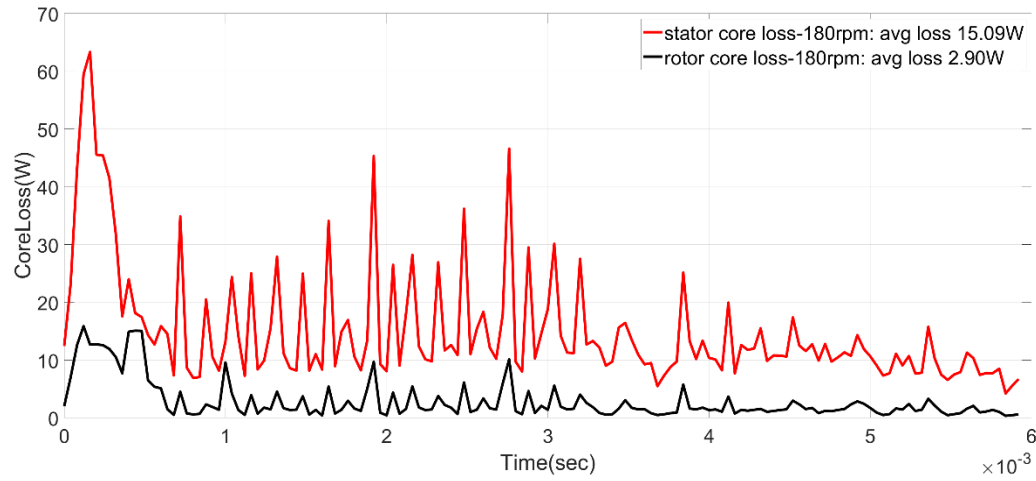


Figure 2.39: The power loss profiles of stator and rotor.

The DC-resistance-based copper loss is estimated at 47.8W per phase. Since the copper loss is calculated by the RMS current, the total copper loss of 191W has been evenly applied to each stator slots. Under the steady state thermal condition, the heat generation of windings is directly coupled to the outer surfaces of the stator and the inner surfaces of the rotor. Assuming that the ambient temperature around the motor is stable at 25°, the heat transfer coefficient of outer surface of stator and inner surface of rotor is set to $10W/m^2$ assuming an air convection. The heat of stator also transfers to the inner surface of the rotor through the airgap. The stator support with shaft is designed with bores which are used to route the wire and air cooling. The inner surfaces of the stator and support are assumed to have heat transfer coefficient of $30W/m^2$. The steady state simulation of the thermal response is proceeded. The model is viewed from the center clipping plane. The thermal images are shown in Figure 2.40. The final temperatures of the stator and rotor are around 66 C°.

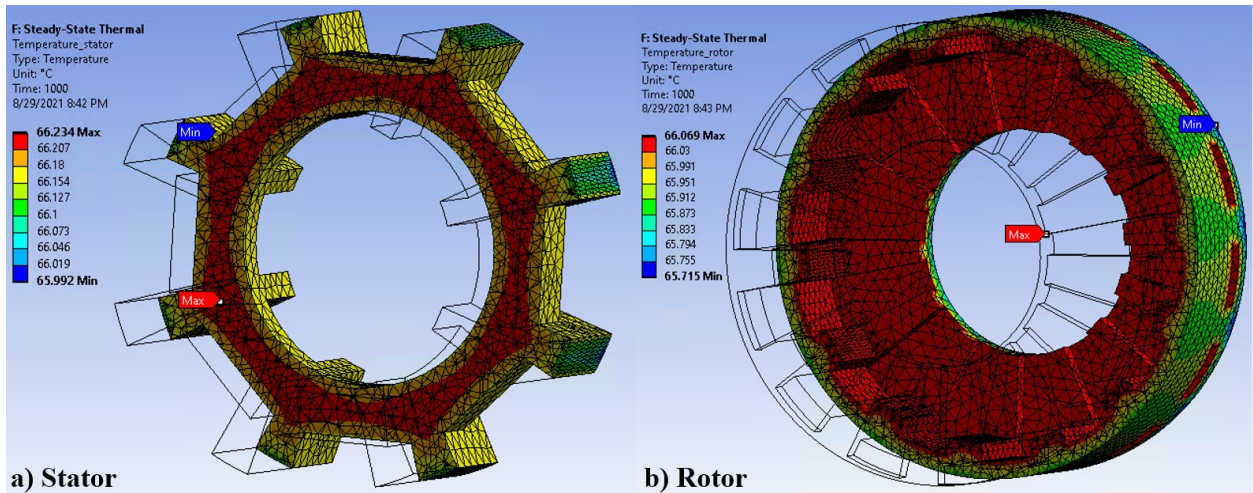


Figure 2.40: The saturated thermal image of stator and rotor.

Furthermore, the surface force densities of stator and rotor at aligned position are imported to the static structural analysis model. This is because at the aligned position, the radial force and axial force will be maximized. The equivalent tensile stress (von Mises) and deformation of the exterior rotor is shown in Figure 2.41 while those of stator are shown in Figure 2.42. The stress and deformation of stator support with bearings is shown in Figure 2.43. Per the mechanical properties of Hipercro 50 from Edfan.CO [27], the tensile strength and yielding strength of the magnetic core are 814 Mpa and 435Mpa respectively. According to the static simulation, the maximum tensile stress at stator tip is about 3.1Mpa. The maximum stator deformation of stator is about 4.8um. The maximum tensile stresses of rotor and stator support are 4.3 Mpa and 2.4um. Those of stator support are 4.3 Mpa and 3.2um.

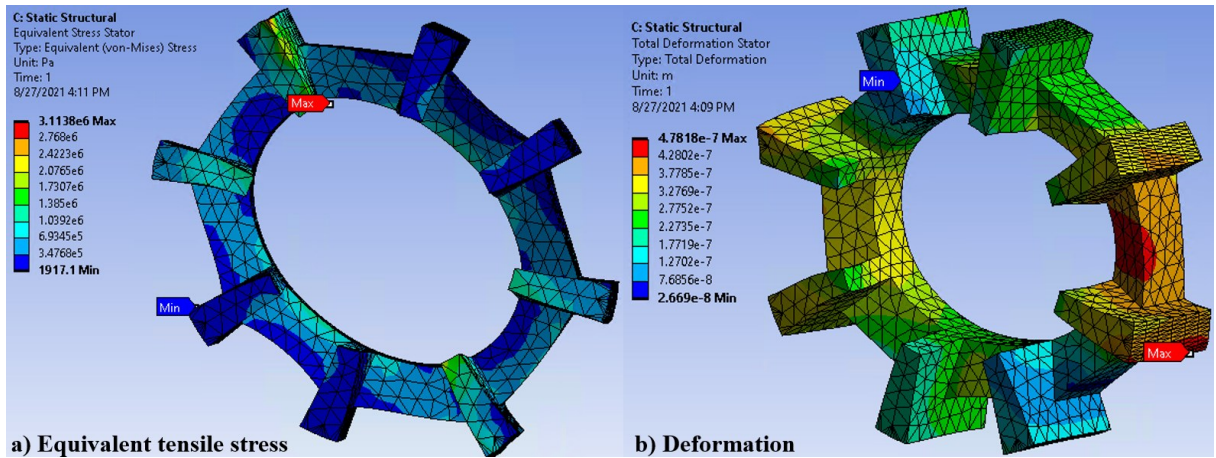


Figure 2.41: The equivalent tensile stress and deformation of stator.

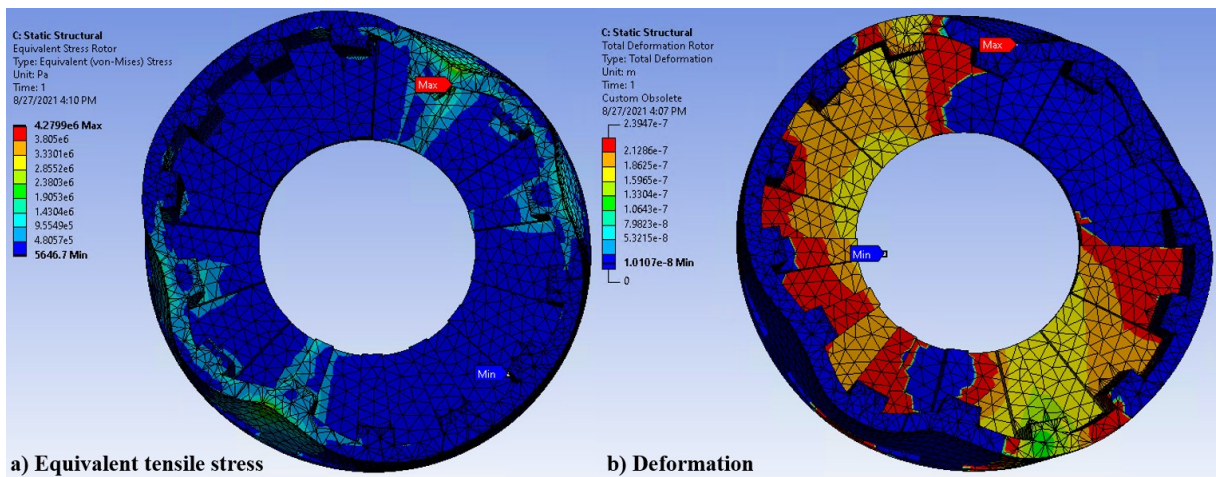


Figure 2.42: The equivalent tensile stress and deformation of rotor.

The pressure and deformation of machine core are far less than the material rating. The stator support frame is built by stainless steel 316 with tensile stress around 600 Mpa and 310 Mpa such that the mechanical integrity of the machine is an issue.

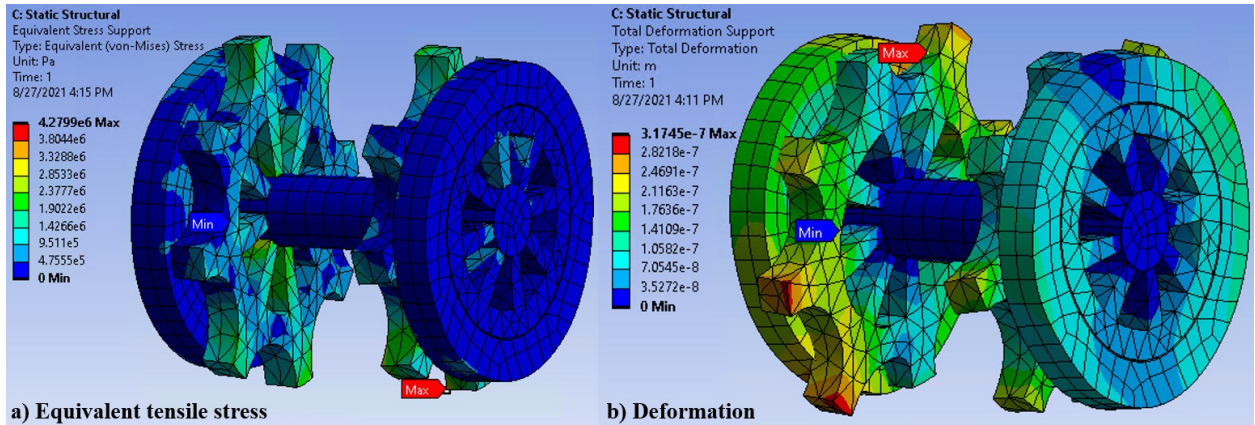


Figure 2.43: The equivalent tensile stress and deformation of stator support and shaft.

Until now, the design methodologies and original model of SRM with the proposed 3D flux structure have been discussed. Since the theoretical advantages and mechanical properties of the model with the double-salient structure has been seen, the next step is to seek the possibility of improving the model and handling the inherent drawback of the configuration—the existence of the magnetic paths yielding negative torque. The second revision of the proposed structure is discussed in Chapter 3.

CHAPTER 3

MODIFIED SEGMENTED ROTOR 3D FLUX SRM

The primary reason of major revision of the 08/14 3D flux model is to seek the possibility of removing the magnetic flux contributing to negative torque. Those magnetic paths could exist in a double salient-pole SRM with a higher number of rotor poles than the stator poles [21-24].

There are two choices to resolve the unwanted magnetic paths: 1) suppress the strengths of unwanted magnetic paths; 2) change the magnetic field distribution. In the literature, some specified structures like C core, U core, and modular stator have airgap and flux barriers between stator poles. The magnetic fields will be forced to locally distribute. The traversed fluxes between stator poles will be inherently weak since they must travel through large portions of airgaps. The C core or U core stator are generally adopted for radial flux machines. The rotor normally has salient poles on two ends of the rotors which are exactly underneath the poles of 'C' core or 'U' core. Other parts of the rotor do not join the torque generation and are only used for mechanical support purposes. The space utilization will be lower than conventional machine, especially when the machine is merged with the axial flux structure. The second option is the modular stator structure as studied in [16]. The clearance between each stator module could be helpful to reduce the magnitude of the unwanted flux vectors. However, the mechanical integrity will be one major issue for the modular stator structure, even if the structure is only designed for radial flux. To improve the mechanical integrity of the modular stator, the Li [16] filled core materials in the clearances between each stator module only for supportive purposes. The stator structure is optimized through elimination of fluxes that flow through the supportive magnetic bridge. This concept may not apply to the interior stator applications because transverse fluxes

appear once there is any core material filled between interior stator modules. In addition, it is not clear as to how merge the axial modular structure with the radial modular structure. As a result, the modular structure is not a feasible idea for the proposed structure. The last option is to utilize the segmented rotor structure which has non-magnetic material built in between each magnetic rotor segment. Different from double-salient pole structure, the segmented-rotor machine has a better torque capacity and a higher machine efficiency albeit with a higher torque pulsation [25, 26]. In academia, the segmented-rotor SRM has drawn significant attention over the past decades. [26] claims that the torque capacity of a SRM could be increased by roughly 40% after switching to the segmented-rotor structure. The superior output torque of a segmented-rotor SRMs comes from its specified structure: 1) the non-magnetic material built-in between magnetic rotor segments guarantee the minimal phase inductance at unaligned positions 2) the rotor segments magnetically short the adjacent two stator pole guarantee the maximum phase inductance at aligned position. These two scenarios are shown in Figure 3.1.

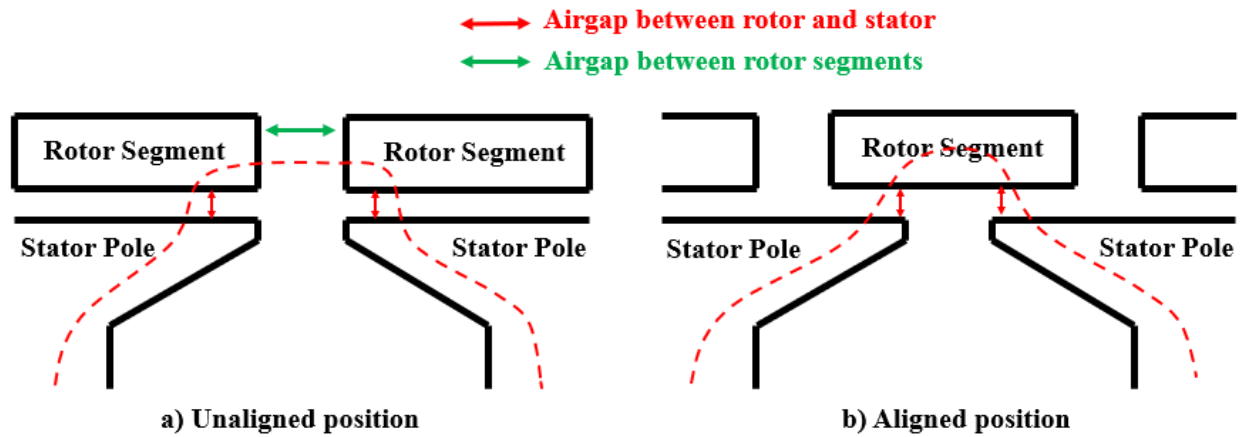


Figure 3.1: The overlap pattern of segmented-rotor SRM.

In a double salient-pole SRM, the magnetic flux travels from one rotor pole to another through the rotor back iron such that the length of the magnetic path is long. Depending on the excitation

pattern, those magnetic paths could be shortened. However, the magnetic field design is still not flexible, compared to segmented-rotor SRMs. This is because the fluxes in rotor back iron seek any chance to return to the stator as long as paths can offer smaller reluctances. Undesired magnetic paths could appear as the number of rotor poles increases. On the contrary, the field design could be straightforward in case of segmented-rotor SRMs. With the interleaved layout of segmented rotor structure, the magnetic fluxes can be locally confined, which boosts the design flexibility. As long as the arc of the non-magnetic segment is equal or larger than the clearances between two adjacent stator pole tips, the minimal phase inductance could be achieved. The stator poles of a segmented rotor SRM are built with pole shoes to widen the stator pole arcs such that the rotor segments can overlap with stator poles in advance. Also, most fluxes travel through the stator pole shoes such that the geometrical length of closed magnetic flux paths could be shortened. By proper trend studies, the overlap area between stator poles and rotor segments could be reasonably enlarged to boost the flux linkage at aligned positions. In addition, different from the salient-pole rotor structure, the rotor segments could be fully embedded into the non-magnetic rotor frame to smooth the rotor inner surface. Notably, at high speeds, the windage loss could be minimized. In short, replacing the double-salient pole structure with the segmented-rotor structure is the reasonable step to improve the torque capacity of a SRM with the proposed 3D flux structure. There could be multiple targeted features including torque pulsation, overload capacity, efficiency, vibration, etc. However, since this is still a novel structure, the study procedures have to be detailed. To narrow down the scope, the top objective of this study is to seek the maximum output torque. For the segmented-rotor structures, the trend study on pole configurations of 12/08, 12/10, 12/14, 12/16, 16/12, 16/14, 16/22 has been

proceeded with no satisfactory results. Considering unipolar excitation and successive stroke torques, the valid pole configurations are limited. The unipolar excitation is commonly adopted for SRM for simplicity and lowering design cost. Even though the phase current direction is not critical in harvesting single phase torque, the transients of current directions are not preferred. In fact, the bipolar excitation does matters for some pole configurations such as 08/06 and 16/12. If it is needed to harvest successive stroke torque from these two pole configurations, bipolar excitation having an electrical cycle of 8 strokes are required. The current directions of the first four strokes will be reversed with respect to those of the last four strokes. The full bridge topology could handle this scenario while the consequent cost, core loss, current transients, operation complexities are obvious drawbacks. After multiple trials, under the same space constrain (2.55Liters), the valid option that could satisfy most aspects is still the 8/14 configuration. In the following section, the geometry layout of the segmented-rotor 3D flux 08/14 machine is reviewed.

3.1 *The machine structure*

The magnetic rotor segment does not have to have a rectangular cross-section as shown in Figure 3.1. The cross-section of rotor segment is trapezoid and has taper on each side. Given 2D/3D simulation results, it is observed that the rectangular cross-section of rotor segment is not always helpful to develop higher average output torque. This is because the magnetic flux density of the magnetic paths significantly increases when the edge of rotor segment close to the edges of stator pole tips. The locally saturated regions could be small due to the decent magnetic material available on the magnetic paths. Per the discussions in Chapter 1, the reluctance torque is derived from the changes of the phase inductance. If the saturation status of the rotor segment does not

have obvious variations around the alignment, the developed reluctance torque could be small. Alternatively, the yielded torque profile could present a rising ramp at the beginning of stroke then rapidly decaying along the rotor position. This scenario may frequently occur in the exterior rotor SRM. The proper shapes of interior segmented rotor could be investigated such that the geometry study of the rotor segment discussed here is confined to the scope of the proposed structure. The cross section of the radial part of the optimized segmented-rotor 08/14 SRM is shown in Figure 3.2. The brown pieces are the radial rotor segments. The gray pieces are non-magnetic segment. The cross-section of the rotor segment has stairs on both sides in order to simplify the optimization process and fabrication.

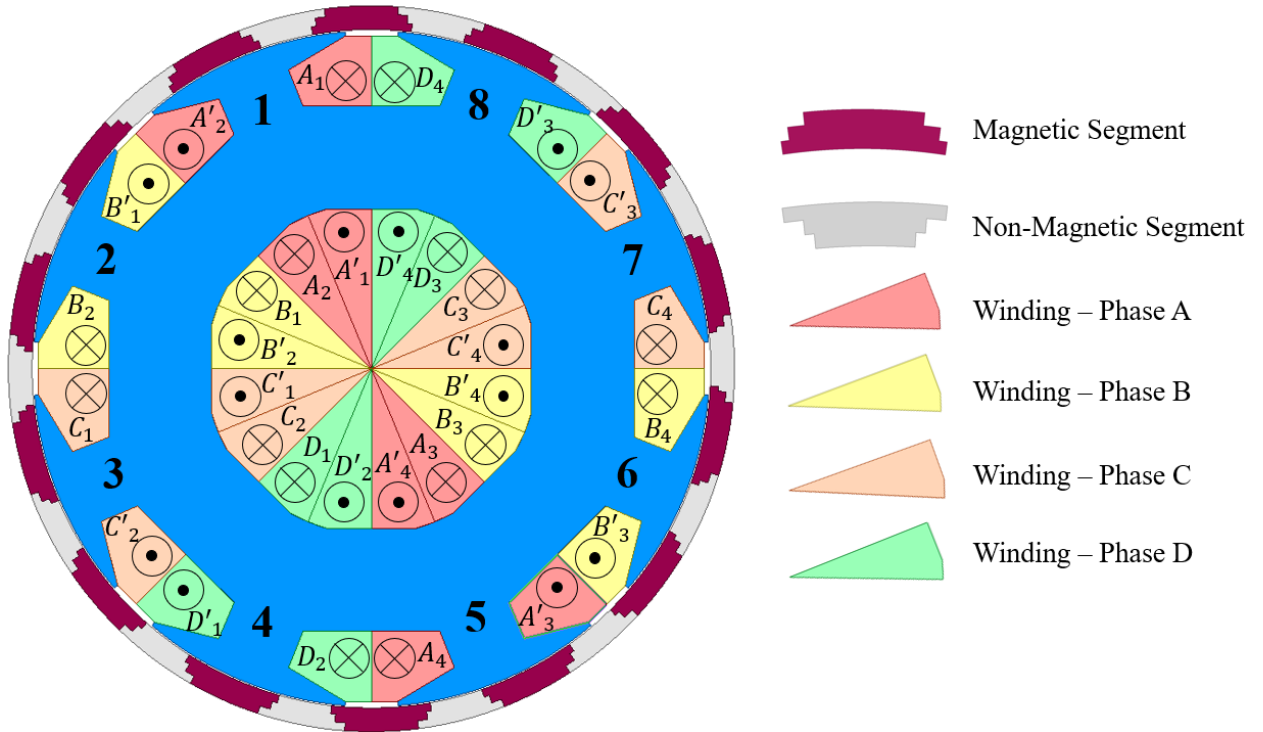


Figure 3.2: The cross section of optimized 08/14 SRM.

The actual rotor fluxes will not exactly travel along the stair-stepping edges. On the contrary, they will travel through the regions nearby the rotor inner surface and segment tips. The

magnetic flux paths of the radial model at unaligned position and aligned position are shown in Figure 3.6 in the next section which discusses the magnetic field of the segmented-rotor 08/14 SRM. The radial rotor segment has the identical cross-section along the axial direction. Pieces of radial rotor segment, non-magnetic rotor segment, axial rotor segment, and non-magnetic rotor segment are presented in Figure 3.2.

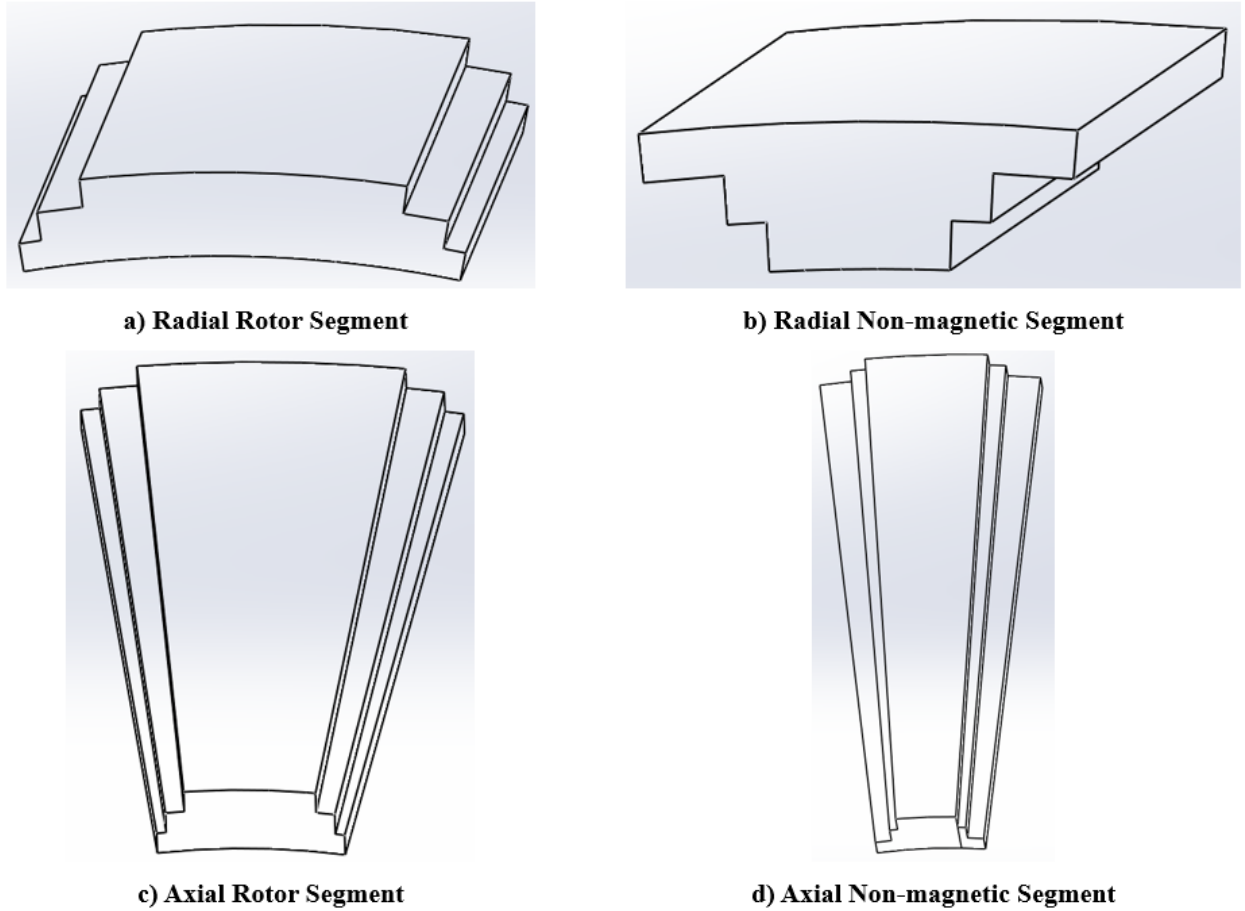


Figure 3.3: The rotor magnetic segments and non-magnetic segments.

In Figure 3.3, both the radial rotor segments and radial non-magnetic segments have 3-stairs structures where arc of each layer has been optimized to improve the output torque. This is to simplify the optimization workload. The arc of each layer of the radial non-magnetic segment is designed to match the radial rotor segment. The length of the radial rotor segment is optimized as

well where the length of the radial rotor segment could be in a range of ($L_{stator}, L_{stator} - 2mm$). This is to balance the cross saturation in radial fields and axial fields at the corners and edges of radial rotor segment, radial stator pole, axial rotor segment, and axial stator poles, which are shown in Figure 3.4. The GA optimization of this model had been applied for long periods of time in the past such that the size of the data base is quite large and convincing. The radial rotor segments and axial rotor segments have different arcs. This is the optimization outcome. Since both radial flux structure and axial flux structure offer different reluctance profiles, the final output torque will be the summation of the torque harvested from the radial flux structure and the torque harvested from the axial flux structure. To avoid cross saturation and cross coupling in both flux structure, they are expected to be different. In Figure 3.4 b), the axial segment has a smaller arc to avoid early saturation due to the extended radial stator pole tips. Note that the early saturation will drop the output torque.

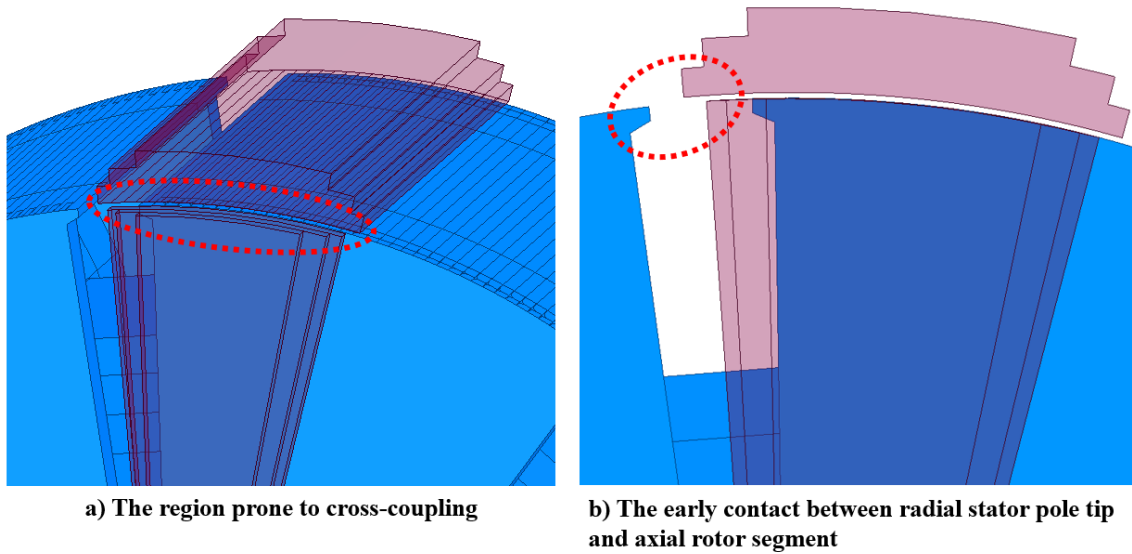


Figure 3.4: The region prone to the cross-coupling issues.

Given the recorded data, the torque capacity of the model with the identical radial segment arcs and axial segment arcs are not quite satisfactory. Therefore, the radial rotor pole arc, radial stator

pole arc, axial rotor pole arc, and axial stator pole arc are set to different values. No matter whether which one of radial stator pole arc or axial stator pole arc is larger, the arcs of counterpart rotor segments are made smaller to avoid early-stage cross contact between radial flux structure and axial flux structure. In Figure 3.4 b), the large radial stator pole arc is helpful to make early contact between radial rotor segment and radial stator pole such that the startup torque could benefit from a sharper ramp. At this position, the edge of axial rotor segment is still a bit away from the edge of axial stator pole. The output torque derived from the axial part of the machine is not significant, yet it becomes significant once the edge of axial rotor pole moves closer to the axial stator pole. The saliency of the axial flux structure could be theoretically helpful in boosting the middle stage of the total torque profile. Each flux structure could perform differently during rising and falling in the corresponding torque profile. One has freedom to choose different pole arcs and select various risings and falling edges of the respective torque profiles. In fact, the optimization algorithm implemented this task. One can filter out the models presenting unsatisfactory torque profiles. It is difficult to tell the significant impacts of early-stage cross saturation on the total torque generation process. The model presented here is one of the top selections provided by the optimization. Given the overlapped area between axial rotor segment and axial stator pole, there could be considerable increment in co-energy contributed by the alignment of axial flux structure. This may be able to explain that the results of the global Genetic Algorithm present some discrepancies due to the variation of axial rotor segment arc given the nonlinear relationship. The 3D model of the inner stator of the segmented-rotor SRM is shown in Figure 3.5. The clearances between stator pole edges are generally smaller than those in double-salient pole 08/14 SRM as shown in Figure 2.32. This is because most magnetic fluxes

are locally distributed. Also, the magnetic paths will be only formed in the aligning rotor segments and stator poles due to the absence of magnetic back iron. To exploit the segmented-rotor SRM, the stator pole arc is enlarged as much as possible to shorten the loops. There are two criteria: 1) there will be a minimal clearance per rated excitation to avoid too much fringing flux linking two adjacent stator pole tips; 2) there will be an optimal clearance to ensure the maximum increment of co-energy. To test the theoretical advantages of the segmented-rotor 8/14 SRM, the flux tube is still designed with curved edges which only guarantee the minimal stator slots. The axial stator pole has a 5-mm thickness sector shape and internally merges with the stator pole base as shown in Figure 3.5 d). As discussed in previous sections, the axial flux SRM has strong axial electromagnetic force acting on axial stator poles due to the large axial stator pole surface and small axial airgap. To avoid potential deformation, the thickness of the axial stator pole could be marginalized.

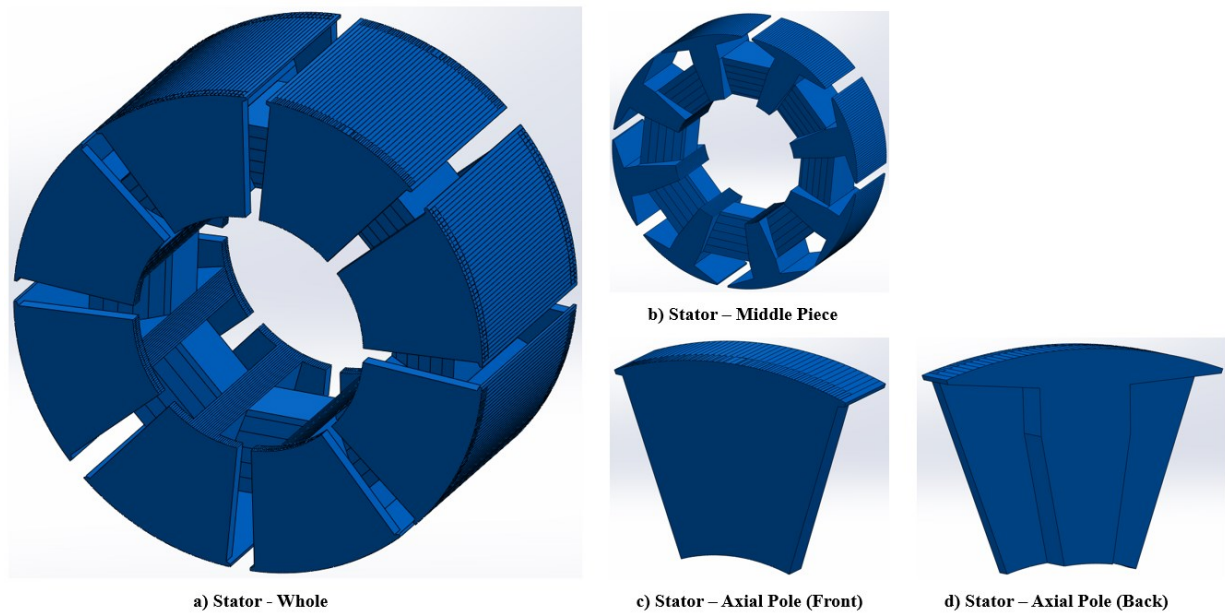


Figure 3.5: The 3D model of the inner stator of the segmented-rotor 08/14 SRM.

The axial stator pole could be machined separately and installed on the stator middle piece. Perhaps in the future, the 3D printing technique could print the magnetic core materials with better resolution such that the stator could be built as one piece. In short, the proposed interior stator challenges the current fabrication techniques and is assumed to be built piece by piece for now. Additional magnetic material on the stator pole will be used for providing mechanical stiffness and may not contribute to the magnetic performance.

3.2 The magnetic design

The pattern of magnetic field distribution in the radial part is similar to that in the axial part. The magnetic design will be first illustrated by the 2D model. The stator core of the 8/14 machine could be energized by single phase or two phases. Due to the concentrated winding installed on each stator pole with 180° space shift, the machine provides single phase torque. The span of the positive torque zone is 12.857° . Each positive torque zone consists of two strokes. Each stroke has a span of 6.428° .

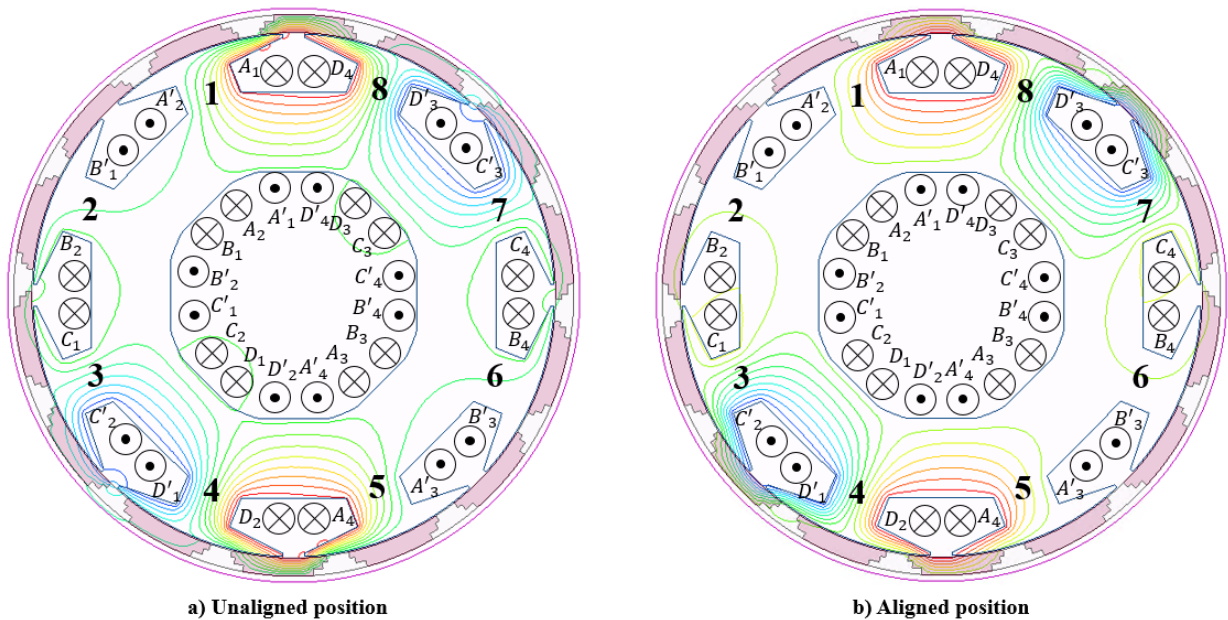


Figure 3.6: Flux lines in radial part of segmented-rotor 08/14 SRM.

For single phase torque, the rotor segment will rightly align with the centerline of two stator poles. At this position, the rotor segment will symmetrically overlap with two adjacent stator poles. To exploit the full capacity of the machine, stroke excitation (double-phase excitations) is needed such that the MMF in active stator slot could be doubled. However, the alignment pattern of double-phase excitation is different from that of single-phase excitation as shown in Figure 3.6. In terms of double-phase excitation, the rotor segment close to stator pole #1 receives the magnetic flux from the stator pole #8. The stator pole #8 is energized by the outgoing phase D. Along the rotation, the material density of magnetic paths linking stator pole #1 and stator pole #8 does not vary much such that the yielded torque may be insignificant. Most of the reluctance torque generated by the magnetic reaction between stator pole #8 and stator pole #7. At the unaligned position, the magnetic paths are dominated by non-magnetic materials. Along with the rotation, the portion of non-magnetic material are gradually replaced by magnetic materials of the rotor segments. In addition, the portion of magnetic materials increases till the rotor segments fully align with stator poles. There is a small portion of flux linking stator pole #7 and stator pole #6 at the beginning of the stroke. Along with the rotations, the portion of non-magnetic materials enlarges and then reduces such that the variation in loop reluctance could be negligible. Once the rotor segment moves closer to the stator pole #7. The magnetic paths could contribute to generation of positive torque. Moreover, this rotor segment will keep harvesting the positive torque in the incoming stroke. As a result, the resulting impact of magnetic path linking stator pole #7 and stator pole #6 could be unknown in the first stroke. The electrical period of this segmented-rotor 8/14 machine has four strokes, namely: phase D/C ON \rightarrow phase C/B ON \rightarrow phase B/A ON \rightarrow phase A/D ON. To illustrate the 3D magnetic field in the segmented-rotor 8/14

SRM, the radial probe sheets and axial probe sheets are inserted into the model to capture the field information. The span of the probe sheets is from 25° to 110° . Since the model is excited by stroke excitations, magnetic fluxes will travel through stator poles #1, #8, #7, #3, #4, #5, and aligning rotor segments. The field distribution is symmetric such that all probe sheets are placed on one side.

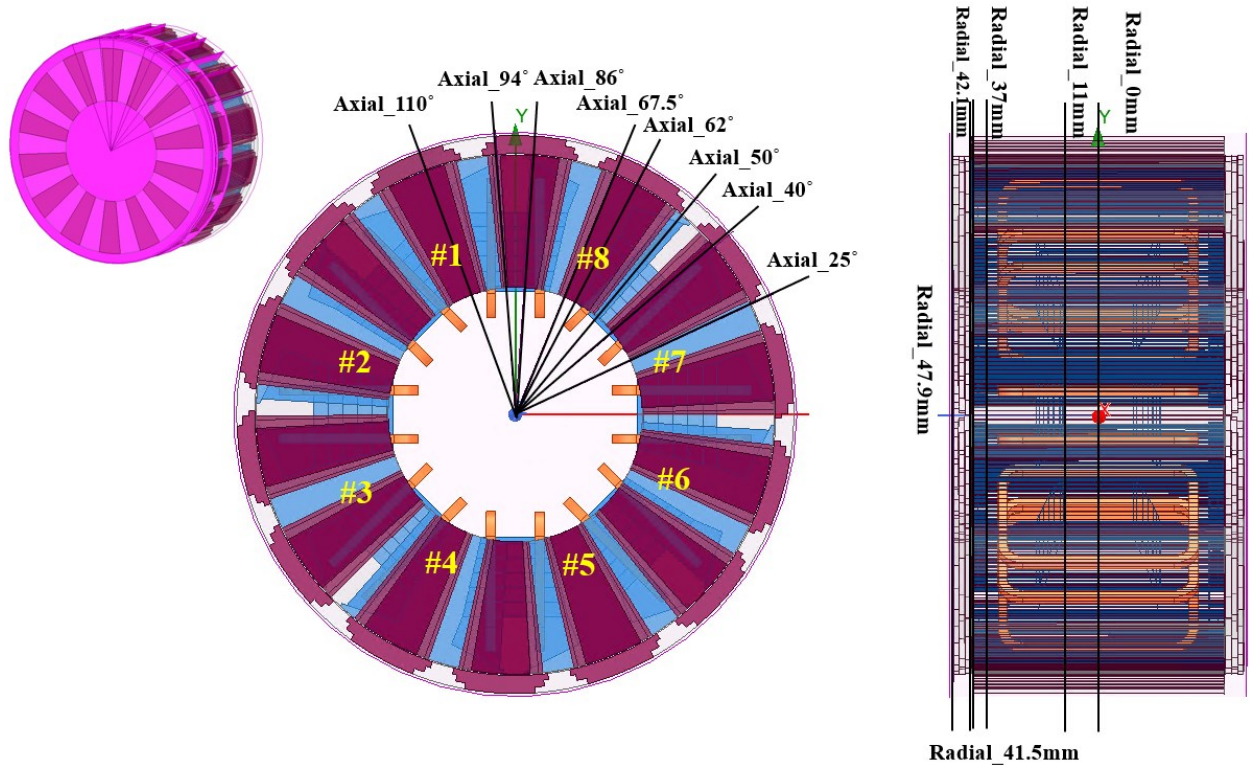


Figure 3.7: the geometrical distribution of probe sheets.

The axial probe sheet at 110° is placed on the right side of the stator pole #1. In Figure 3.7, the stator pole #1 captures the traveling fluxes from stator pole #8 which stem from phase D. At the same time, magnetic path linking stator pole #8 and stator pole #7 are energized by both of phase D and C. Hence, the axial probe sheet at 110° should not observe saturation. This could be verified by Figure 3.8. This is a segmented-rotor 8/14 machine having a stroke of 6.428° . The flux plots of each probe sheets at a few rotor positions are presented in Figure 3.8. The rotor

position starts from the beginning of a stroke to the end of the stroke with a 1.6071° increment. The axial probe sheet at 94° captures the field information in the pole tips of stator #8 and the corresponding cross-sections of rotor segments. At the beginning of the stroke, the radial rotor segment and axial rotor segment exhibit overlap with the pole tips of the stator #1. Along with the rotor movement, the local saturation is noted as shown in Figure 3.8. This explains that the magnetic paths linking stator pole #1 and stator pole #8 are able to generate the positive torque along the alignment. The flux tube linking stator pole #1 and stator pole #8 shows average flux density around 2.0 Tesla which is slightly below the saturation point of Hiperco 50. The axial probe sheet at 86° captures the field information of the overlapped region of rotor segments and pole tips of stator pole #8. The overall magnitude of flux density is stabilized around 1.8 Tesla. The magnetic fluxes travel through the left part and right part of stator pole #8 could show different strengths. This is because the magnetic paths linking stator poles #8 and #7 are excited by double magnitude of MMF. It is not expected to see bulk saturation in stator pole #8. Given this, axial probe sheet at 67.5° , which is right at the centerline of the stator pole, could present less flux density than that at 62° . This is because the fluxes tend to travel along geometrically shorter paths, which is confirmed by Figure 3.8. The overall magnitude of flux density at 62° is higher than that at 67.5° . The peak magnitudes of magnetic flux densities captured by both sheets are around 2.2 Tesla where the saturation points of Hiperco 50 could be between 2.2 Tesla to 2.4 Tesla. Thus, the stator pole #8 may show locally marginal saturation or slightly below saturation. Axial probe sheet at 50° points out to the flux plots at edges of stator pole #8 and the aligning rotor segment. Along the rotation, the marginal saturation occurs at edges of stator pole #8 and the aligning rotor segment. This is due to the small overlap region between the rotor segment and

stator pole tips, which is a normal phenomenon in SRMs. In fact, this is desired in the optimization process since this is helpful to smooth the reluctance profile and smooth the ramp of the phase inductance. Axial probe sheets at 40° and 25° show the field distribution on the linking stator pole #7. The flux density increases with the alignment so does the co-energy of local airgap.

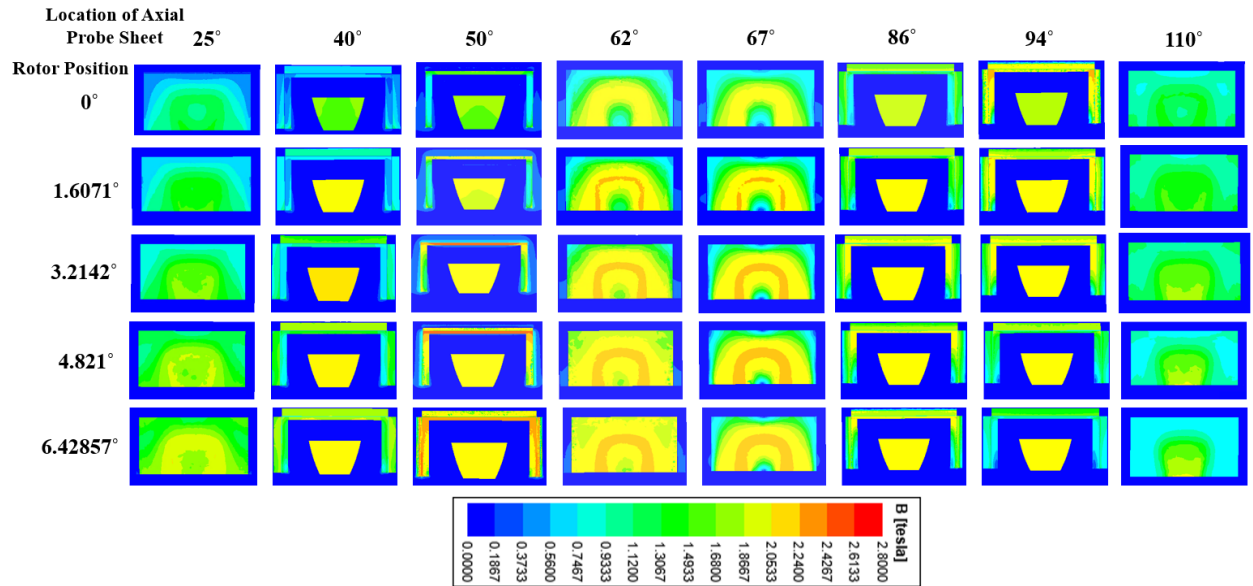


Figure 3.8: The flux plots of axial probe sheets.

The flux plots of radial probe sheets are shown in Figure 3.10. The radial probe sheet at 0mm denotes the center cross-section of the machine. It could present the typical field distribution of the radial flux structure. In Figure 3.10, the flux plots of the radial probe sheet at 0mm reveals the similar details as shown in Figure 3.8: 1) at the beginning of the stroke, the rotor segment aligning to stator pole #1, stator pole #8, and the pole tip of stator #8 demonstrate locally marginal saturation 2) the flux tube gradually presents marginal saturation as the rotor moves to the aligned position 3) the rotor segment linking stator pole #8 and stator pole #7 presents local saturation once it begins to overlap with pole tips of stator pole #8. The radial probe sheets

indeed demonstrate additional information: the stator pole base presents slight saturation around 2.4 Tesla at the aligned position. The wider pole base is preferred but enlargement of stator pole base would lead chain reactions on many other parameter revisions such as deepening the radial stator slot and shrinking volume of flux tube. Those could eventually lead to local saturation or bulk saturation at other parts of the machine. Since the scope of this study is to investigate torque capacity of a SRM with the proposed structure within a constrained space, and since this is one of the final results from the global GA optimization, it could be concluded that the marginal saturation in stator pole base would be an optimally balanced option. The flux plots of radial probe sheet at 11mm are similar to those of radial probe sheet at 0mm. This is because the machine is overall a combination of radial flux structure and axial flux structure. The radial probe sheet at 37mm points out to the field distribution on the back side of the axial stator pole while the axial probe sheet at 41.5mm points out to the field distribution at 0.1mm underneath the axial stator pole surface. The overlapped region between stator pole (#1) surface and axial rotor segment surface show high magnetic flux densities. The regions with marginal saturation are the edges and corners of the stator pole connecting both the radial stator pole surface and axial stator pole surface. As mentioned above, it could be also interpreted as cross-saturation between radial field and axial field. The magnitude of flux density distribution near the edges of stator pole #8 significantly increases over 2.4 Tesla as the rotor segment begins to overlap with the stator pole tips. The radial probe sheet at 42.1mm points out to the magnetic field at 0.1mm underneath the axial rotor segments. These can present the surface saturation status of the axial rotor segments. At the rotor positions of 4.821° and 6.42857° , only a small region marking the edges of axial rotor segments present marginal saturation since the arc of axial rotor segments

are small. The overlap regions between axial rotor segments and axial stator poles are limited. The radial probe sheet at 47.9mm demonstrates the field distribution at the back side of axial rotor segments. Basically, the average flux density at back side of aligning rotor segment gradually grows from 0 Tesla to 1.6 Tesla in the first stroke and is stabilized around 1.8 Tesla till the end of the second stroke. The 3D magnetic flux plot of the 8/14 machine at the aligned position is shown in Figure 3.9. To obtain a better view, the model is viewed from the center clipping plane, and the stator is set to 90% transparent. The yellow and green vectors have a larger magnitude from 1.6 Tesla to 2.2 Tesla. It confirms the previous statement that majority of magnetic flux is locally distributed around the active stator poles.

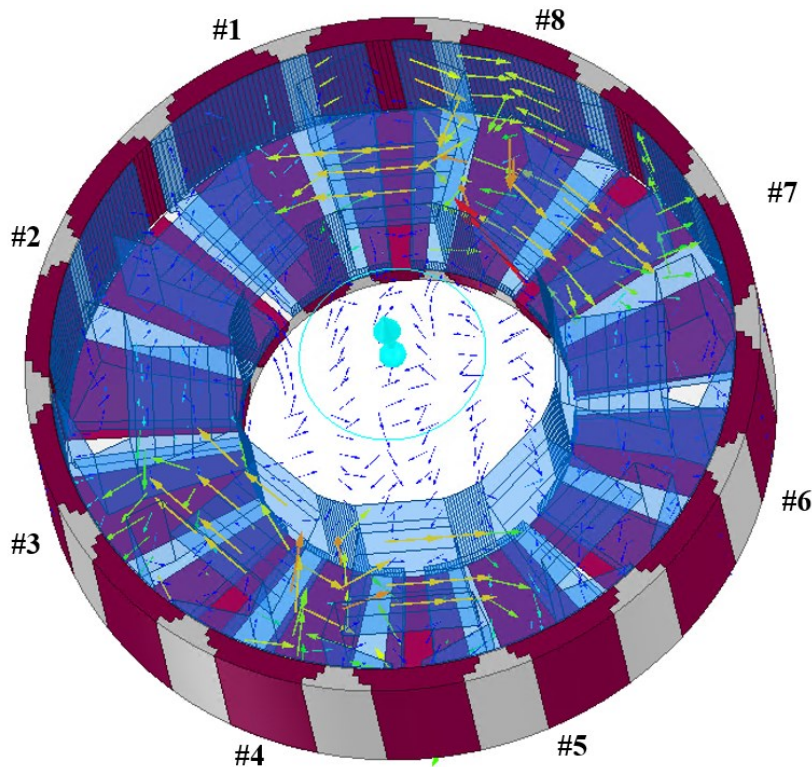


Figure 3.9: The 3D flux vector – $\frac{1}{2}$ model.

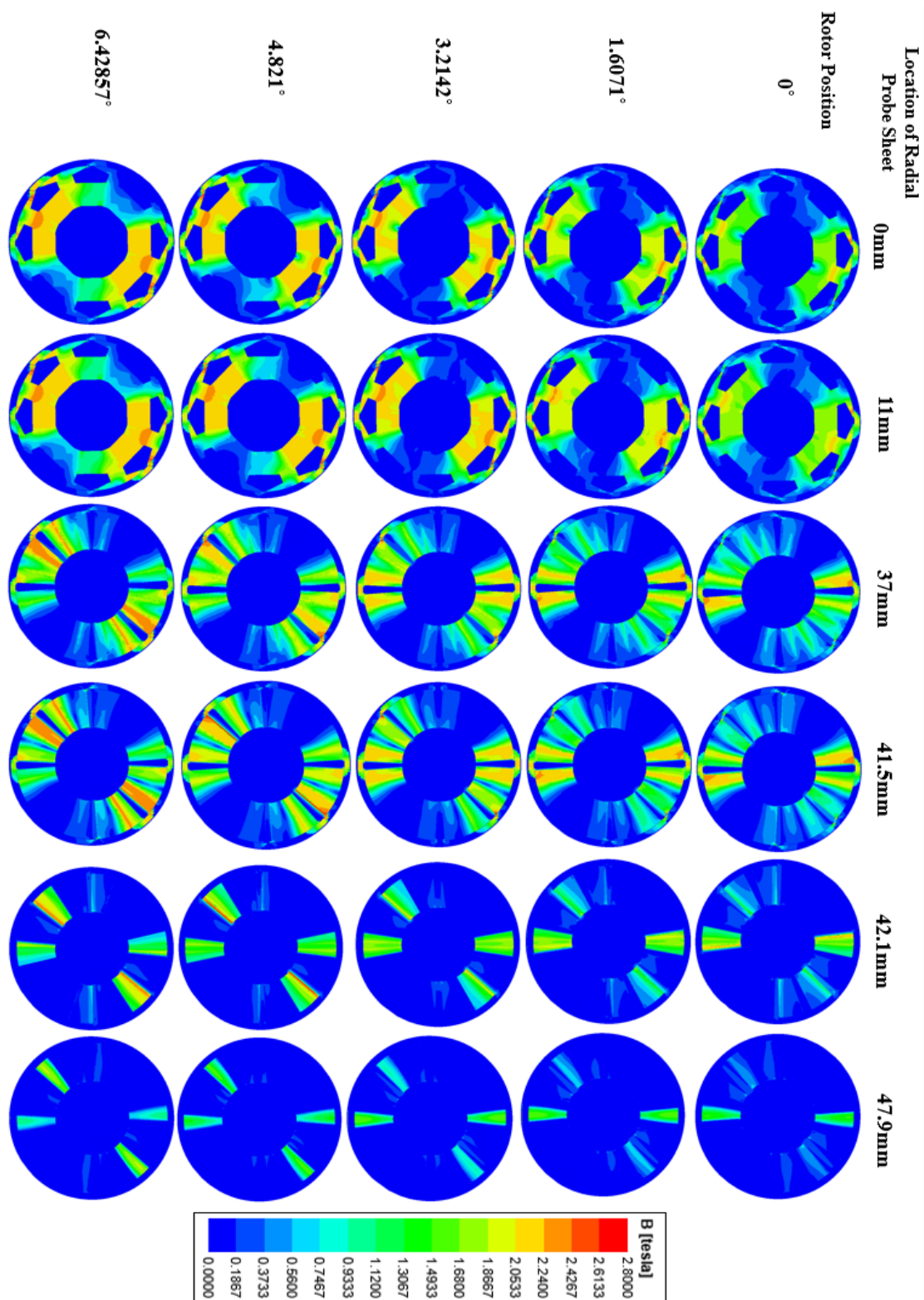


Figure 3.10: The flux plots of radial probe sheets.

3.3 *The comparison between two structures*

It is worthy to summarize the merits of the segmented-rotor SRM before presenting the comparison between two versions of 8/14 SRMs. The nominal span of the magnetic path in the double-salient pole 8/14 SRM is 45° which is the geometrical space between two adjacent stator poles. However, the minimal span of the magnetic path could be much less than 45° due to the extended stator pole shoes and pole tips. In addition, the distance by the flux travels through rotor segment is defined by the clearance between two adjacent stator pole tips. The flux linkage at the aligned position is expected to be much higher than that in the double salient-pole version. On the other hand, the flux linkage at the unaligned position can be easily controlled by manipulating the arc of non-magnetic rotor segment. The rotor segments are inserted into the non-magnetic rotor frame such that the rotor segments are not likely internally linked by traversing flux due to the absence of the rotor back iron. Hence, the unwanted magnetic paths returning to inappropriate stator poles as presented in the double salient-pole SRM do not exist in the segmented-rotor SRM. The segmented-rotor 8/14 SRM is expected to have a higher output torque than that of the double-salient pole 8/14 SRM. The optimal results of the two versions are presented in the Table 3.1. The table lists a few major machine parameters of the segmented-rotor 8/14 machine while there are more machine parameters describing finer dimensions of the machine that are not listed here due to the overwhelming data size. The high-level parameters such as OD, ID, current density, MFF per phase, and machine length are kept the same. The thickness of rotor segments and stator, and strengths of phase excitations are provided in the Table 3.1. The comparison is overall fair and can demonstrate the advantages of the segmented-rotor structure. To narrow down the scope, the optimization of the 8/14 machine is only

conducted at the rated excitation condition. The superior machine design considering overload conditions will require decent workloads of optimizations on all overload operating points. The time-consuming nature of 3D simulations would be unaffordable. So, the optimization only aims at the rate condition. The optimized model shown in Table 3.1 was simulated for overload condition as well under peak current density at 20A/mm^2 . The average load torque is around 67.3 N.m and the average peak volumetric torque density could reach 26.4 N.m/Liters .

Table 3.1: The comparison between two versions of 08/14 3D flux machine

Items	08/14 double-salient pole version (original)	Items	08/14 segmented-rotor version (revision)
Rotor Pole Arc ($^{\circ}$)	12	Radial Rotor Segment Arc 1 st Layer ($^{\circ}$)	20.8
Radial Rotor Inner Radius (mm)	78	Radial Rotor Inner Radius (mm)	86
Radial Rotor Back Iron (mm)	7	Radial Rotor Outer Radius (mm)	92
Radial Rotor Length (mm)	69	Radial Rotor Length (mm)	83.2
Axial Rotor Length (mm)	13.5	Axial Rotor Segment Thickness (mm)	6
Axial Rotor Back Iron (mm)	7	Axial Rotor Segment Arc 1 st Layer ($^{\circ}$)	18.7
Axial Rotor Outer Radius (mm)	92	Axial Rotor Outer Radius (mm)	85.6
Axial Rotor Inner Radius (mm)	43	Axial Rotor Inner Radius (mm)	42
Stator Outer Radius (mm)	77.6	Stator Outer Radius (mm)	85.6
Stator Inner Radius (mm)	43	Stator Inner Radius (mm)	43
Stator Length (mm)	68	Stator Length (mm)	83.2
Stator Pole Arc ($^{\circ}$)	12	Stator Radial Pole Arc ($^{\circ}$)	40.1
Axial Slot Area (mm^2)	560	Stator Axial Pole Arc ($^{\circ}$)	38
Filling Factor (%)	50	Filling Factor (%)	50
Airgap (mm)	0.4	Airgap (mm)	0.4
Phase Number	4	Phase Number	4
Turns Number	80	Turns Number	80
Phase Resistance (ohm)	0.25	Phase Resistance (ohm)	0.25
Peak Phase Current (A)	50	Peak Phase Current (A)	50
Average Torque (N.m)	28.46	Average Torque (N.m)	35.6
Overall Volume (Liters)	2.55	Overall Volume (Liters)	2.55
Torque Density (N.m/L)	11.16	Torque Density (N.m/L)	13.96
Torque Ripple (%)	62.8%	Torque Ripple (%)	62.30

The stroke torques of the two versions are shown in the Figure 3.11. The static torque simulated by the FEA 3D software is a periodic profile with an approximate period of 6.428° . So, one stroke profile would be sufficient to present the idea. Under the same excitation, the stroke torque of the segmented-rotor 8/14 model is overall higher than that of the double-salient pole model. It is worthy to note that some references may mention a confusing approach to calculate the average torque related to the average stroke torque and number of strokes per revolution. In

fact, the stroke number per revolution would be an integer. The static torque of every stroke should be identical such that the average stroke torque is sufficient to present the final average torque per revolution. In this study, the average torque of a machine is calculated by its maximum periodical torque profiles.

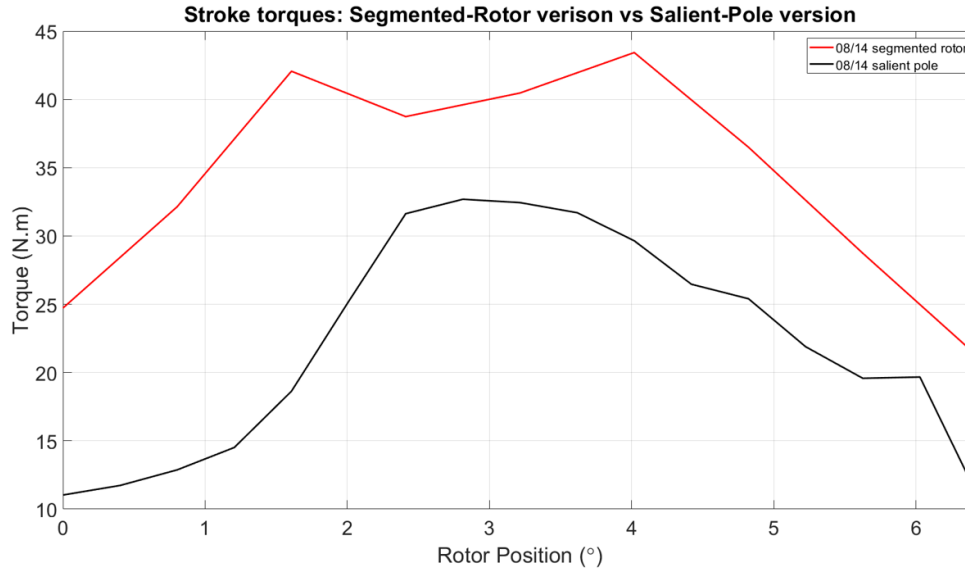


Figure 3.11: The stroke torques of two 08/14 models.

3.4 The second revision on segmented-rotor 3D flux 8/14 machine

Given Figure 3.8 and Figure 3.10, it may not be fully certain to say that the magnetic field design would not partially harvest negative torque. In Figure 3.12, a rotor segment linking stator pole #1 and stator pole #8 reaches the theoretical minimal reluctance position at t_0 where the phase D is active, but phase A is inactive and inversely connected to the DC bus. At the end of stroke, t_1 , the rotor segment passes the minimal reluctance position which may theoretically result in generating negative torque. The significance of such negative torque is not clear since it is difficult to peel the true negative torque from the stroke torque due to the highly coupled contents. However, it is not reasonable to ignore potential design issue. As a result, the magnetic

design is changed, and the concentrated windings are replaced by the simple toroidal windings. Conventional machine design is usually derived from the perspectives of stator pole. In the segmented-rotor version, the aligned position for each stator pole does not mean the aligned position for every stator slot. However, the output torque in the segmented-rotor version is harvested from all aligning rotor segments.

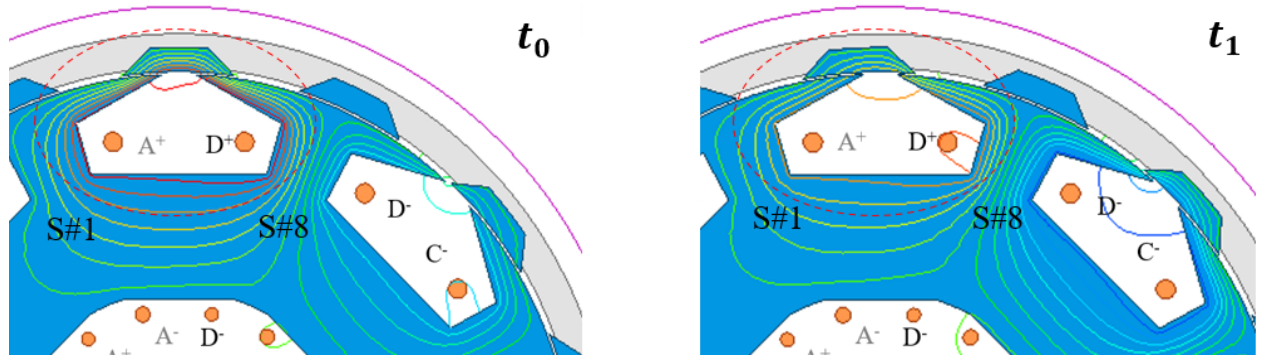


Figure 3.12: The ambiguous design issue.

In this case, placing two different phase windings in every stator slot is unnecessary and inappropriate. It is expected to have single-phase toroidal winding in each stator slot such that every phase can have independent control of the alignment. In every stator slot region, the magnetic paths linking two stator poles and the nearby rotor segment can be flexibly turned ON and OFF. The modified winding configuration is shown Figure 3.13. Once the rotor segment linking stator pole #1 and stator pole #8 reaches the aligned position, phase A could be turned off immediately to avoid potential negative torque. Meanwhile, the phase D is constantly active and phase C should be turned on. With the same parameter shown in Table 3.1, the average torque of the segmented-rotor SRM with the new winding configuration could be as high as 42 N.m. The average volumetric torque density is increased to 16.47 N.m/Liters. However, the new winding configuration for the segmented-rotor SRM could suffer from the imbalanced excitations. As for

the interior stator, not all pole configurations of the inner stator SRM are applicable. In addition, the feasible pole configuration requires specific winding configurations which may put additional constraints on the operations as the case discussed here.

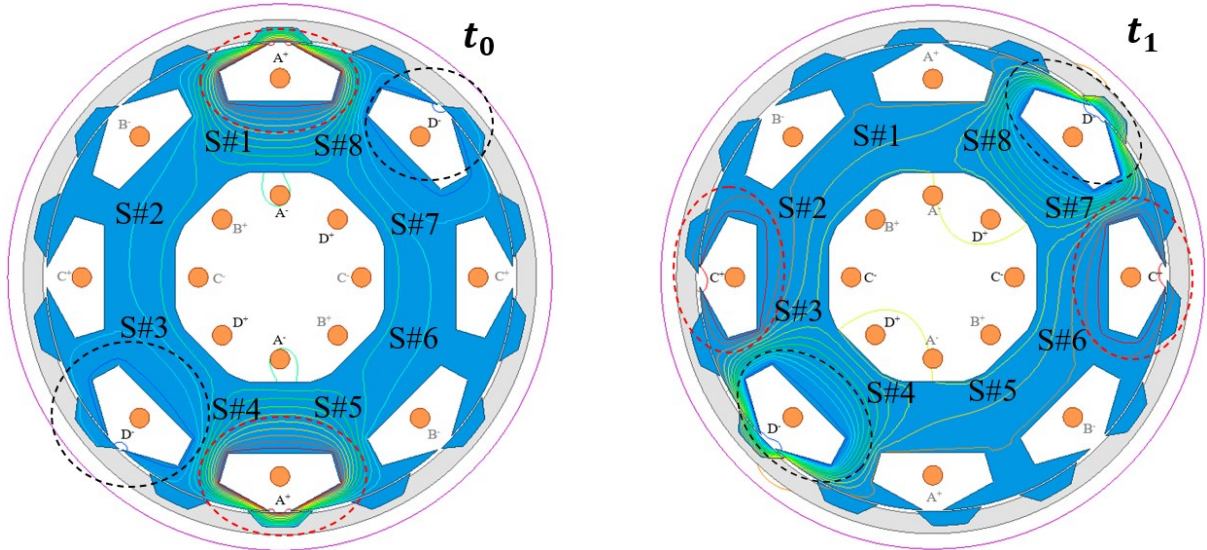


Figure 3.13: The new winding configuration of segmented-rotor 08/14 machine.

From Figure 3.13, it could be interpreted that two toroidal windings on two sides of a stator pole have to carry the same amount of MMF to avoid circulating magnetic flux in the stator core. In the normal operation, the phase excitations are controlled by hysteresis controller which introduces current ripples due to the chopping. So, it is impossible to achieve two phase currents which are stable at the same value without any variation. It is worthy to check the magnetic field distribution in the inner stator core with two active phases with small amount deviation in currents. In the Figure 3.14, the phase D current is 50 Amps, and the phase C current is 49 A. There is about 40 Ampere Turns discrepancy between phase D and phase C. The majority of positive torque could be still harvested (see the magnetic paths in stator slots of phase D) while the partial inner stator core works as inductor which will yield additional core loss, eddy current loss, and unnecessary local saturations.

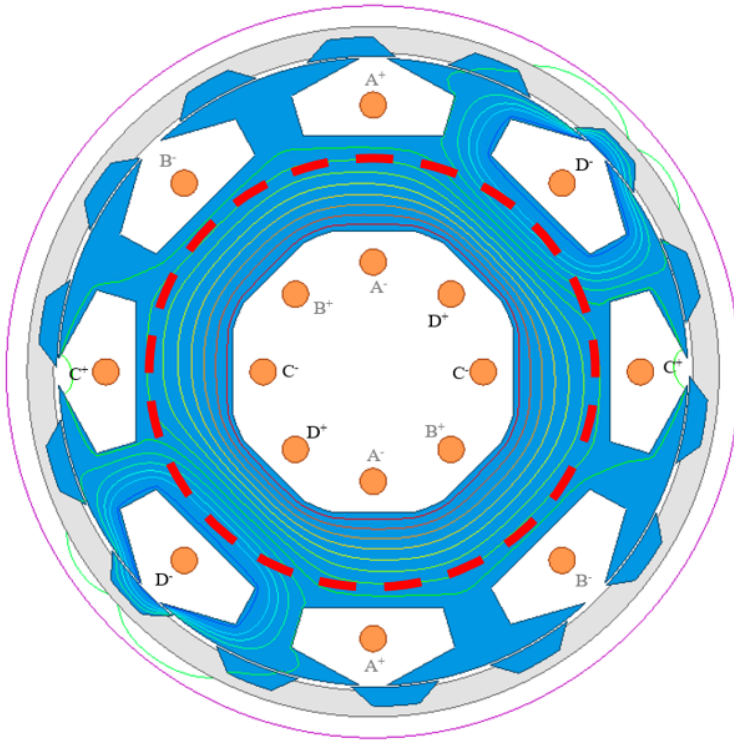


Figure 3.14: The circulation magnetic flux due to the discrepancies in excitations.

In short, if circulating magnetic paths appears in the inner stator, the magnetic design will be abandoned no matter how the theoretical superiority of the model can be under the ideal operations because the ideal operation will not happen anyway. To overcome the issues of circulating magnetic flux, the pole configuration of the machine must be changed. The prerequisites of the machine structure are summarized as follows:

- 1) Each phase must have independent control over the according stator slot
- 2) The machine must have single phase torque
- 3) The structure must inherit the advantages of the 8/14 machine discussed before
- 4) The revision must be done with the same dimension constraint

These selected requirements brought design ambiguities for a while in the past. Many pole configurations and winding configurations for 3-phase machine, 4-phase machine, and 6-phase

machines have been tried. Those polyphase machines are commonly seen in the literature, but the inherent structure cannot simultaneously satisfy the above four criteria.

All requirements cannot be simultaneously fulfilled until a 5-phase machine is considered. In addition, the closed configuration for a 5-phase machine is 10/18 machine which only require minimal revision of the 08/14 structure. Different from 4-phase machine, the ideal positive torque period of the 10/18 machine contains two consecutive strokes which has a period of 4° . The positive period of a phase is 8° while the full cycle of 5 phases is 20° . The calculations of the positive torque period and stroke are not derived by the conventional formulas. Instead, the proper operation of the 5-phase machine is found out by examining the 2D model. The rules for conventional polyphase machine do not seemingly hold for a 5-phase machine. The magnetic paths of the 5-phase machine are shown in Figure 3.15 where both torque mode are presented. As expected, the 10/18 machine has single torque available which means that each phase can independently energize its local magnetic paths without needing the counteracting flux raised from adjacent phase. This critical feature provides significant flexibility to machine operations and makes the 10/18 model a truly practical model. The 10/18 model also possesses short local magnetic paths which could be even shorter than those in the 08/14 model while the maximum stator slot area will be shrunk due to the limited space. The 10/18 model still offers satisfied high output torque. The simulation results of the 10/18 model and the down-scaled version will be introduced in the Chapter 5. In the next chapter, the optimization process of the machine design will be illustrated.

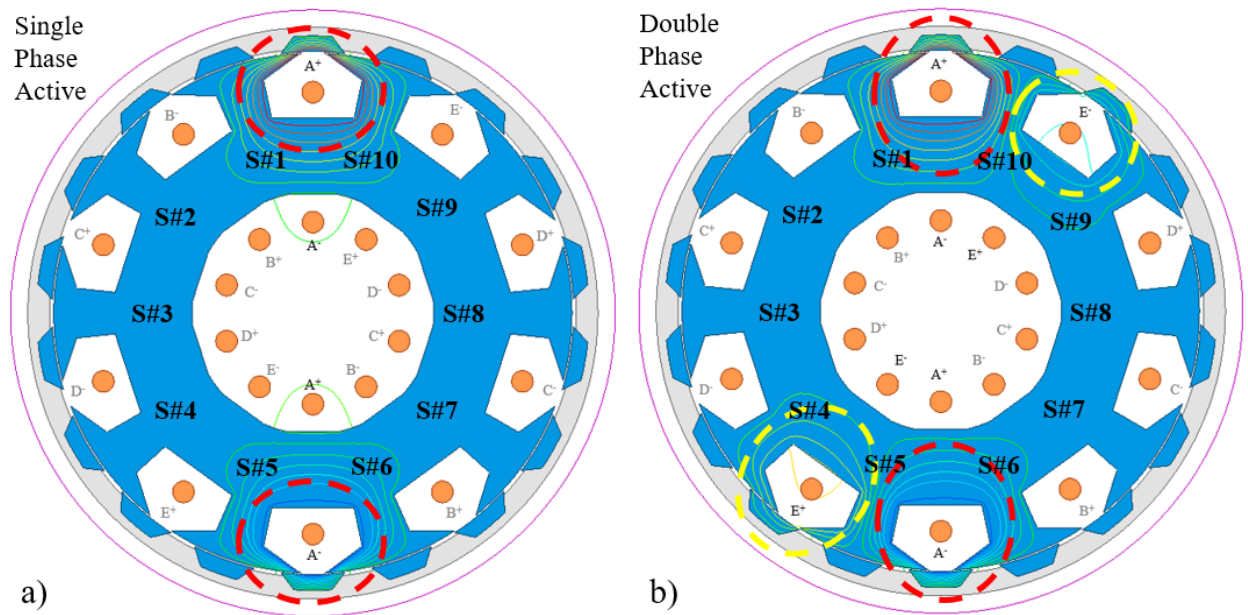


Figure 3.15: The 2D model of a 10/18 machine: a) single phase active b) stroke active.

CHAPTER 4

THE OPTIMIZATION METHOD

The design of the double-salient pole 3D flux 08/14 SRM could be done by a few trend studies because there could be a few criteria reduce the workloads:

- 1) Stator pole arc can be identical with the rotor pole arc
- 2) Rotor pole arc should be smaller than the stator slot opening to avoid overlaps between rotor poles and stator poles at unaligned position but needs to be as large as possible.
- 3) The stator size is defined by the axial rotor and radial rotor where the minimal thicknesses of rotor parts are defined by mechanical concerns.

The machine parameters of double salient-pole 3D flux SRM could be easily to find out, compared to those of segmented-rotor 3D flux SRM. In the segmented version, the axial stator pole arc and radial stator pole arc are allowed to be non-identical, which adds more flexibilities of exploiting the maximum output torque. On the other hand, it also brings more complexities to the optimization process. Compared to the straightforward trend study on the double salient-pole structure, the optimization method of the segmented-rotor structure should possess a few features: 1) iterative operations 2) parameter revision with somehow randomness 3) nonlinearity 4) global searching. The iteration of the optimization is a mandatory since the optimization itself is a methodology of searching for the optimal combination of machine parameters. The randomness for each parameter revision is necessary since the optimization of machine dimension may not always align with human intuitions which are linear summation of existing outcomes. After all, we do not know what we do not know yet such that the randomness is critical for the learning curve. If the optimization process could be viewed as a multi-dimension

function, there could be local optimization points. Nearby the local optimization points, there could be some linearities. When the optimizer moves along such linearity, a local optimization point could be achieved. However, the local optimal solutions do not always mean the global optimal solutions and may not be practical either. This brings up the requirement of global searching. There could be three types of global searching algorithms with randomness: 1) Particle swarm optimization 2) Migrating bird optimization 3) Genetic Algorithm. Those algorithms could be viewed as the same type of algorithms which aim to solving knapsack problems in the high level. The Genetic Algorithm (GA) optimization has a concise logic flow and has been used for multiple machine design projects. The core logic of the GA optimization is to try out any possible mutations of the selectable parameters and meanwhile to keep the superior candidate combinations in the cross-over process. The good pieces of genetic sequences will be inherited through generations to generations. The fundamental operations of GA are shown in Figure 4.1. There are three types of operations of GA optimization, cross over, mutation, and elite inheritance. In every generation, the machine model will be simulated by the combinations of machine parameters. Those combinations of machine parameters can be interpreted as genes for the combinations of machine parameters to be simulated for the next round.

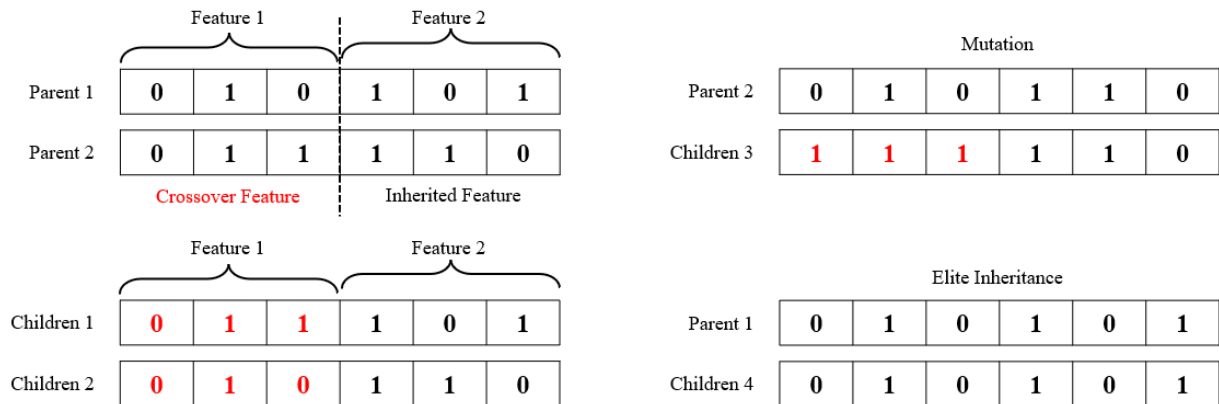


Figure 4.1: The fundamental operation of Genetic Algorithm (GA) Optimization.

The mathematical interpretation of each combination could be presented by a binary sequence of cascading binary pieces. Each piece contains certain numbers of binary values which quantize and discretize the according machine parameter. As the inheritances in the real world, not all gene pieces of parents could be inherited by offspring. Or the child may inherit gene pieces from both parents as illustrated by crossover operation in Figure 4.1. New gene pieces could be also obtained by mutation, which is a small probability event. The mutation is critical for creatures' evolution, which guarantees the diversity of species. The mutated genes could bring surprising benefits to species at some points. This is the randomness of GA optimization. To keep the evolutions on track, gene sequences of elite offspring have chances to directly pass to the next generations such that the offspring will possess the desired features verified in history. The percentages of crossover genes, mutated genes, and elite genes are selectable. Since the global optimization process could theoretically iterate forever, the conventional global optimization processes normally stop by two conditions: 1) boundary conditions are triggered 2) the maximum iterations have been reached. In a conventional optimization, the solving region could be a multi-dimension region with smooth and continuous surfaces while in the GA optimization, the solving region could be a multi-dimension discrete objective which may have many contents, but the number of discrete contents is finite. This could be due to the nature of the knapsack problem. As a result, there is no typical boundary conditions of the GA optimization, even though boundary conditions could be filled in the GA optimization toolbox as inequalities. However, those inequalities are mainly used for limiting the selection ranges of each machine parameters not for terminating the process. The operation principle of the GA optimization is simple: start the program till it reaches the maximum iterations or anywhere the users want to

stop the program. The behind logic of this is shown in Figure 4.2. As a conventional global searching algorithm, gradient descent algorithm gradually converges to the local or global optimal points as the number of iteration increases. In the GA optimization, optimal solutions could begin to appear from certain generation. As the number of generations builds up, the possibility of appearances of good solutions will increase since the offspring is sort of being forced to evolve for specified directions (remind the small portions of elite genes propagating through every generation). Thus, after certain number of generations, the optimal solution could be found in the database. And it has been observed that with a great number of iterations, the results of GA optimization could present a few major categories of gene sequences. In each category, the gene sequences of offspring could be similar but with small differences. The gene sequences of different categories could present huge discrepancies, for example, the segmented-rotor 08/14 SRM could at least present two categories. One category could have larger radial stator pole arcs, and the other one could have larger axial stator pole arcs. The physical meaning of those two categories is that either radial part or axial part of the machine dominates the final output torque.

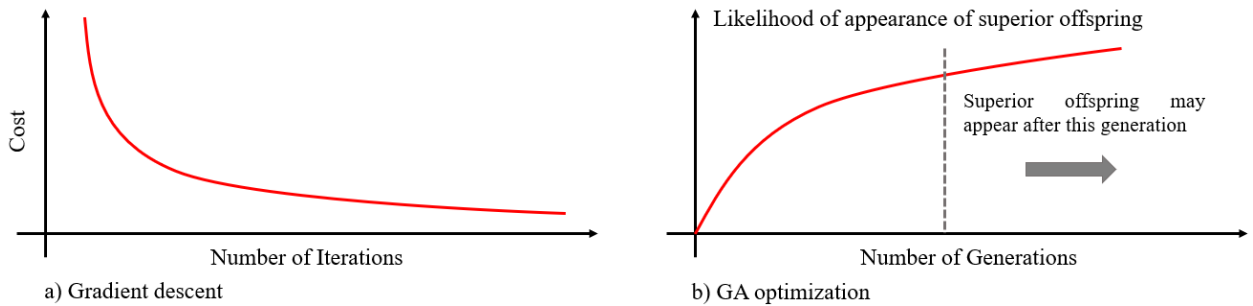


Figure 4.2: The behind logics of different optimizations.

The model is built by at least 60 machine parameters. Assuming that the binary interpretation of the selecting range of every machine parameter is a 4-bit data, the total combinations of gene

sequences will be 16^{60} which is about $1.76e72$. Even though optimal solutions may appear after 50th generation, the number of 3D FEA simulation may be overwhelming (noting that every stroke-based 3D FEA may cost 16-to-24 hours on a 16-core 128MB memory working station). As a result, the number of considered machine parameters must be reduced to a reasonable range to minimize the workload. Otherwise, the GA optimization will run forever. In the segmented-rotor SRM, the interior stator and flux tubes are built from at least 30 machine parameters due to the necessary complexity. For accommodating different MMF and radial and axial stator pole arc, the geometries of the interior stator and flux tubes will be required to change. In a constraint space, the maximum MMF per phase may be roughly found out by examining saturation patterns of the stator core. The according geometries of stator pole bases and flux tubes can be pre-fixed to match the maximum MMF per phase. The axial stator pole arc, the radial stator pole arc, the radial stator pole tip, and axial stator pole tip can be flexibly revised without changing the stator pole bases and flux tubes. This makes the GA optimization of the interior stator machine design possible. The evaluation criteria, the cost function of the optimization could contain two terms, the average torque and torque ripple. More precisely, the two terms are the inversed square of average torque and the inversed square of torque ripples, respectively. This is because the main logic of the GA optimization tends to evolve the gene sequence along the trend of minimizing the cost function. The cost function is a multi-input and single-output function where all simulated parameters will be recorded. The single output is just for simplify the evolution direction which ideally emphasizes both the average torque and torque ripples with the according weights. In fact, the average torque will be the top objective of this study while the torque ripple is a secondary objective. The data base of the GA optimization could be accessed at any time of

the co-simulation between MATLAB and 3D FEA package. It is always possible to find out the most optimal solution in the data base. As discussed above, the optimal gene sequences may converge to a few categories after certain number of generations as shown in Figure 4.2. Python scripts could be helpful to statistically analyze the total database and find out the superior solutions. The final drawings of the 10/18 model are derived from one of the superior solutions where the drawings are modified by fabrication concerns. In Figure 4.3, the simplified gene sequence consists of the axial rotor pole arc, the radial rotor pole arc, the axial stator pole arc, the radial stator pole arc, and the additional radial stator pole length. The rest of machine parameters are pre-fixed given the results of previous rounds of GA optimization. The purpose of this simplified GA optimization is to find quick geometrical answer since there are more workload to make the model easier for CNC milling, EDM, and wire cutting. Most of machine parameters are rounded with one or two decimal numbers per manufacture concerns so do the tight tolerances in the model.

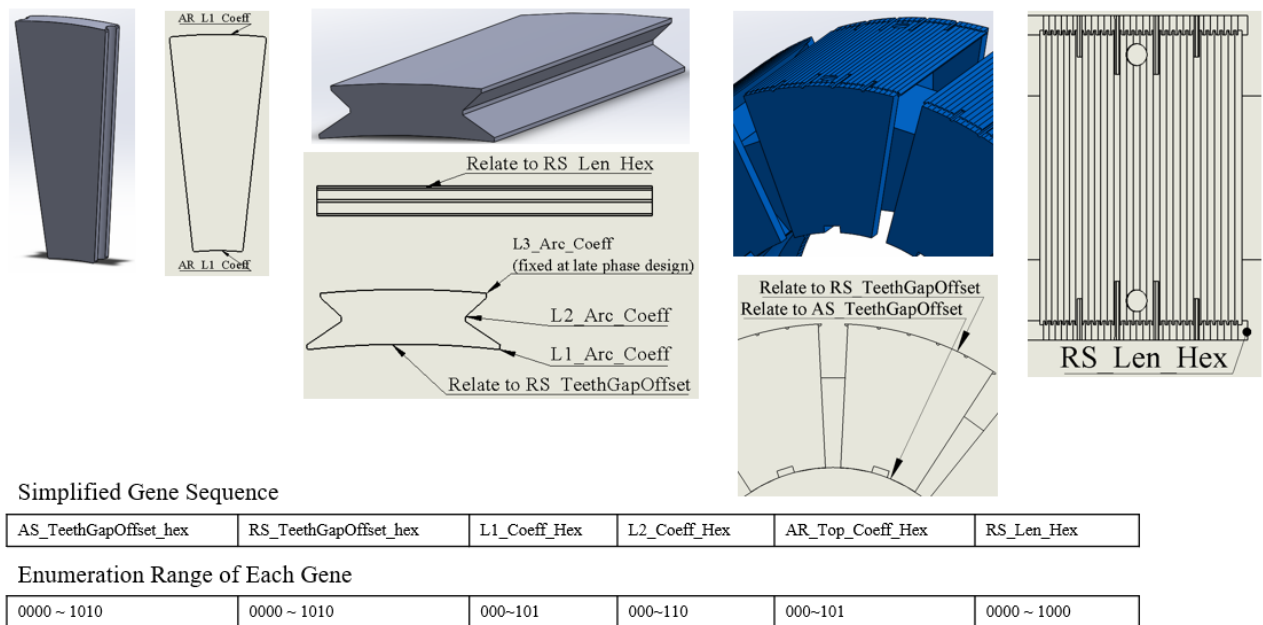


Figure 4.3: The simplified gene sequence.

The whole design process could be summarized as shown in Figure 4.4. The GA optimization could be treated as the inner loop of the whole design process after narrowing down the design scope. The first thing is to lock down the parameter of the OD and ID of the rotor frame. Given the magnetostatic simulation, it is found that the 6-mm thickness of magnetic rotor segment could be the threshold value. No significant benefits can be obtained by increasing the thickness of the rotor segment over 6mm while the decreases in average torque can be observed once the thickness is smaller than 6mm. The radial airgap and axial airgap are both 0.4mm such that the OD of the stator can be locked. After a few simulations on the thickness of axial rotor segment, the total length of the interior stator could be solved. The ID of the stator can be solved after the maximum MMF per phase is choice because the ID of the stator determines if the hallow inner space of the interior stator is sufficient to house the 5-phase end windings. The increases in ID of the interior stator lead the depth of stator slots to increase or lead the number of turns of windings to reduce. After multiple trials, a balanced point could be found out. And the internal GA optimization could start from there. In Figure 4.4, it is shown that the machine design is based on the 10/18 model under a 2.55 Liter space restriction. In fact, this design flow could be applied to other space restriction and pole configurations. Given the magnetic field analysis above, the 10/18 pole configuration may be the only feasible option for space smaller than 2.55 Liters. If the space constraint is released, the numbers of stator poles and rotor segments could be increased by integer times. Considering the potential down scaling of the 10/18 model per budget concerns, the GA optimization processes are directly duplicated for a small volume 10/18 segmented-rotor 3D flux machine.

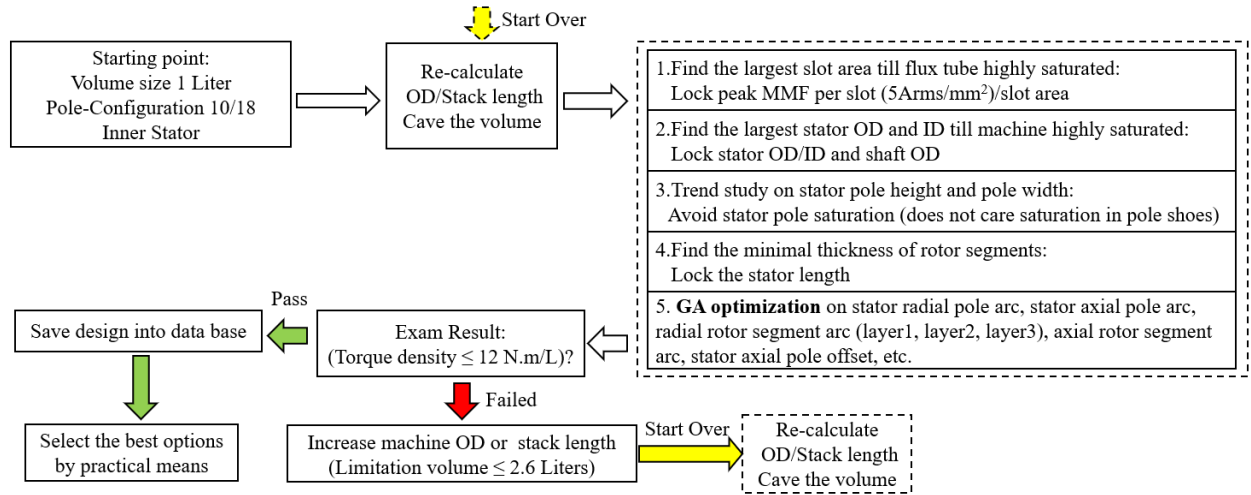


Figure 4.4: The logic flow of the overall design process.

In the next chapter, the simulation results and geometric down-scaling of the 10/18 will be discussed.

CHAPTER 5

SIMULATION RESULTS

Before the down-scale prototype is fabricated, the according 3D model is simulated. As the previous chapters emphasize, a few criteria are to be satisfied: average static torque, circuit dynamic, structure deformation, thermal stress. After multiple GA optimizations, the geometric configuration of 1-Liter down-scaled models is selected. The tradeoff process is based on the above criteria. Since the model is proposed for the signature of high average torque density. The average static torque has the top priority. To be critical for the design, static torque profiles are evaluated by multiple perspectives. Due to the nature of 3D FEA simulations, the reliability of static torque profile is based on the 3D meshes and their qualities. Plus, the mesh leakage issues occur in the entire development process. If mesh leakage occurs, the band, the solving region, the resolution of the model will be needed to reasonably modify to successful solving. The according data point may loss a bit consistence to other data point solved before the solving region is modified. In addition, the estimated static torque is based on a consumption where the excitations are constant. The practical excitation may be faced with current ripples and electrical transient such that the high static torque at the certain rotor positions may not be easily obtained in practices. In the down-scaled model, the current density is set to 5A/mm^2 for the cooling concerns. Given the superior magnetic properties of the Hiperco 50, the current density of 5A/mm^2 may not be able to properly saturate the down-scaled machine. To maximally utilize the 1-Liter magnetic core, the current density is better to be greater than 6.4A/mm^2 while it is not necessary to do that in the trimmed prototype. The model running with 5A/mm^2 can show a high torque density about 8N.m/L which is sufficient to validate the idea. A few superior static stroke

torque profiles from GA optimization are demonstrated in Figure 5.1. Each torque profiles are labeled by series numbers where those numbers denote the optimization parameters. The GA optimization of the down-scaled model adopts four optimizing variables: radial rotor pole arc coefficient, axial rotor pole arc coefficient, stator slot opening coefficient, and gap coefficient of stator radial pole and stator axial pole. Each variable has 16 discrete selections for reducing the computation burdens. All static torque profiles show small instant torques at the end of stroke. The model 831010 and model 46811 show the highest instant torques at the end of stroke. In fact, SRMs are normally faced with a conundrum: at one hand, the higher torque at end of strokes can greatly reduce the torque pulsation and boost the average torque; at the other hand, one phase is expected to be immediately turned off after the end of stroke which is impossible in the real world. There will be some tailing current which may result in partial negative torque such that the commuted phases are normally turned off at the end of stroke o. The high torque at end of strokes may not be fully utilized in real world. So, the model 831010 and model 46811 are out of Table

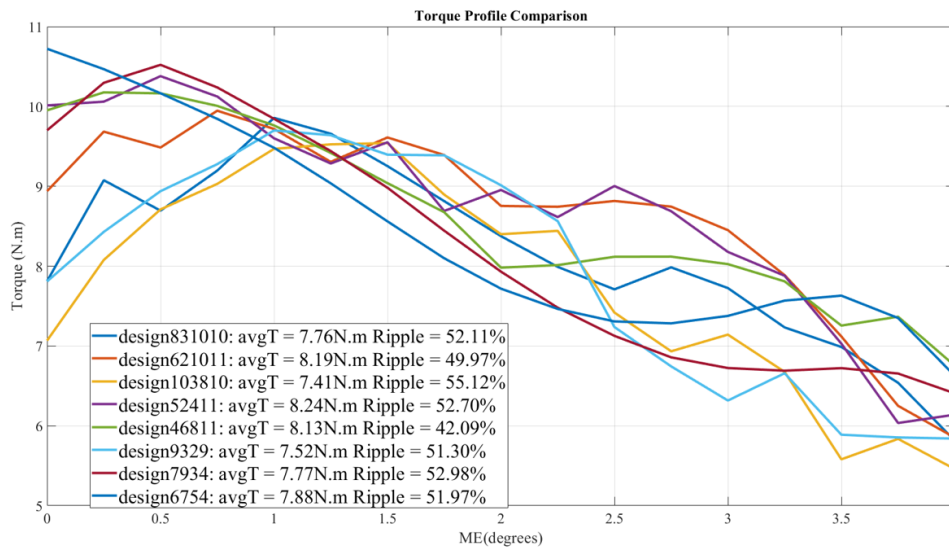


Figure 5.1: The static stroke torque profiles of GA optimized down-scaled models.

The model 52411 show the best stroke but its solving region and band were modified a few times due to the mesh leakage issues. There is, of course, a question mark of integrity of the data such that the model 52411 was abandoned. With more evaluations, there are only model 621011 and model 6754 remaining on the Table The model 621011 has a bit higher average torque. Also, its profile looks more even in the stroke period. As a result, the model 621011 was decided to fabricate and co-simulate. In the following section, the simulated electrical dynamics, structural performance, and thermal performance are demonstrated.

5.1 The simulated electromagnetic behavior of the model 621011

The simulated material is Hiperco 50. The according data of B-H curve and core loss curve are purchased from the MagWeb database. Those data only describe Hiperco 50 27mil lamination. As mentioned in the previous chapter, not many vendors really investigate the magnetic performance of Hiperco 50 solid block. Thus, the simulation results are only used to demonstrate the principal machine behavior. The magnetic data and loss data are shown in Figure 5.2. The mechanical properties are shown in Figure 5.3.

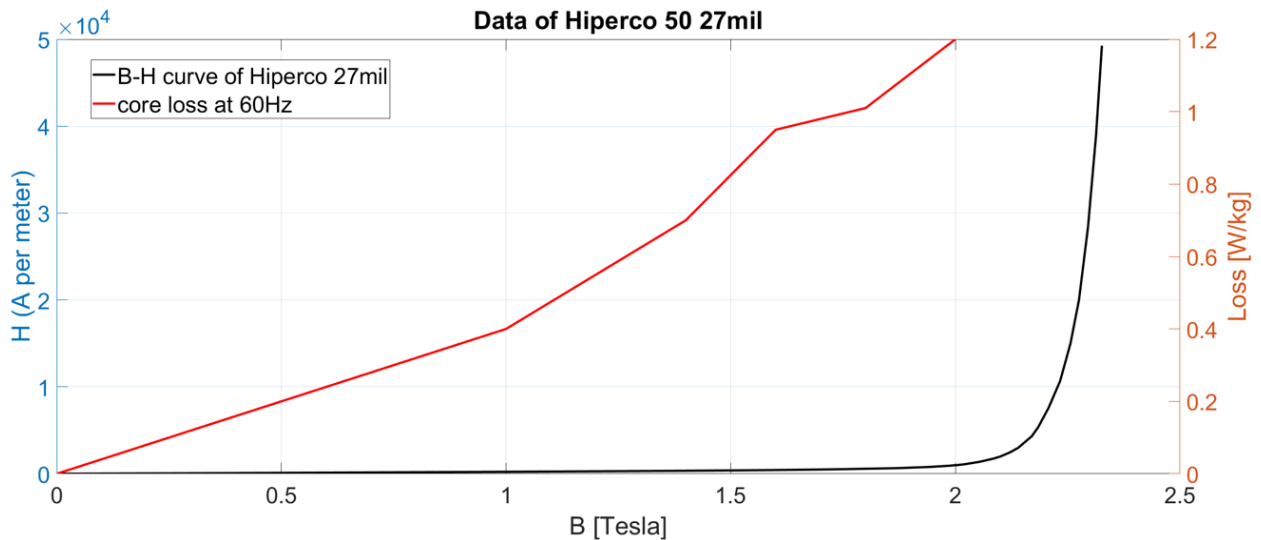


Figure 5.2: The B-H curve and loss curve of Hiperco 50 27mil.

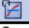

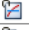

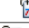



Properties of Outline Row 5: Hiperco50			
	A	B	C
1	Property	Value	Unit
2	 Material Field Variables	 Table	
3	 Density	8120	kg m ⁻³
4	 Isotropic Secant Coefficient of Thermal Expansion		
5	 Coefficient of Thermal Expansion	1.04E-05	C ⁻¹
6	 Isotropic Elasticity		
7	Derive from	Young's Modulus and Poisson...	
8	Young's Modulus	2.07E+11	Pa
9	Poisson's Ratio	0.33	
10	Bulk Modulus	2.0294E+11	Pa
11	Shear Modulus	7.782E+10	Pa
12	 Tensile Yield Strength	7.17E+08	Pa
13	 Compressive Yield Strength	3.65E+08	Pa

Figure 5.3: Mechanical properties of Hiperco50 27mil.

The magnetostatic solver can apply automatic refined mesh during the iterative process and provide accurate torque results. The evaluations of torque density are based on the magnetostatic results. In the co-simulations between TwinBuilder and 3D FEA transient solver, there is no automatic mesh such that the element size could be larger than their proper size. The quality of co-simulated torque decreases with the simulation steps while the results are able to evaluate the machine behaviors. The TwinBuilder circuit is shown in Figure5.4. The circuit simulates a 5-phase asymmetric bridge rated up to 20A per phase. The co-simulation step-size is set to 20us, corresponding to the 50kHz control frequency. The machine model is simulated at 180 rpm. The control method is current-based hysteresis control with 0.6A band. The electrical cycle of the model has a duration of 20 mechanical degrees. Each phase actives for consecutive 8 degrees. The first 50% duty overlaps with the outgoing phase. The last 50% duty overlaps with the incoming phase. The excitation sequence is as follows: Phase E and Phase D → Phase D and Phase C → Phase C and Phase B → Phase B and Phase A → Phase A and Phase E. The simulated excitation sequence is also shown in Figure 5.5. The current band become larger and larger due to decreasing quality of the meshes. However, the current transient and commutation

can be validated by this simulation. The commutation was seriously concerned in past due to the combination of toroidal windings configuration and inner stator. Due to the degraded mesh quality, the torque and core-loss data are only shown by the reasonable window which includes second and third strokes as shown in Figure 5.6 and Figure 5.7. The raw co-simulated inductance profile has many ripples which is due to the variations of mesh quality and chopping. The data are applied with the moving average filtering to smooth the curve. The phase C inductance profile has a saliency ratio of 171% under rated excitation ($5\text{A}/\text{mm}^2$) as shown in Figure 5.8. It could be seen that the inaccuracy of the co-simulation at aligned position could be due to the advanced turn off. To avoid consuming too much storage space of system hard drive, the field information and mesh information are only stored every 700us. The core loss profile has a low resolution while it is sufficient to estimate the average core losses. Since the machine operates at a lower rpm, the core loss is smaller than copper loss. At the low-speed region, the copper loss will dominate the total loss.

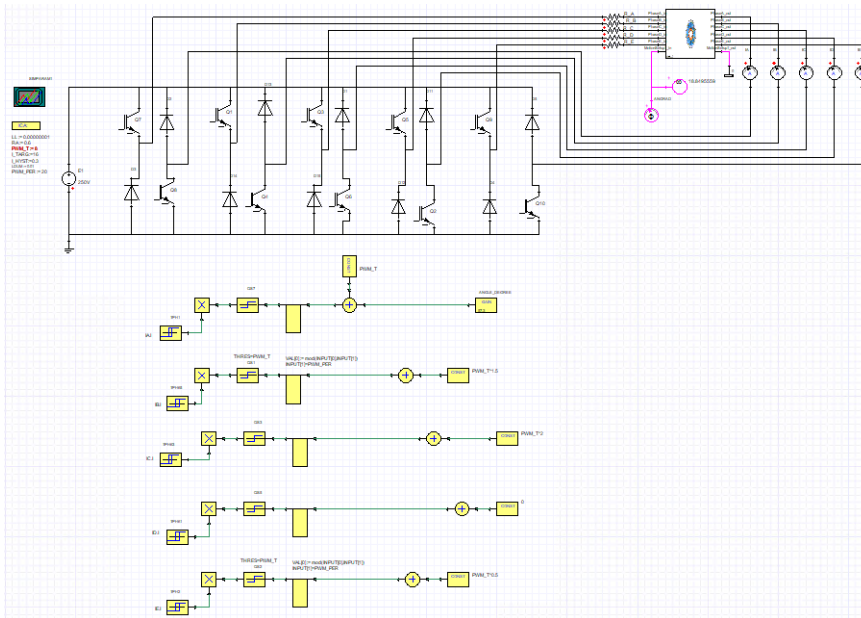


Figure 5.4: The co-simulation electrical interface.

To provide more insight of the model, the major machine parameters are summarized in the Table 5.1. The structure is quite complicated such that the small dimensions are not presented in the thesis. In addition, the small dimension parameters may be slightly changed to improve the feasibility of fabrication. The geometries of rotor segments and stator poles could refer to Figure 4.3.

Table 5.1: The machine parameters of the down-scale 10/18 model 621011

Items	10/18 Model	Items	10/18 Model
Radial Rotor Segment Arc 1 st Layer (°)	14.6	Phase Number	5
Radial Rotor Segment Arc 2 nd Layer (°)	7.6	Turns Number per phase	252
Radial Rotor Segment Arc 3 rd Layer (°)	10.6	Branch per phase	2
Radial Rotor Segment Length (mm)	55.2	Phase Resistance per phase(ohm)	0.6
Radial Rotor Segment Outer Radius (mm)	70mm	Peak Phase Current (A)	15.8
Radial Rotor Segment Outer Radius (mm)	66mm	Average Torque (N.m)	8.19
Axial Rotor Segment Arc 1 st Layer (°)	11.9	Overall Volume (Liters)	1
Axial Rotor Segment Arc 2 nd Layer (°)	10	Torque Density (N.m/L)	8.19
Axial Rotor Segment Arc 3 rd Layer (°)	11.9	Torque Ripple (%)	50%
Axial Rotor Segment Length (mm)	4	Copper Loss at rated condition	75
Machine OD (mm)	140		
Machine length (mm)	70		
Stator Inner Radius (mm)	37.4		
Stator Outer Radius (mm)	65.6		
Stator Length (mm)	61.2		
Stator Radial Pole Arc (°)	31.2		
Stator Axial Pole Arc (°)	31.2		
Stator Axial Pole Thickness (mm)	3		
Radial Stator Slot Area (mm ²)	276		
Axial Stator Slot Area (mm ²)	276		
Filling Factor (%)	50		
Radial Airgap (mm)	0.4		
Axial Airgap (mm)	0.4		

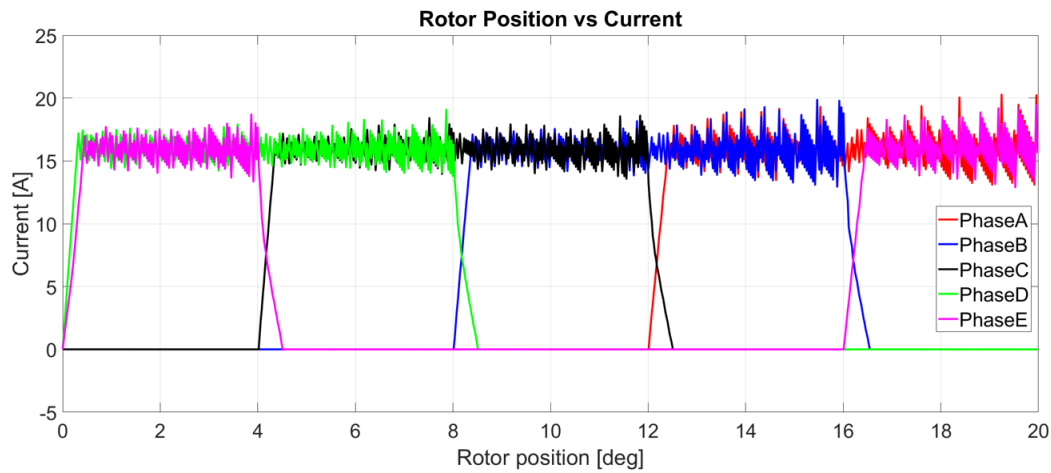


Figure 5.5: The simulated excitation sequence.

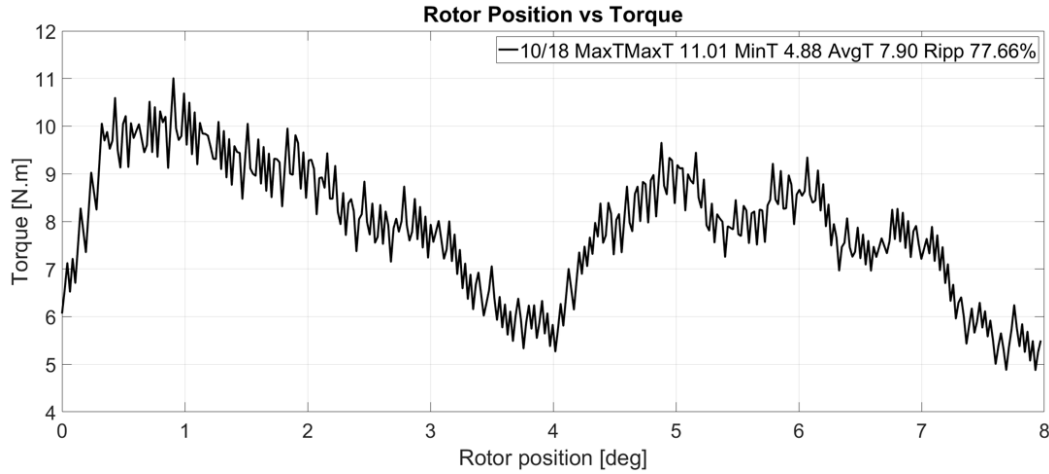


Figure 5.6: The co-simulated torque profile of the second and third strokes.

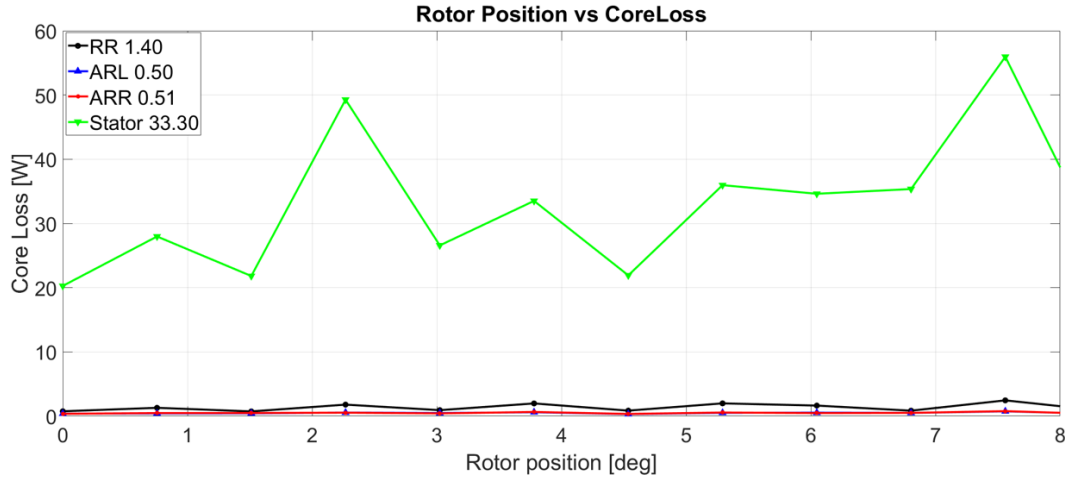


Figure 5.7: The co-simulated core loss profile of the second and third strokes.

For the down-scale 1 Liter model, 5A/mm^2 is not sufficient to saturate the Hiperco 50 core. This could be quickly verified by three flux plots at the aligned position. The flux plots of the center of stator, 0.1mm underneath the stator axial pole, and 0.1mm underneath the axial rotor segments are captured and are shown in Figure 5.9. The overall flux density is below 2.0 Tesla. The conners of radial segments and radial stator poles shows around 2.2 Tesla while the flux density of stator pole and flux tubes are around 1.6 Tesla to 1.8 Tesla. The axial stator pole surface shows 2.0 Tesla at regions overlapped with edges of axial rotor segments. The flux densities of

other regions are equal or less than 2.0Tesla. The axial rotor segments are clearly under unsaturated condition. Those proves that the machine core cannot be fully exploited under 5A/mm^2 .

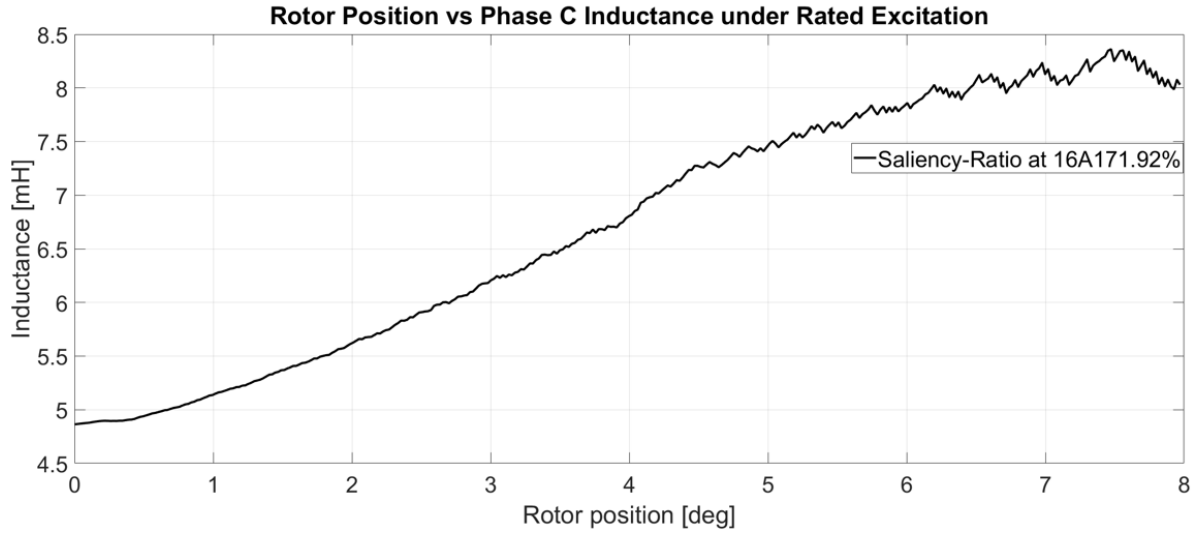


Figure 5.8 The phase C inductance profile from the unaligned position to the aligned position.

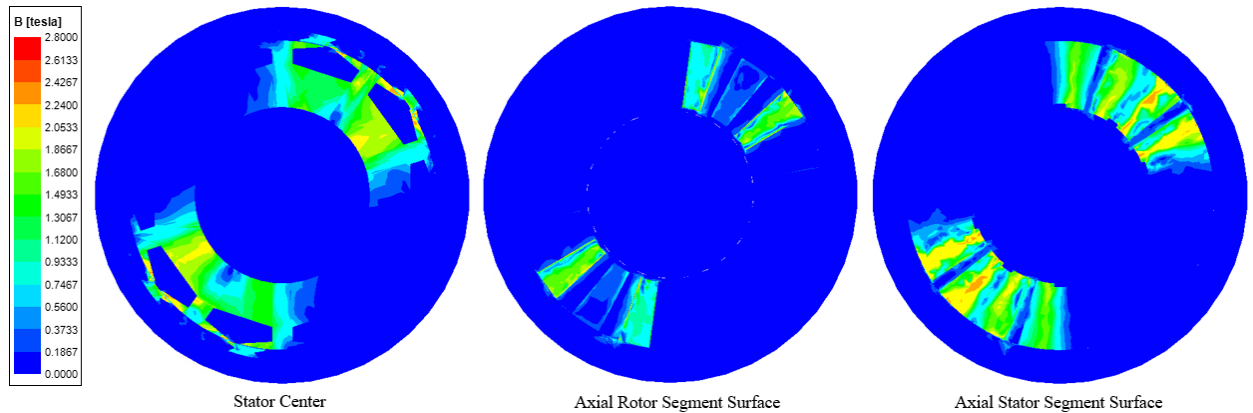


Figure 5.9: The flux plots of stator center, axial stator pole surface, axial rotor segment surface.

5.2 The simulated mechanical and thermal performance of the model 6211011

The structural pressure and deformation simulations are based on the peak aligned position field information. The data of surface force density of the model at aligned position are imported to the steady-state structural analysis. The simulation time is set to 1000s which is enough to

achieve the steady state. Since the machine is an exterior rotor machine, the machine is designed to be supported from one side. The torque is transmitted through the rotor frame. The major support components include two stator support, the stationary shaft, bearings, etc. Since the electromagnetic simulation with separated support components cannot be solved due to mesh leakage issues, those are merged into one piece. The actual stator support frame has multiple vents allowing air flow or oil flow. Those vents crash the electromagnetic simulation as well such that the bores are removed from the support frame. From the deformation standing point, the major concerns are not on the rotor frame since the geometry has decent materials. They are on edges of the rotor segments and stator poles which interact with large electromagnetic forces. In addition, the deformation is expected not to significantly impact on the radial and axial airgap. The rotor frame is designed to fully housing the rotor segments. High temperature super glue will be used to install the rotor segments even though the snug fitting tolerances of rotor frame has been applied. The rotor segments cannot freely move once the rotor segments are inserted into the slots of rotor frame. Thus, the electromagnetic force acting on rotor segments will be partially distributed to the rotor frame. To simplify the simulation, the contact between edges of rotor segments and slots of rotor frame are set to direct contact. To show both inside and outside of the machine, the graphs are captured from the center cross-section plane. The deformations and maximum stress information of rotor are shown in Figure 5.10 and Figure 5.11. The maximum deformation of the rotor is 1.566×10^{-4} mm where the rotor frame is built by Aluminum 6061T. The maximum stress is 0.505 Mpa. A few spots of contact regions of rotor segments and slots of rotor frame show stress around 0.449 Mpa.

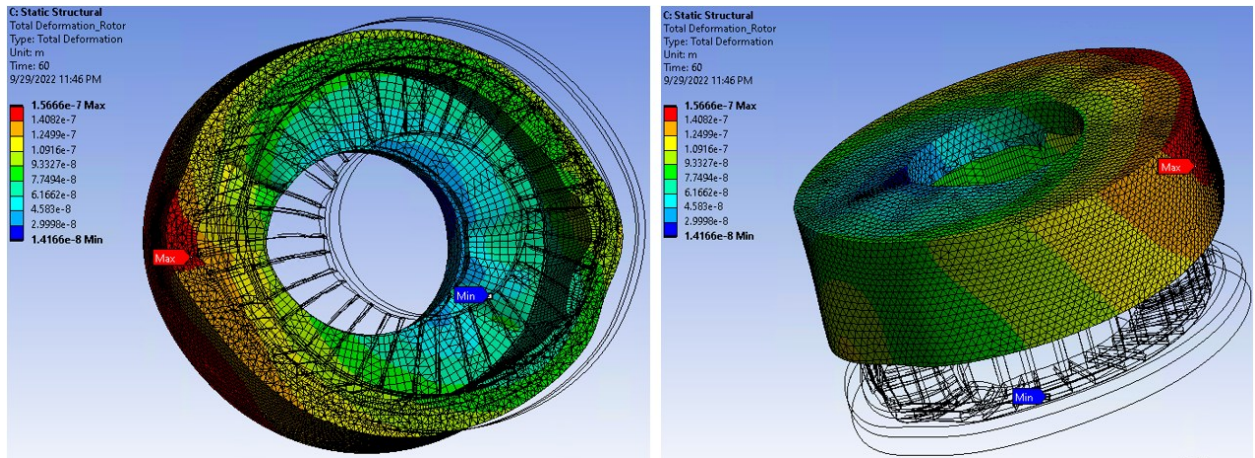


Figure 5.10: The deformation information of rotor.

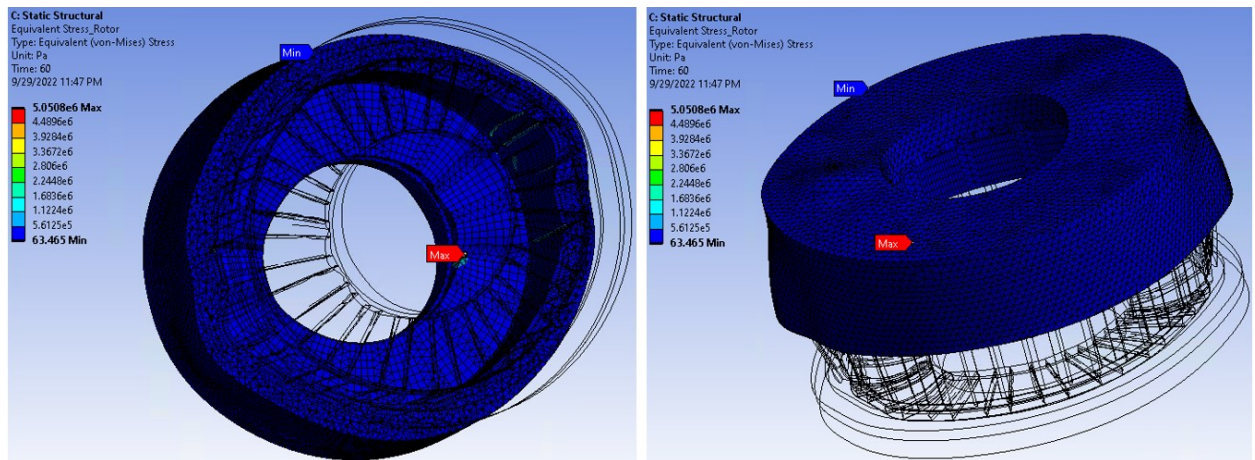


Figure 5.11: The stress information of rotor.

The deformation of interior stator is presented in Figure 5.12 while the stress information is presented in Figure 5.13. The maximum deformation is 3.4808×10^{-4} mm at the edges of stator radial pole. At the aligned position, one phase is fully aligned. The other phase is at the half-aligned position. For the half-aligned phase, the according rotor segments just begin to overlap the stator pole shoes. The great deal of electromagnetic force locally distributes on the overlapped thin stator pole tips. However, the level of deformation is too small to be concerned. The pressures on edges of stator pole tips are around 9.1 Mpa to 4.6 Mpa, which do not draw attention.

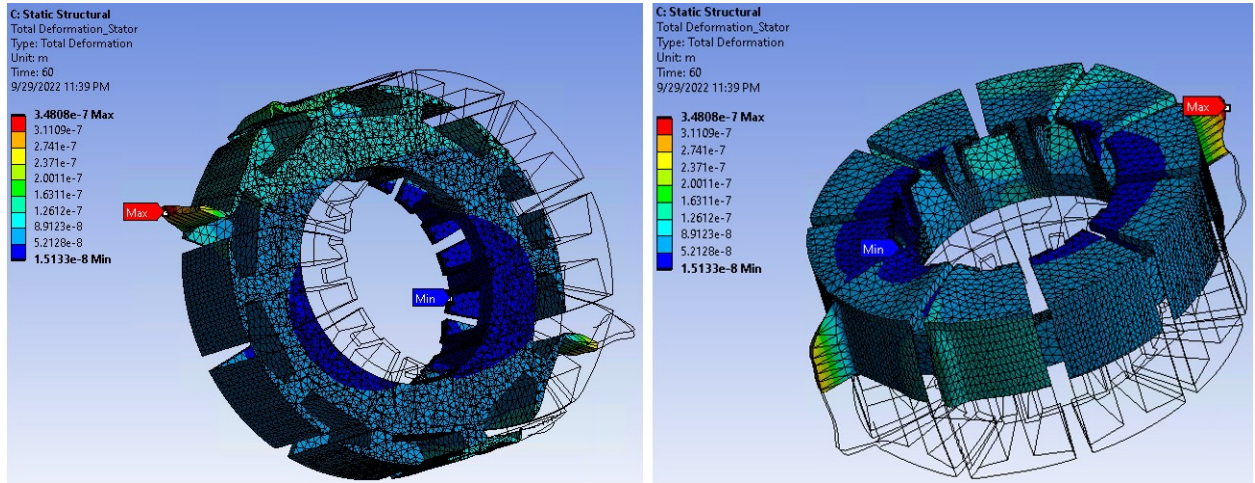


Figure 5.12: Deformation information of the stator.

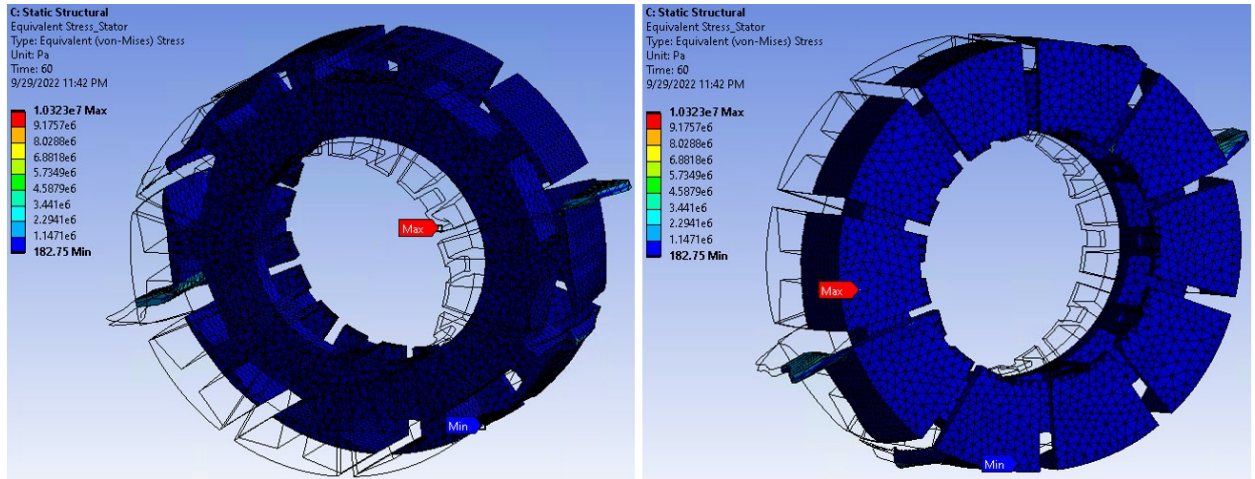


Figure 5.13: Stress information of the stator.

All support components are made by non-magnetic stainless steel 316. They only support the static weight. Since the motor is only supported from one side, the unmounted side shows more stress and deformation than the other side. The maximum stress is about 10 MPa. The according deformation is about 1.06×10^{-4} mm as shown in Figure 5.14.

The steady-state thermal performance of the machine is simulated. The major heat source is from the windings. The DC copper loss is about 75 W. The copper loss due to the AC resistance is hard to know because the actual geometry and configuration of the real 3D windings are not easy to

know. Plus, the machine is designed to operate at low speed such that the AC resistance is just ignored for simplicity. The copper loss is partially coupled to the stator and the support unit. Since the vents are absent from the support unit, a small region of the mounting side is set to $20\text{W/m}^2\cdot\text{C}$ to mimic better cooling effect. The actual cooling effect could be better or worse than this number. The inside surfaces of rotor, stator, and support frame is set to $10\text{W/m}^2\cdot\text{C}$ to mimic standard air convection. Even though the outer surfaces of rotor directly contact with air and has a better cooling effect, the rotor temperature is low. Partial heat from stator couples to the rotor frame, while the temperature of the rotor frame is still much lower than stator as shown in Figure 5.15. The hottest spots of the rotor are closed to the unmounted side since the cooling factor is low. The average temperature of rotor segments and rotor frame is around 44C . The peak temperature of rotor segments and rotor frame are around 52C . The rotor segment temperature plots are shown in Figure 5.16. The rotor segments closed to the mounted side show a lower temperature at 44C due to the better cooling effect.

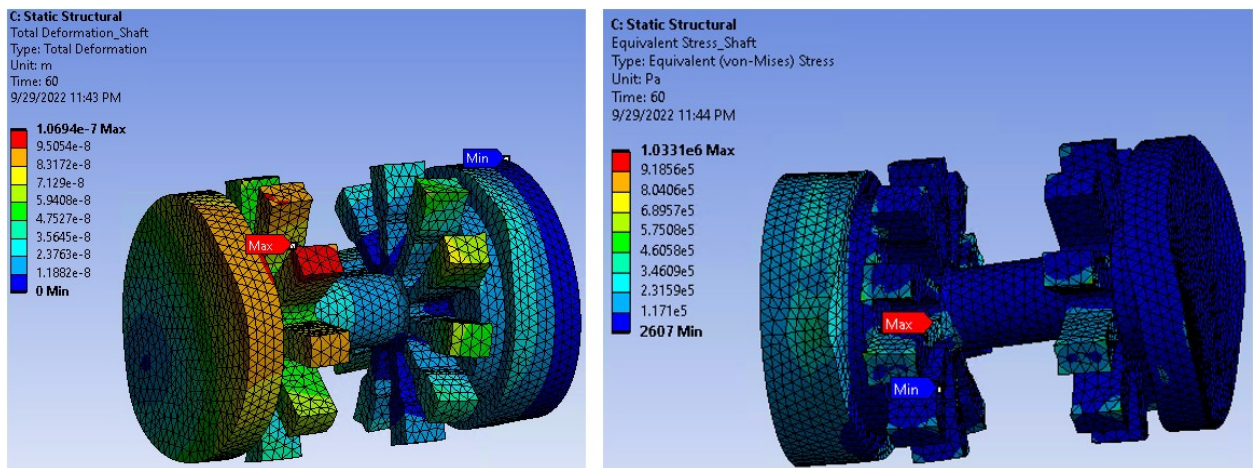


Figure 5.14: The stress and deformation information of the support unit.

There is decent winding heat coupled to the stator, the average stator temperature is around 86C as shown in Figure 5.17. The peak temperature inside of the inner stator is high as 89C . Since the

stator support frame direct contact with the interior stator, the heat from stator is partially coupled to the support unit. The support beams of one side with the better cooling condition show a peak temperature of 84.5C. The other side is about 89.5C. The average temperature of the shaft is about 69C.

In the next chapter, the down-scaled prototype will be demonstrated including the test setup and electronic interface. The test results and analysis will be presented.

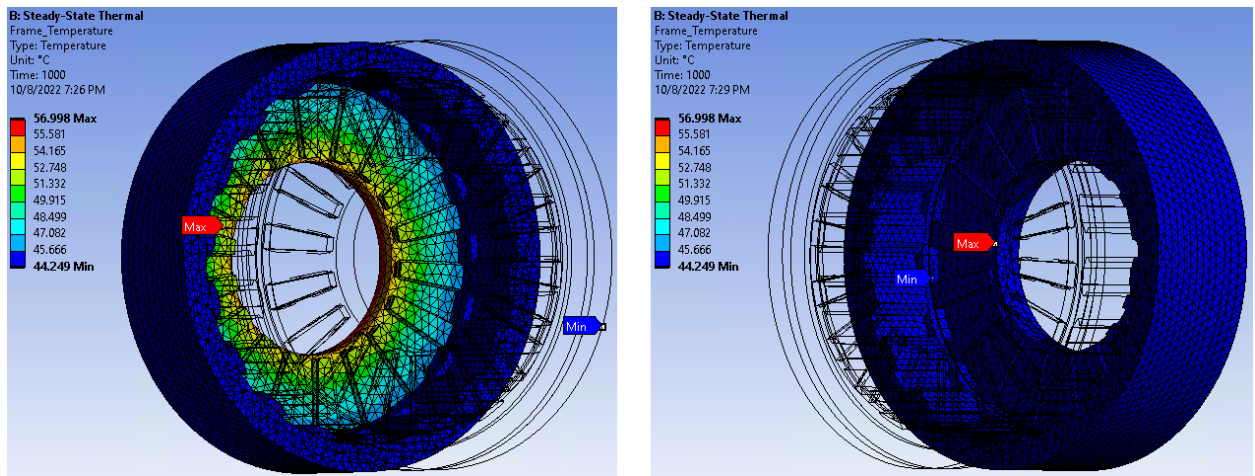


Figure 5.15: The inner temperature of rotor frame.

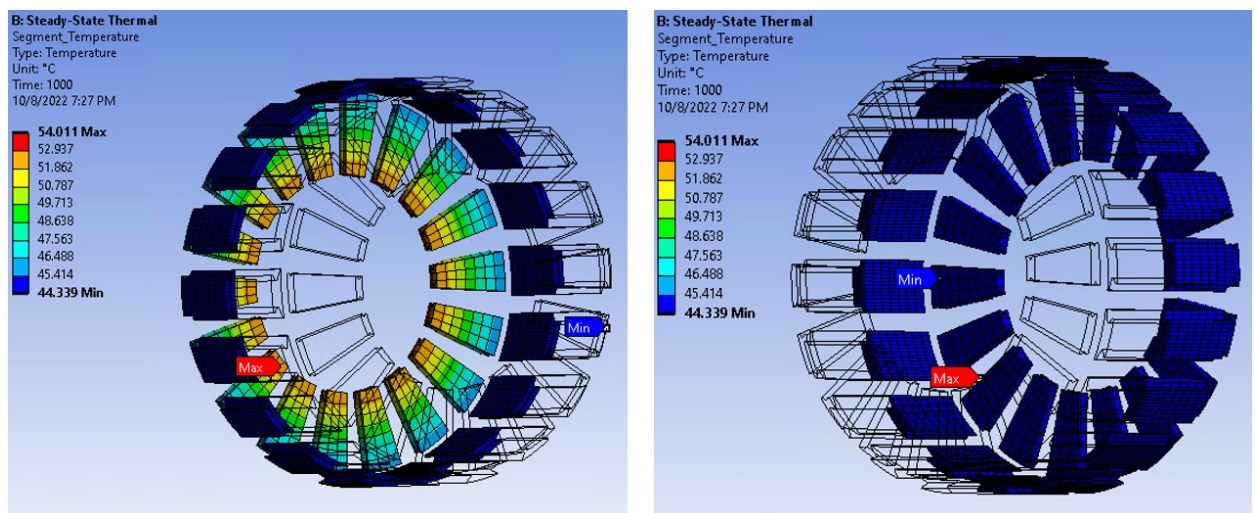


Figure 5.16: The temperature of rotor segments.

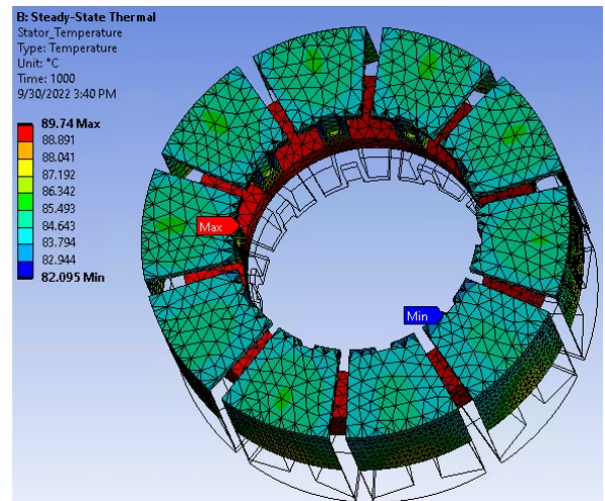
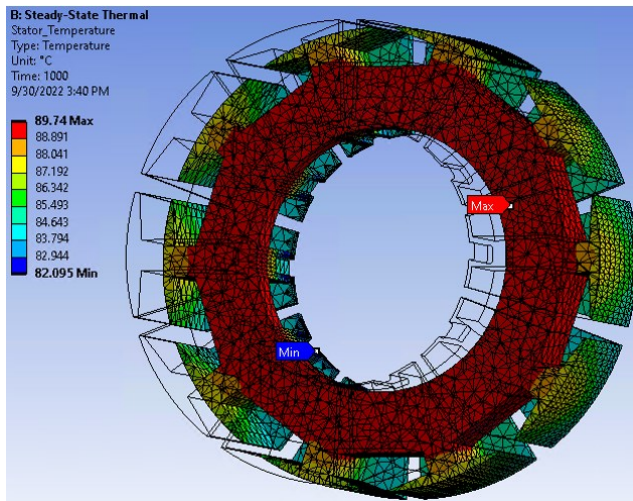


Figure 5.17: The temperature of stator core.

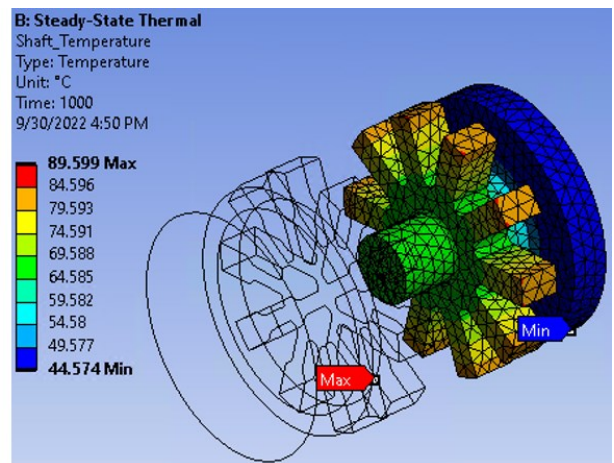
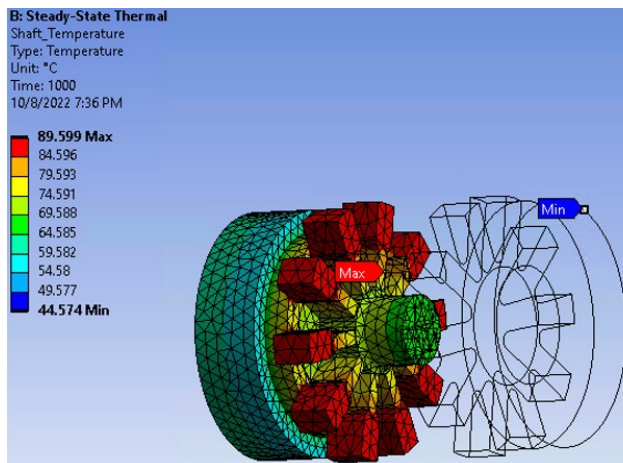


Figure 5.18: The temperature of support unit.

CHAPTER 6

EXPERIMENTAL RESULTS

To validate the design concept, a scaled-down prototype is fabricated. Originally, all parameters are selected upon the superior magnetic properties of Hiperco 50. However, per feedback from the vendor, the Hiperco 50 was stiff and fragile for their machinery such that the corners and edges may fall off at the end of machining. Considering the limited budget, lead time, and further assembly, the magnetic material had to be changed. The alternative material is equivalent to M19/BA35A250 electrical steel which normally offers a saturation point from 1.3 Tesla to 1.5 Tesla. Given the past simulations, the M19 could offer around 5N.m to 6N.m for the 1 Liter optimized geometry. Since there was not sufficient time to run all optimization again, the 1-Liter design is just manufactured by the alternative material without any changes. The purpose of this prototyping is to validate the magnetic configuration and to observe the impact of different core materials. From the material vendor, the purchased alternative material has the similar feature of BA35A250 while it is hard to confirm since the bulk material is not directly purchased from BAO STEEL. Fortunately, after all of fabrication and manual assembly, the final prototype indeed proves the design concept. A 5-phase SiC asymmetric inverter rated for 20A per phase has been developed. To improve the performance of the inverter, the high-band width differential isolated amplifiers are used for current sensing. The microprocessor is a high-end TI C2000 series dual core MCU, F28388D. The SiC MOSFETs and SiC Diode are 650V-40A discrete devices from Infineon. To improve the performance of the driver circuit, all driver circuits have their own isolated power supplies. The gating signals are directly fed into the power device with real short header pins around 7mm. The driver circuit is shown in Figure 6.1.

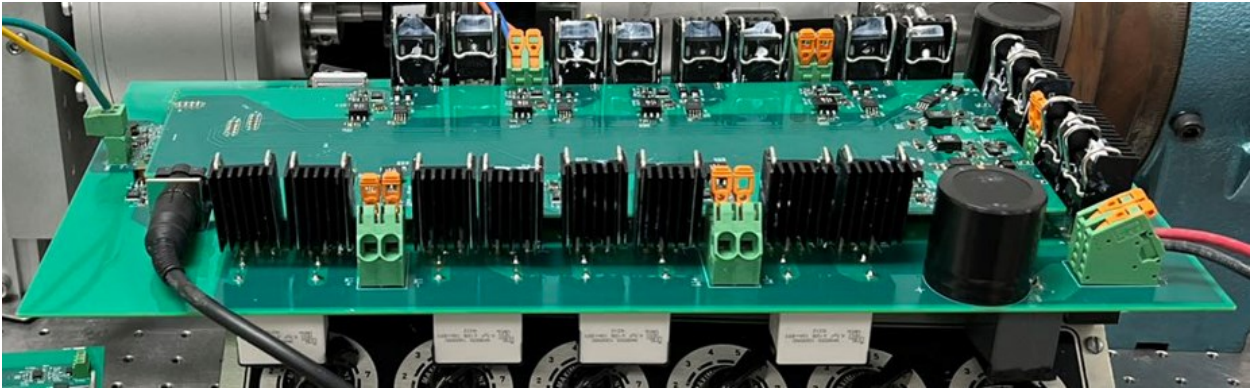


Figure 6.1: The 5-phase SiC asymmetric inverter board.

The winding installation is the hard part of the assembly due to the specified stator slot design. The windings have to be manually installed since there is no feasible commercial winding machine designed for the toroidal stator slots. The windings are made in the laboratory. Theoretically there should be 140 turns per stator slots while the maximum number of turns that can be safely installed is 39 turns per stator slot after many trials. The gap between each turn is quite large and the space is not properly exploited due to the lack of skills in winding installation. However, 39 turns per stator slot can still be useful to validate the design. The stator core with installed winding and support unit is shown in Figure 6.2. The rotor frame with installed rotor segments is shown in Figure 6.3. There are rust on magnetic core surface due to the lack of antioxidant treatment after the fabrication. After the magnetic parts are fabricated, there was a chance to apply antioxidant treatment on the core surface. However, there were two concerns: the additional treatment may increase the thickness of the magnetic parts and bring difficulties to assembly; the additional chemical treatment may change the magnetic properties. The surface regions of the magnetic core are important areas for harvesting torque. Due to the lack of treatment knowledge and experience, it is decided not to apply any additional treatment to those magnetic parts.

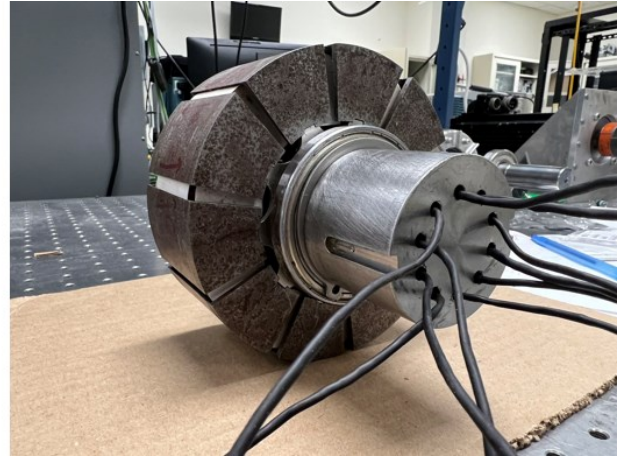
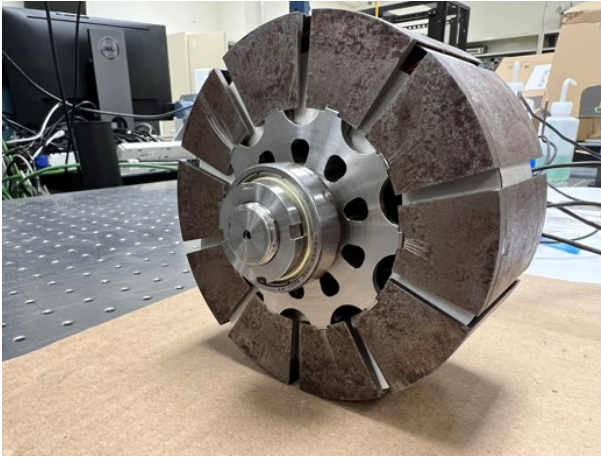


Figure 6.2: The stator with installed windings and support unit.

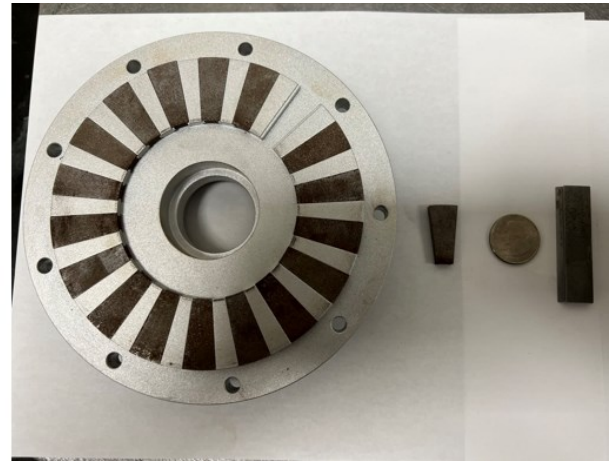


Figure 6.3: The rotor with installed rotor segments.

6.1 *Experimental results*

After the machine is fully assembled, static torque and inductance profiles are measured. The no-load dynamic performance is implemented as well. To measure the static torque and inductance profiles, the machine is installed in a static torque testbed where the shaft is clamped by the position rotary indexer as shown in Figure 6.4. The torque meter is MCRT 48001V (1-2)-N-N-N rated for 15000 rpm and 11.298 N.m. The torque meter generates $\pm 5V$ signal with a conversion rate of 2.26 N.m/V. A power inductor bank offering 2mH per phase is not shown in the picture due to its large size. The power resistor and power inductor are used to smooth out the current

transient and current ripples for the static torque tests. For the inductance measurements, they are detached from the testbed. Phase A, Phase B, and the respective stroke period of Phase A and Phase B are tested. Each phase was tested up to 21A. Theoretically, each phase should operate at 28A to reach the rated ampere turns of the designed model. The vents on the support unit were made much smaller than what they should be as a tradeoff between the machining complexity and lead time. Even though the motor windings are rated for around 200C. It cannot be guaranteed that the thermal stress would not lead to any failure in insulation or bundling of the windings. To simplify the winding installation, each phase is built by single-branch AWG18 magnetic wire. The ohmic loss is much higher than the designed model. All below tests operate with short durations to avoid failures due to the thermal stress. The static torque of phase A and static torque of phase B are shown in Figure 6.5. Each phase turns on for consecutive 8 mechanical degrees.

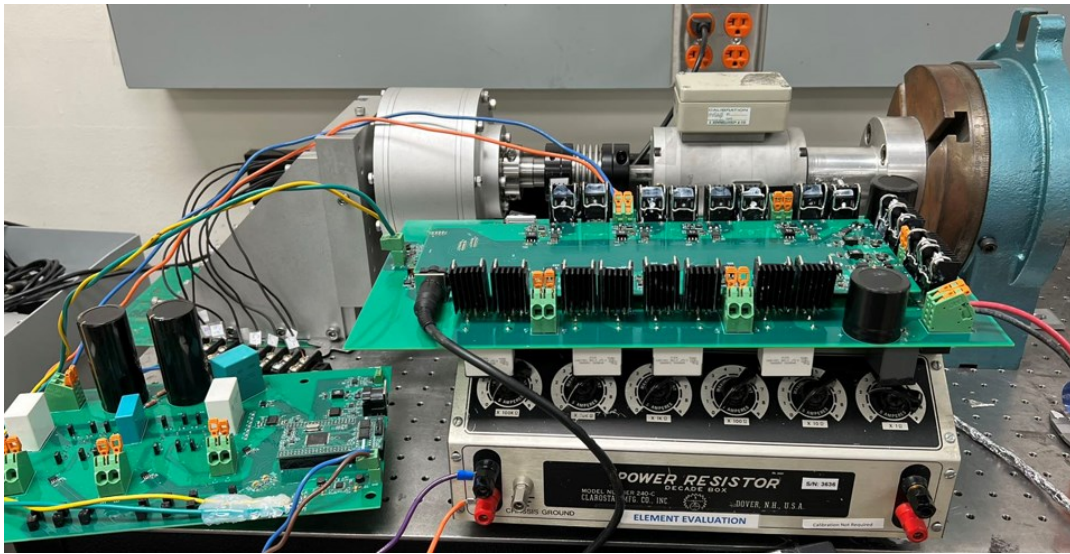


Figure 6.4: The static torque testbed.

Each phase excitation overlaps with the excitation of the outgoing phase for the first 4 mechanical degrees. It overlaps with the excitation of the incoming phase for the remaining 4

mechanical degrees. The stroke torques of phase A and phase B are shown in Figure 6.6. All static torque and inductance measurements are proceeded with 1 mechanical degree step-size which is the minimal resolution of the position rotary indexer.

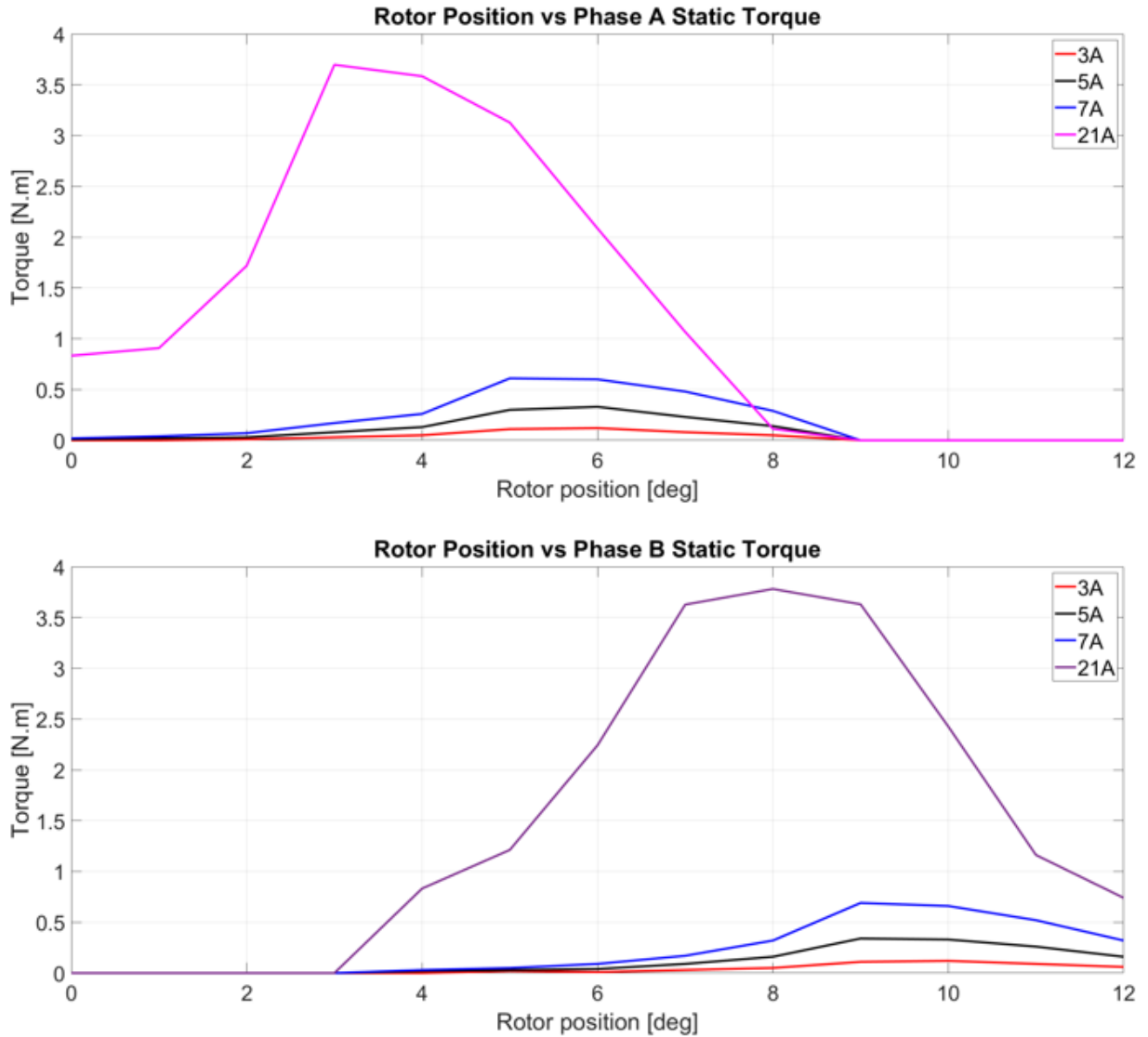
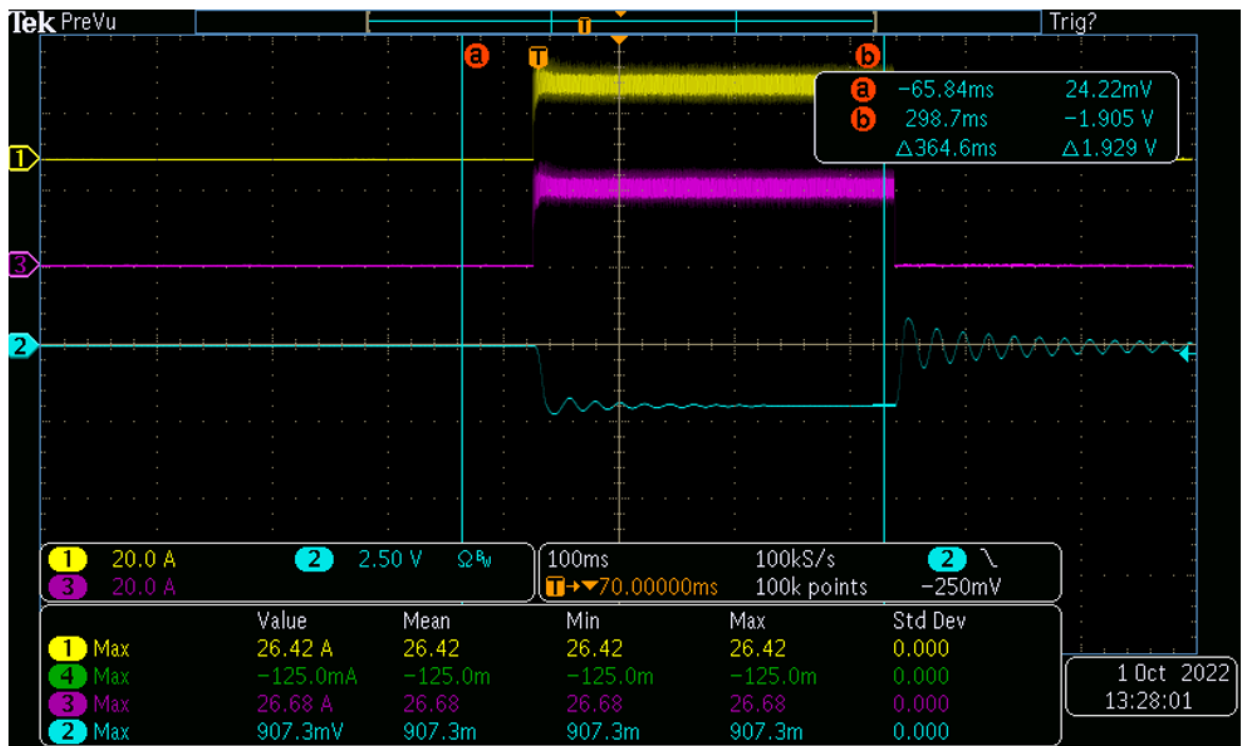
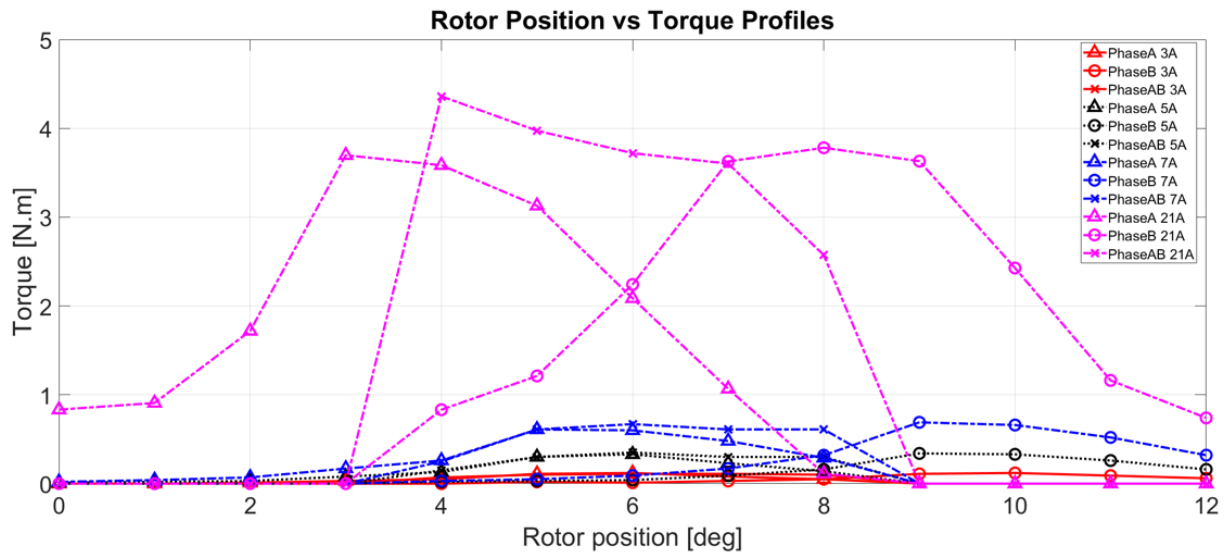


Figure 6.5: Static torque of phase A and phase B.

Due to the manual winding installation and stator assembly including the edge grinding of stator axial poles, there could be some discrepancy between static torques of Phase A and Phase B while the trends clearly prove the design concept. Considering the differences between magnetic

properties of equivalent BA35A250 and Hiperco 50 and the difference between 39 turns and 140 turns, the average torque could reach around 8 N.m if all factors are ideal. The oscilloscope reading at the initial position of the stroke of Phase A and Phase B is shown in Figure 6.7. The blue curve is the torque meter signal. The switching frequency is set to 40kHz. The VDC is set to 50V. Even though the current hysteresis band is set to 0.1A, the circuit dynamics surely makes the actual current band larger than the desired band. The average number still meets the expectation. As shown in Figure 6.7, at the initial position of the stroke for Phase A and Phase B, both Phase A and Phase B should be constantly ON. Once the torque meter reading reaches the steady state point, both phases are turned off. The test duration of the static torque is set to 750ms. Given the sensing gain of the torque meter, 2.26N.m/V, the 1.929V torque meter reading corresponds to 4.35 N.m as shown in Figure 6.6. The inductance profile of Phase A and Phase B are also estimated from the current transients. During the data collection process, it is sensed that the parasitic capacitance significantly impacts the current transients and voltage transients. Figure 6.8 shows the current and voltage transients at 3V and 3A. At this operating point, the parasitic capacitance impacts the flux linkage calculation and inductance estimation are not reliable. The trends of estimated flux linkage and phase inductance are reasonable.



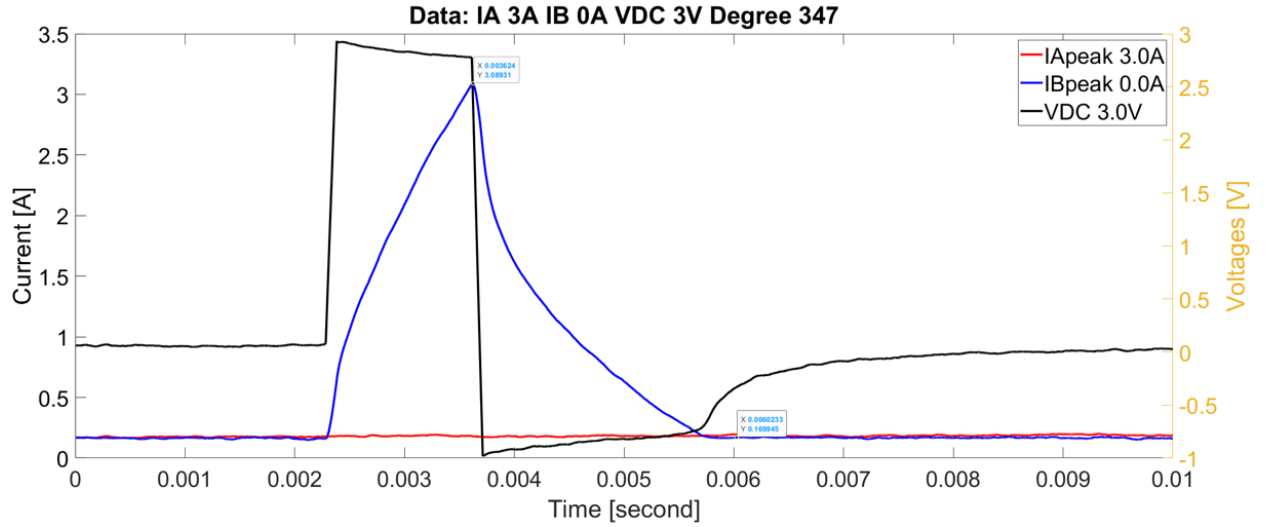


Figure 6.8: the current and voltage transient.

The missing parts of the winding voltage are due to the cable impedance. Next, higher excitations are applied and larger voltage will be held by the cable impedances. Under a lower voltage and a lower excitation, this phenomena mitigates a bit such that 3V and 3A winding tests are successful. Even though the calculations of flux linkages upon the raising edges of current profiles can show an increasing trend, the results are not quite in the reasonable scope due to the impacts of parasitic capacitance. The DC resistance of the winding is about 0.6 ohm. However, the inductance estimation based on the falling edges of the current profiles could be reasonable. The time constant is $\frac{L}{R}$. To achieve the steady state, it could require 5 times of the time constant. The inductance estimation is based on $5t_{falling} \times 0.6$ where the DC resistance of the winding is about 0.6 ohm. The estimated inductance profile is shown in Figure 6.9. The saliency ratio of the down-scaled prototype at unsaturated conditions is around 180%. Considering the ideal number of turns per stator slot, the estimated inductance profiles could be boosted by 12.96 under unsaturated conditions. Since the machine core is not Hiperco 50, the actual inductance profile of the ideal prototype could be even more different.

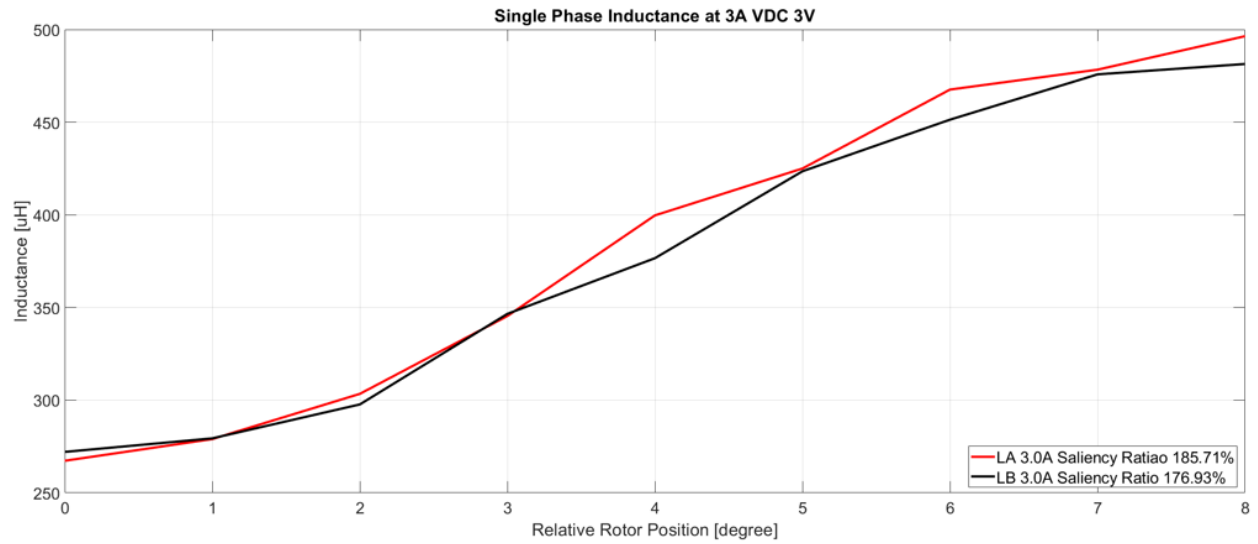


Figure 6.9: The reconstructed inductance profile.

6.2 Discussion of discrepancies between simulation results and experimental results

Since the manufactured motor used a different material (B35A250) compared to the earlier designed version (Hiperco 50), the following simulations are conducted in order to compare the experimental results and the simulation results. Since the model is dependent on the accuracy of the 3D FEA solvers, it is reasonable to study the mismatches. The 3D magnetostatic solver does not directly provide the phase inductances while it indeed provides much better mesh quality and more accurate flux information. As a result, the unsaturated inductances are firstly estimated using the 3D FEA simulation results at 3A. Only phase D is energized and since the model is symmetric the phase D inductance will be identical to other phases. The models for magnetostatic solver and co-simulated transient solver have been modified by the B-H curve of B35A250 27mil. The number of winding turns is revised to 39 as well. Even though the purchased magnetic material is sold as B35A250, the bulk material is not certificated by BAO STEEL. As a result, there could be discrepancies in BH curve. However, the following comparative simulations are based on the BH curve of BA35A250 27mil data which is purchased

from MagWeb. For the first-round magnetostatic simulations, the phase D current is set to 3A to be identical with the experimental tests. Theoretically, at 3A the model is not saturated and the loop reluctances are dominated by the airgaps. Using the active airgaps, inductances could be estimated. The magnetic circuit of one stator slot has two axial airgaps on the two sides and one radial airgap. The other side of the stator has the same magnetic circuit. The loop reluctances of the two sides are cascaded. Such that the phase inductance could be estimated by equation (6.1).

$$L_{total} = \frac{2N^2}{R_{eq}} = \frac{2N^2}{R_r // R_a // R_a} \quad (6.1)$$

$$R_r = \frac{2g_r}{u_0 A_r} \quad R_a = \frac{2g_a}{u_0 A_r}$$

Where $u_0 = 4\pi \times 10^{-7} \text{ N/A} = 39 \text{ g}$ and g_r and g_a are both 0.4mm at aligned position. As the rotor position changes the equivalent airgap and equivalent surface area changes accordingly. g_r stands for the radial airgap and g_a stands for the axial airgap.

Since the 3D magnetic field is not uniformly distributed along the axial and radial direction, here the average estimation is used. Figure 6.10 shows a few magnetic plots at the aligned position. Different flux distribution patterns along radial direction and axial direction could be seen. At the stator center, the range of utilized airgap is from 25.3 to 23.35 degree. At the end of radial rotor segment, the airgap flux density is really low such that those regions are not magnetically engaged. Therefore, the way to estimate the radial airgap surface is to shift the radial probe sheet along the z axis and identify regions of airgap that are utilized. The same process is done for the axial pole. In Figure 6.10, it could be seen that the overlapped regions between axial stator pole and axial rotor segment surface is in the range of 2.14 to 20.4 degree. The estimated inductance at aligned position at the aligned position with 3A excitation is about 768uH. Applying the same

process to unaligned position, the estimated inductance is about 253.5uH. By changing the nominal airgap, the estimated aligned position inductance and estimated unaligned position inductance are shown in Figure 6.11. The unaligned position inductance does not significantly vary with the changes of airgap, however, the aligned position inductance does exhibit notable changes. This could explain the discrepancy between the experimental measurements and simulation results since the manual installation and manufacturing tolerances could introduce additional airgap and geometrical mismatch. By using the actual pattern of flux distribution from magnetostatic simulation with 0.4mm airgap, the estimated inductance with different airgap length are computed and illustrated in Figure 6.12.

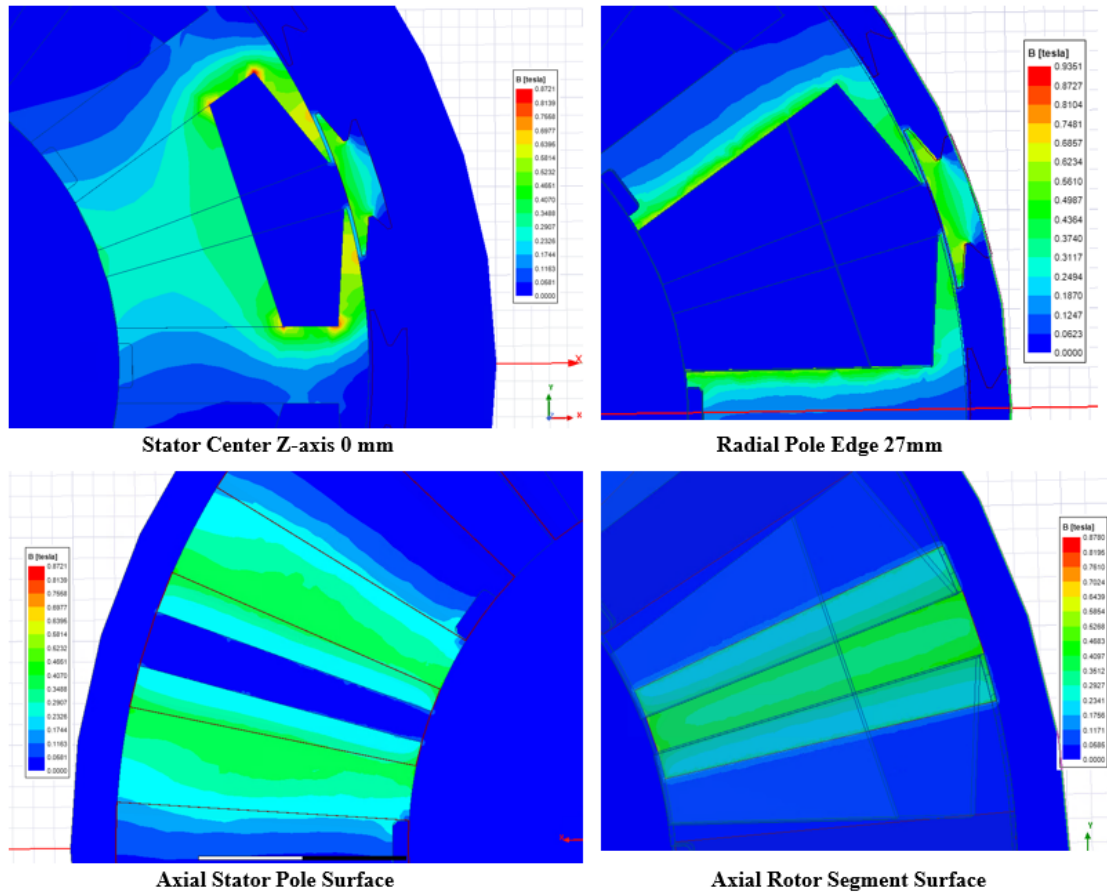


Figure 6.10: Flux plot at different positions.

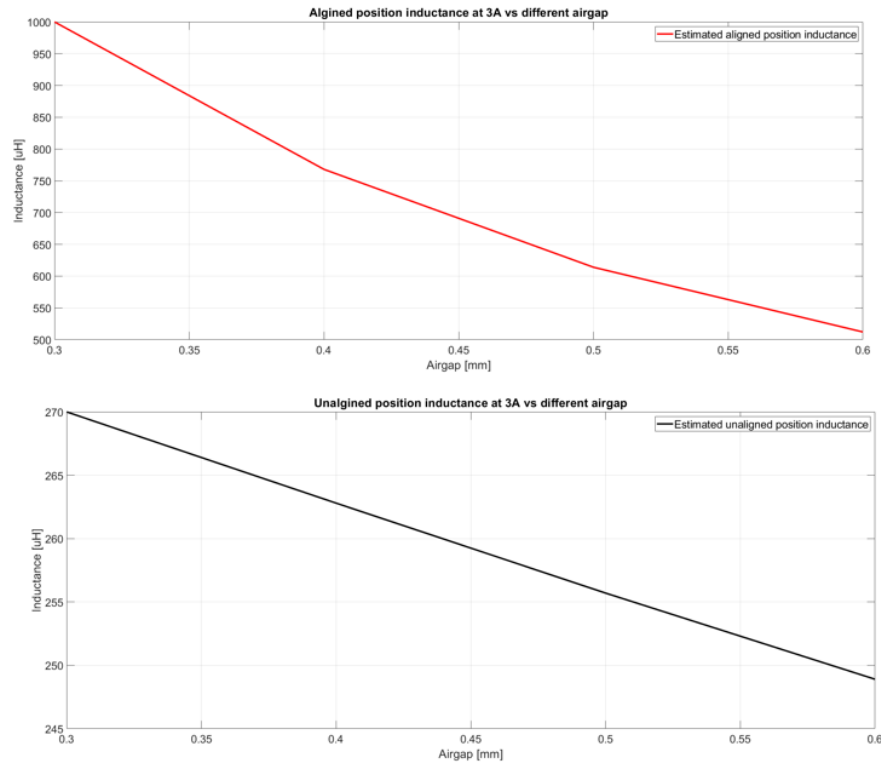


Figure 6.11: estimated aligned position inductance and unaligned position inductance.

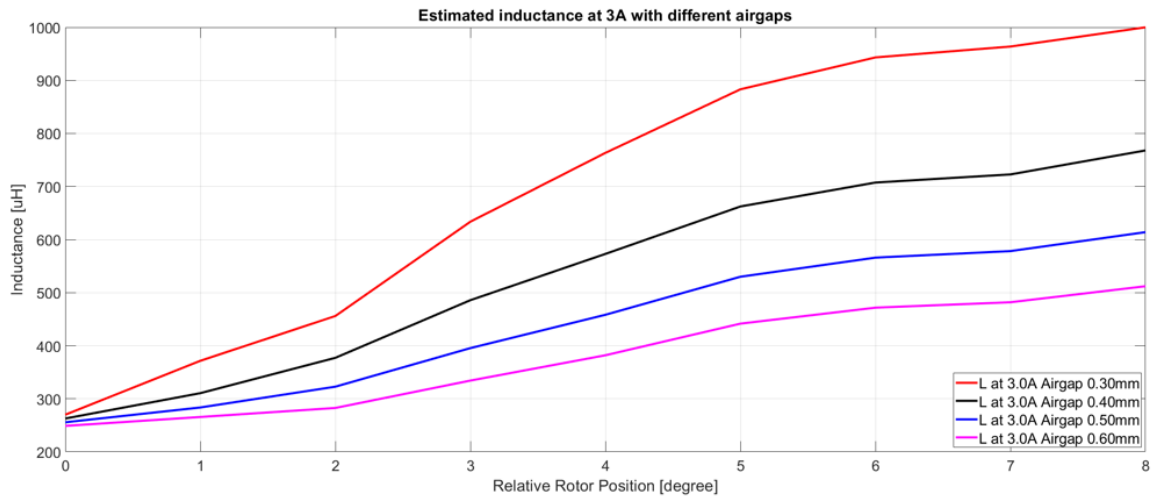


Figure 6.12: estimated inductance profiles with different airgaps.

To further check the inductance profile, the co-simulations with magnetic-transient solver are conducted. Due to the coarse mesh quality of the transient solver, which is uncontrollable, the results still show discrepancies from the experimental results. However, the results of this study

follow the same trend. By changing the radial airgap and axial airgap, the inductance profiles can be substantially affected. In the simulation, the 3V is applied to a phase when the shaft is locked at certain rotor position. These inductances are estimated by area integral of $V-iR$ with respect to time then divided by the nominal 3A excitation. The experimental results and co-simulation results are shown in Figure 6.14. The red-dashed curve is the experimental measured phase A inductance profile while the red solid curve is the experimentally measured phase B inductance profile. The blue dotted curve is the inductance profile of the revised model with 0.3mm on both radial airgap and axial airgap. The blue dash-and-dotted curve is the inductance profile of the revised model with 0.4mm radial airgap and 0.3mm axial airgap. The blue dashed curve is the inductance profile of the revised model with 0.3mm radial airgap and 0.4mm axial airgap. The blue solid curve is the inductance profile of the original model. The saliency ratios of the experimental inductance profiles are around 180% while the saliency ratios of co-simulated results are around 280%. The unaligned position inductances of co-simulation results are lower than experimental results which could be due to the mesh quality of transient solver.

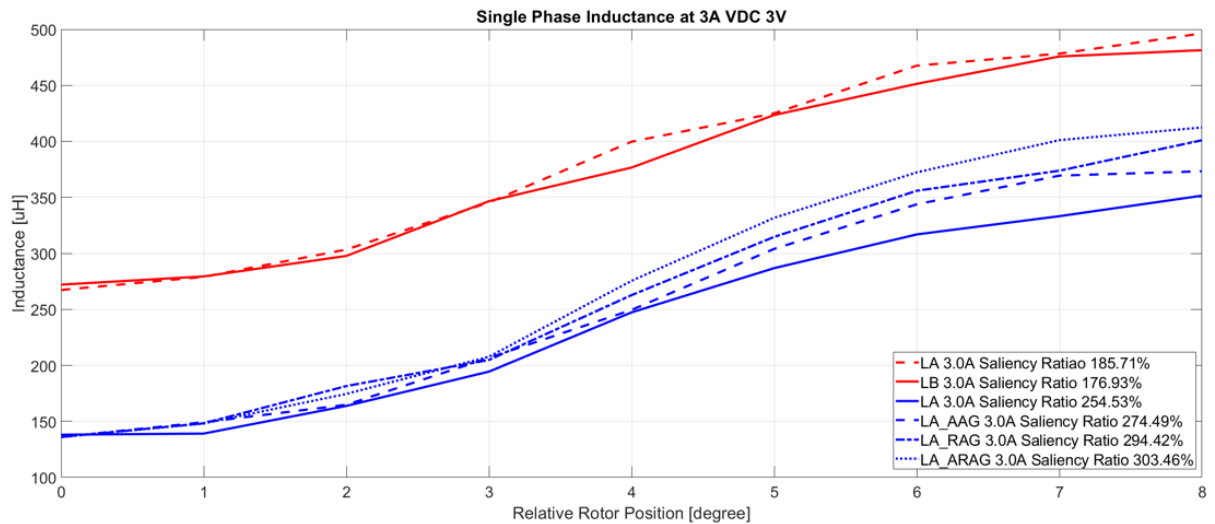


Figure 6.13: The experimental inductance profiles and co-simulated inductance profiles.

It is our conclusion that the experimental inductance profiles do not show higher saliency ratios due to the imperfect implementation. However, the trend study indeed demonstrates the incremental rise in inductances when the airgap is reduced, and the saliency-ratio could be boosted. The static model is configured for BH curve of B35A250 27mil and magnetostatic simulation under 21A phase excitation is performed. The winding configuration is identical with the experimental setup where the winding is single branch with 39 turns. The simulated static phase torque and stroke torque are presented in Figure 6.14. The average torque for phase A is 2.08 N.m while the average torque for phase-B is 2.35 N.m. The average of the simulated single-phase torque is 3.23 N.m. The average of simulated stroke torque is 5.39 N.m. The experimental stroke torque is about 3.69 N.m. The discrepancy of average value is about 32% due to the imperfect implementation and additional airgap between stator pieces. However, the shapes of the simulated torques are very similar to those from the experimental results. With higher accuracy of experimental measurements and the more precise assembly of the machine, the experimental results could be closer to the simulation results. Throughout all simulations and experiments, the trends of the results are reasonable.

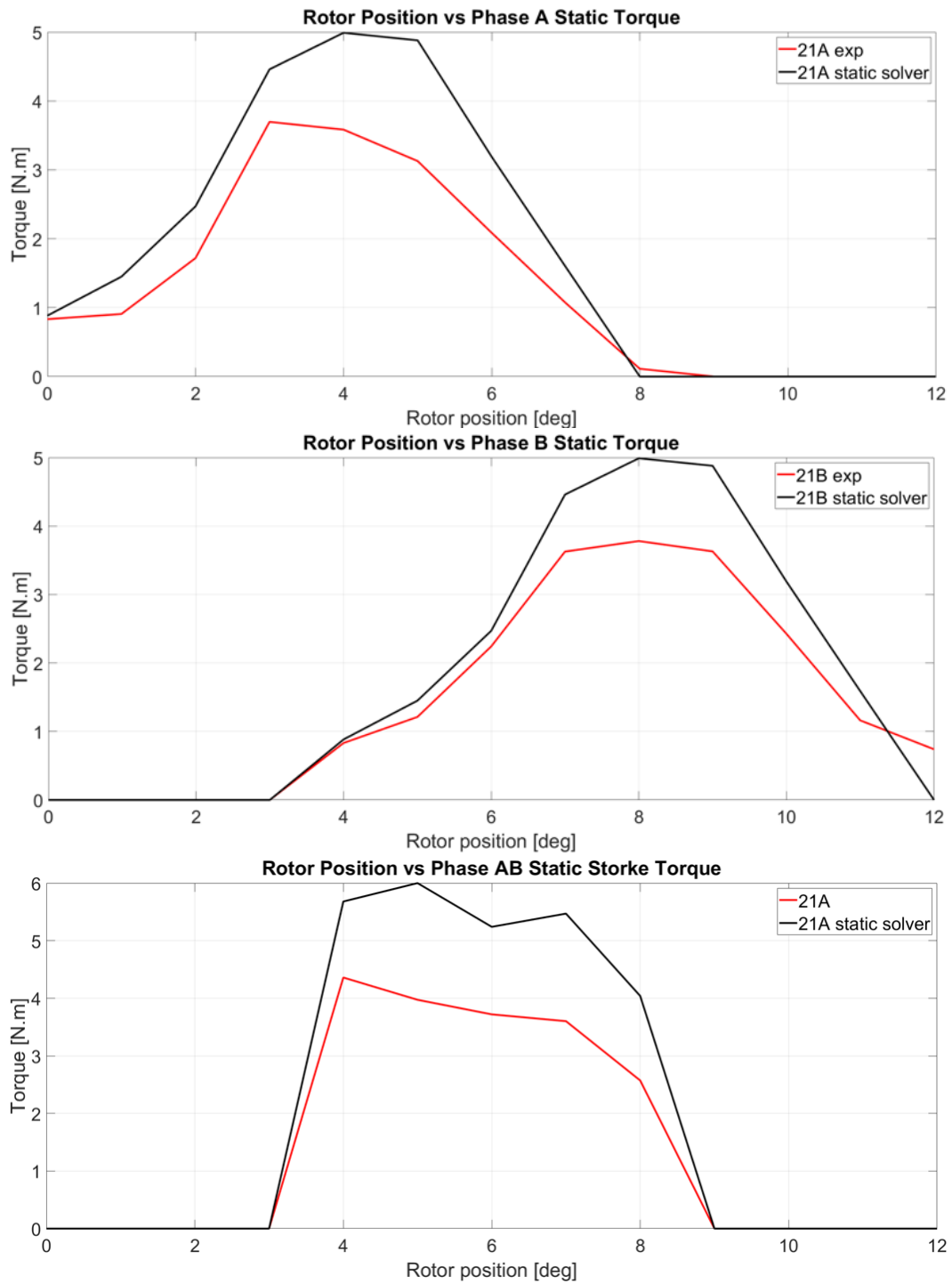


Figure 6.14 The comparisons between simulated torques and experimental results.

CHAPTER 7

CONCLUSION AND FUTURE WORKS

In this thesis, a novel 3D flux structure has been proposed. The review of conventional machine topologies is presented in the first chapter. The principal differences of various types of electrical SR machines are discussed as well. The reasoning for the proposed idea and how it improves common switched reluctance machine have been also presented. The proposed structure can be applied to induction machine and PM machines as well. Given the simple structure, the switched reluctance machine is selected for validating the idea.

In chapter 2, fundamental design principles of switched reluctance machine are addressed in detail. The salient-pole 3D flux structure is proposed as well as the corresponding design methodology. Beside maximally utilizing the inner space of an electrical machine, the proposed structure can also reduce the volume of the end windings.

In chapter 3, the segmented-rotor version of the novel 3D flux 08/14 switched reluctance machine and its magnetic merits are demonstrated. It mainly solves the negative torque issue of the pole configuration in a higher number of rotor poles than stator poles. However, it brings in its own deficiencies in terms of circulating magnetic flux due to the differences among the adjacent active phases. To thoroughly solve all potential deficiencies while migrating all advantages of previous designs, a segmented-rotor 3D flux 10/18 machine is proposed.

In chapter 4, the underlying logic of Genetic Algorithm, which is the optimization tool of the entire design process, has been discussed. The flowchart of the design and optimization flow chart is presented as well.

In chapter 5, the simulation results of the scaled-down 10/18 SRM are demonstrated to address the concerns of mechanical integrity, thermal stress, average torque, and electrical commutation.

The logics in deciding the parameters of the fabricated model are introduced as well.

In chapter 6, the experimental results of the scaled-down prototype with multiple fabrication tradeoffs are demonstrated. The static single-phase torque, stroke torques, and inductance profiles prove the design concepts. The 1-liter prototype indeed shows high torque density. As for ideal prototype without any tradeoff, the performance should be able to match the simulation results.

As the proposed structure requires decent manufacturing supports, it is designed as a step forward towards future machines. As the more precise 3D printing techniques are developed, more advantages of such 3D flux structures could be seen and be commercialized for EV, drones, and UAV applications which demands high-torque density propulsion units. Multiple topologies and machine types could be investigated using the proposed structure.

REFERENCES

- [1] C. H. T. Lee, W. Hua, T. Long, C. Jiang and L. V. Iyer, "A Critical Review of Emerging Technologies for Electric and Hybrid Vehicles," in *IEEE Open Journal of Vehicular Technology*, vol. 2, pp. 471-485, 2021, doi: 10.1109/OJVT.2021.3138894.
- [2] C. Liu, K. T. Chau, C. H. T. Lee and Z. Song, "A Critical Review of Advanced Electric Machines and Control Strategies for Electric Vehicles," in *Proceedings of the IEEE*, vol. 109, no. 6, pp. 1004-1028, June 2021, doi: 10.1109/JPROC.2020.3041417.
- [3] D. Gerada, A. Mebarki, N. L. Brown, C. Gerada, A. Cavagnino and A. Boglietti, "High-Speed Electrical Machines: Technologies, Trends, and Developments," in *IEEE Transactions on Industrial Electronics*, vol. 61, no. 6, pp. 2946-2959, June 2014, doi: 10.1109/TIE.2013.2286777.
- [4] F. Bu et al., "Induction-machine-based starter/generator systems: Techniques, developments, and advances," *IEEE Ind. Electron. Mag.*, vol. 14, no. 1, pp. 4–19, Mar. 2020.
- [5] N. Rivière, G. Volpe, M. Villani, G. Fabri, L. Di Leonardo, and M. Popescu, "Design analysis of a high-speed copper rotor induction motor for a traction application," in *Proc. IEEE Int. Electric. Mach. Drives Conf. (IEMDC)*, May 2019, pp. 1024–1031.
- [6] Miller, TJE, "*Switched Reluctance Motors and their Control*", Magna Physics Publishing and Clarendon Press, Oxford, 1993.
- [7] J. W. Jiang, B. Bilgin, and A. Emadi, "Three-phase 24/16 switched reluctance machine for a hybrid electric powertrain," *IEEE Trans. Transport. Electrific.*, vol. 3, no. 1, pp. 76–85, Mar. 2017
- [8] A. M. Omekanda, "Switched reluctance machines for EV and HEV propulsion: State-of-the-art," in *Proc. IEEE Workshop Electr. Mach. Design, Control Diagnosis (WEMDCD)*, Mar. 2013, pp. 70–74.
- [9] Fang, H. 2019. Structural Studies of Mn-X (X=Al, Bi): Permanent Magnetic Materials without Rare Earth Metals. Digital Comprehensive Summaries of Uppsala Dissertations from the Faculty of Science and Technology 1782. 57 pp. Uppsala: Acta Universitatis Upsaliensis. ISBN 978-91-513-0594-3.
- [10] M. Cheng, W. Hua, J. Zhang, and W. Zhao, "Overview of stator-permanent magnet brushless machines," *IEEE Trans. Ind. Electron.*, vol. 58, no. 11, pp. 5087–5101, Nov. 2011
- [11] C. Liu, K. T. Chau, and J. Z. Jiang, "A permanent-magnet hybrid brushless integrated starter-generator for hybrid electric vehicles," *IEEE Trans. Ind. Electron.*, vol. 57, no. 12, pp. 4055–4064, Dec. 2010.
- [12] N. Bianchi, S. Bolognani, E. Carraro, M. Castiello, and E. Fornasiero, "Electric vehicle traction based on synchronous reluctance motors," *IEEE Trans. Ind. Appl.*, vol. 52, no. 6, pp. 4762–4769, Nov./Dec. 2016.

- [13] J. Yu, C. Liu, and H. Zhao, "Design and multi-mode operation of double-stator toroidal-winding PM Vernier machine for wind-photovoltaic hybrid generation system," *IEEE Trans. Magn.*, vol. 55, no. 7, pp. 1–7, Jul. 2019.
- [14] W. Wang, M. Luo, E. Cosoroaba, B. Fahimi and M. Kiani, "Rotor Shape Investigation and Optimization of Double Stator Switched Reluctance Machine," in *IEEE Transactions on Magnetism*, vol. 51, no. 3, pp. 1-4, March 2015, Art no. 8103304, doi: 10.1109/TMAG.2014.2356573.
- [15] S. E. Rauch and L. J. Johnson, "Design principles of flux-switching alternators," *AIEE Trans.*, vol. 74, no. 3, pp. 1261–1268, Jan. 1955.
- [16] G. J. Li, X. Y. Ma, G. W. Jewell and Z. Q. Zhu, "Novel Modular Switched Reluctance Machines for Performance Improvement," in *IEEE Transactions on Energy Conversion*, vol. 33, no. 3, pp. 1255-1265, Sept. 2018
- [17] M. Abdalmagid, E. Sayed, M. H. Bakr and A. Emadi, "Geometry and Topology Optimization of Switched Reluctance Machines: A Review," in *IEEE Access*, vol. 10, pp. 5141-5170, 2022, doi: 10.1109/ACCESS.2022.3140440.
- [18] K. Kiyota, T. Kakishima, A. Chiba and M. A. Rahman, "Cylindrical Rotor Design for Acoustic Noise and Windage Loss Reduction in Switched Reluctance Motor for HEV Applications," in *IEEE Transactions on Industry Applications*, vol. 52, no. 1, pp. 154-162, Jan.-Feb. 2016
- [19] S. Li, S. Zhang, T. G. Habetler and R. G. Harley, "Modeling, Design Optimization, and Applications of Switched Reluctance Machines—A Review," in *IEEE Transactions on Industry Applications*, vol. 55, no. 3, pp. 2660-2681, May-June 2019, doi: 10.1109/TIA.2019.2897965.
- [20] Parveen Vijayraghavan, "Design of Switched Reluctance Motors and Development of a Universal Controller for Switched Reluctance and Permanent Magnet Brushless DC Motor Drives", PhD dissertation, Virginia Polytechnic Institute and State University, 2001.
- [21] P. C. Desai, M. Krishnamurthy, N. Schofield and A. Emadi, "Novel Switched Reluctance Machine Configuration With Higher Number of Rotor Poles Than Stator Poles: Concept to Implementation," in *IEEE Transactions on Industrial Electronics*, vol. 57, no. 2, pp. 649-659, Feb. 2010, doi: 10.1109/TIE.2009.2034678.
- [22] B. Bilgin, A. Emadi and M. Krishnamurthy, "Design Considerations for Switched Reluctance Machines With a Higher Number of Rotor Poles," in *IEEE Transactions on Industrial Electronics*, vol. 59, no. 10, pp. 3745-3756, Oct. 2012, doi: 10.1109/TIE.2011.2141102.
- [23] R. Madhavan and B. G. Fernandes, "Axial Flux Segmented SRM With a Higher Number of Rotor Segments for Electric Vehicles," in *IEEE Transactions on Energy Conversion*, vol. 28, no. 1, pp. 203-213, March 2013, doi: 10.1109/TEC.2012.2235068.

- [24] X. Liu and Z. Q. Zhu, "Stator/Rotor Pole Combinations and Winding Configurations of Variable Flux Reluctance Machines," in *IEEE Transactions on Industry Applications*, vol. 50, no. 6, pp. 3675-3684, Nov.-Dec. 2014, doi: 10.1109/TIA.2014.2315505.
- [25] V. R and B. G. Fernandes, "Design Methodology for High-Performance Segmented Rotor Switched Reluctance Motors," in *IEEE Transactions on Energy Conversion*, vol. 30, no. 1, pp. 11-21, March 2015, doi: 10.1109/TEC.2014.2336861.
- [26] B. Mecrow, J. Finch, E. El-Kharashi, and A. Jack, "Switched reluctance motors with segmental rotors," *IEE Proc.—Electric. Power Appl.*, vol. 149, no. 4, pp. 245–254, Jul. 2002.
- [27] Hiperco 50 material datasheet, "Hiperco 50 & 50A Properties," June 14th 2005 [online] Available: <https://edfagan.com/hiperco-50-coil>
- [28] Parveen Vijayraghavan, "Design of Switched Reluctance Motors and Development of a Universal Controller for Switched Reluctance and Permanent Magnet Brushless DC Motor Drives", PhD dissertation, Virginia Polytechnic Institute and State University, 2001.
- [29] Google image link of motor end windings:
https://www.google.com/search?q=motor+end+winding&tbm=isch&source=hp&biw=1920&bih=937&ei=5oluY9HKIuaiqtsPtL2twAg&iflsig=AJiK0e8AAAAAY26X9iWeUqxPFv7mJvIWvx9OaZrrncRl&ved=0ahUKEwjRlcn9lqb7AhVmkWoFHbReC4gQ4dUDCAc&uact=5&oq=motor+end+winding&gs_lcp=CgNpbWcQAzIFCAAQgAQyBggAEAgQHjoICAAQgAQQsQM6CAgAELEDEIMBOgsIABCABBCxAxCDAToHCAAQgAQQGFC-BViKL2C6MWgIcAB4AIABrAGIAZQIkGEEMjQuMZgBAKABAaoBC2d3cy13aXotaW1nsAEA&sclient=img
- [30] P. Chen, B. Fahimi, M. Moallem and M. Kiani, "A Novel Structure for Exterior-Rotor Switched Reluctance Machines," 2020 International Symposium on Power Electronics, Electrical Drives, Automation and Motion (SPEEDAM), 2020, pp. 466-471, doi: 10.1109/SPEEDAM48782.2020.9161921.

BIOGRAPHICAL SKETCH

Pengyuan Chen is a current PhD student in the department of electrical and computer engineering of The University of Texas at Dallas. He joined the REVT lab since 2018 and has worked towards his PhD degree in the direction of electrical machine design and power electronics. He holds BS and MS degrees in electrical engineering from the Beijing University of Technology and the California State University at Fresno in 2009 and 2015, respectively.

CURRICULUM VITAE

Pengyuan Chen

CAREER SUMMARY

About 10 years of research and industrial experiences on electrical engineering (firmware design and power electronics). Have independent firmware design experiences and solid understanding on the mixed signal system and linking between firmware and hardware systems. Fast learning.

TECHNICAL SKILLS

Hardware Experiences

- Professional on EE (power electronics, circuit modeling, testbed design, and control technique)
- Circuit design, debug, and trouble shooting
- System/circuit simulation MATLAB/Simulink, PLECS
- Schematic and PCB/Layout Design: Altium designer

Embedded Devices/Firmware

- MCU (C2000 series, Atmel, TI CC2430) – C language Assembly language
- Development environment – Code Studio Composer, IAR workbench, Borland C++

EMPLOYMENT

- Jing-Jin Electric Power Electronic Engineer Oct
2017 – Dec 2017
Revision and debug on 50kW/100kW DC-DC EV LV charging system. 300kW EV power system layout design for national funded research on 12-meter EV bus.
- VOLLRATH.co.LLC Firmware & Power Electronics Engineer Oct
2015 – May 2017
Commercial firmware maintaining and customization on 200W~3kW induction cooker series resonance circuit. Independent redesign firmware to achieve automatic collaboration of products and solve the beat frequency issue which keeps deferring the new product launch. The new designed firmware, power firmware and control firmware, is compatible with existing power boards. New generation 3kW power board development using F28075 TI MCU to boost the capacity of the computation and communication to merge the future needs. Troubleshooting the returned products.
- SMC Pneumatics Center of Tsinghua University IoT System Design Engineer Dec
2009 – Dec 2012
Independent research and development of TI CC2430-based IoT system involving propulsion systems, cylinders, remote sensors, magnetic valves, cooling system, and heating system.

EDUCATION

- | | | |
|---|---------------------------------------|-------------|
| PhD candidate, Electrical Engineering
Jan 2018 – now | University of Texas at Dallas | GPA 3.9 |
| MASTER, Electrical Engineering
2013 – Aug 2015 | California State University at Fresno | GPA 3.8 Jan |
| BSEE, Electrical Engineering
2005 – Aug 2009 | Beijing University of Technology | GPA 3.3 Aug |
- 1 UTD patents in process
 - Published 12 conference papers, 1 in process

PROJECTS EXPERIENCE

- R&D dynamic 30kW SiC driver – System Design and Test Firmware
Sep 2021 – now
Independent design SiC inverter and TI F28388D based control stage design for high-speed electrical machines. Logistic management of the whole development process from parts purchasing (distributed market), customization parts, test protocol to fit the rapid development window around 6 months.
- SMC Turntide 1.8kW SRM upgrading – Testbed, Driver, and Test Firmware Jan
2021 – Aug 2021
Independent design SiC-module based power stage and TI F28388D based control stage design for low speed SRM. Automatic data acquisition and processing setup design via MATLAB scripts and Jupiter Python IDE.
- Southern California Edison MPPT algorithm research – Adaptative MPPT System Design Aug
2014 – Aug 2015
Independent discrete-MOSFET power board design and TI F28335 based control stage design. The adaptative P&O algorithm is developed in MATLAB and embedded into TI MCU.
- SMC Corporation Vehicle Washing System – Testbed GUI Design Aug
2009 – Dec 2012
Borland C++ GUI design for a vehicle washing system prototype. High-level firmware design in windows interacts with a FPGA control box for data acquisition and process, commanding PLC and servo motors, and automatic report generation.

PUBLICATIONS

1. P. Chen, B. Fahimi, M. Moallem and M. Kiani, "A Novel Structure for Exterior-Rotor Switched Reluctance Machines," SPEEDAM, 2020.
 2. T. Chen, C. Caicedo-Narvaez, P. Chen, A. Parsapour and B. Fahimi, "Design of a 6.8-kW Two-Phase Converter for 48V Automotive Applications," APEC, 2020.
 3. P. Chen, T. Chen, J. Liang, B. Fahimi and M. Moallem, "Torque Ripple Mitigation Via Optimized Current Profiling in Interior Permanent Magnet Synchronous Motors," 2019 IEMDC.
 4. T. Chen, P. Chen, J. Liang, S. Li and B. Fahimi, "Maximum Torque Per Ampere Control of Interior Permanent Magnet Synchronous Motor via Optimal Current Excitation," 2019 ECCE.
UTD Patent: High Torque Density 3D Flux Segmented-Rotor Switched Reluctance Machine (USPTO 63/354,065, 06/21/22)
-